10-18-2018

Computational Aerodynamics and Anatomical Characterization of Laryngotracheal Stenosis in Children

William Poynot
Louisiana State University and Agricultural and Mechanical College

COMPUTATIONAL AERODYNAMICS AND ANATOMICAL CHARACTERIZATION OF LARYNGOTRACHEAL STENOSIS IN CHILDREN

A Thesis

Submitted to the Graduate Faculty of the
Louisiana State University and
Agricultural and Mechanical College
in partial fulfillment of the
requirements for the degree of
Master of Science

in

The Department of Mechanical and Industrial Engineering

by
William Joseph Poynot
B.S. Mechanical Engineering, Louisiana State University, 2013
December 2018

Acknowledgments

With any endeavor, it is seldom the case that the outcomes may be solely attributed to the efforts of one individual. The research detailed in this thesis is no exception. As such, I would first like to thank my faculty advisor, Dr. Keith A. Gonthier, for his invaluable guidance and support throughout my graduate studies. His integrity and expertise have helped me to become a more effective engineer, researcher, and communicator. I would like to thank Dr. Michael Dunham for allowing us to collaborate with him and for providing valuable insights into the medical and clinical issues. I would also like to thank Dr. Dimitris E. Nikitopoulos and Dr. Mayank Tyagi for agreeing to serve on my committee and for providing valuable critique and advice. I would also like to thank Dr. Harris Wong for guiding my development as an applied mathematician and fluid dynamicist.

I thank the Louisiana Biomedical Collaborative Research Program for sponsoring this research, and I thank the Department of Mechanical and Industrial Engineering for supporting me during my program and for giving me the opportunity to teach undergraduate Capstone Design and Fluid Mechanics classes. I would also like to acknowledge the Louisiana Optical Network Initiative (LONI) for providing high-performance computational resources, without which the scope of this research would have been severely restricted. I would like to thank my family and friends, who have been a constant source of support. Finally, I must thank my fianceé Carrie for her unyielding faith and support, from which I have drawn much of the strength and inspiration that has carried me through my graduate school journey.

Table of Contents

ACKNOWLEDGMENTS ii

LIST OF TABLES v

LIST OF FIGURES vi

ABSTRACT xi

CHAPTER

1 INTRODUCTION 1
- 1.1 Background and Problem Description 1
- 1.2 Anatomy of the Human Airway 2
- 1.3 Statistics of Pediatric Ventilation 2
- 1.4 Literature Survey 6
- 1.5 Study Objectives 10

2 MODELING & NUMERICAL METHODS 12
- 2.1 Computational Fluid Dynamics (CFD) 12
- 2.2 Airway Model Generation 18

3 ANATOMICAL CHARACTERIZATION OF STENOSIS 21
- 3.1 Characteristic Dimensions 21
- 3.2 Medial Axis Projection 22
- 3.3 Feature Location Identification 23
- 3.4 Feature Length Scale Identification 24
- 3.5 Verification 26
- 3.6 Feature Identification of Stenosis in Real Airways 29
- 3.7 Discussion 31

4 COMPUTATIONAL FLUID DYNAMICS OF STENOTIC TUBE 34
- 4.1 Turbulence Model Validation 34
- 4.2 Mesh Sensitivity 38
- 4.3 Discussion 43

5 COMPUTATIONAL FLUID DYNAMICS OF REAL AIRWAYS 44
- 5.1 Model Complexity 44
- 5.2 Aerodynamic Indicators 45
- 5.3 Reduction of the Computational Domain 47
- 5.4 Simulations on Truncated Domains with Stenosis 55
- 5.5 Correlations Between Aerodynamics and Anatomy 63
- 5.6 Simulation of a Sinusoidal Inspiration Cycle 72
- 5.7 Discussion 74

6 CONCLUSIONS & FUTURE WORK 78

6.1 Future Computational Studies 79
6.2 Future Experimental and Clinical Studies 80
6.3 Toward Medical Software and Patient Impact 81

REFERENCES 83

APPENDIX
A TURBULENCE MODEL 87
A.1 Transport Equations 87
A.2 Production Terms 88
A.3 Dissipation Terms 89
A.4 Cross-Diffusion Term 90
A.5 Model Constants 90

B PARAMETRIC SENSITIVITY TO INFLOW BOUNDARY 92
B.1 Biased Inlet Flow Distribution 92
B.2 Directivity of Inlet Flow 95
B.3 Numerical Simulations 95
B.4 Discussion 97

VITA 99

List of Tables

1.1 Variations in mean respiratory rate across age groups [9] 3

1.2 Dimensional variations of trachea with respect to age [10] 4

1.3 Pressure loss coefficients from axisymmetric stenotic tube experiments (adapted from [47]) 9

3.1 Verification of wavelet-based feature length scale identification algorithm using axisymmetric stenotic tube model. 28

4.1 Mesh parameters used in mesh sensitivity study. 39

5.1 Ranges of relative flow rate Φ for Myer-Cotton Grades I-III based on best fits for two stenosis widths $w/D_0 = 0.75$ and $w/D_0 = 1.90$. 72

A.1 k-ω SST turbulence model constants [4]. 91

B.1 Summary of simulation parameters for parametric sensitivity study. 96

List of Figures

1.1 Myer-Cotton classification system for subglottic stenosis (adapted from [26]). 2

1.2 Schematic of human respiratory system [42]. 3

1.3 Variations in breathing time T_B, tidal volume TV, trachea aspect ratio L_T/D_h, and characteristic Reynolds number $\mathrm{Re_D}$ across age ranges. 5

1.4 Variations in dimensionless flow-through time $T_I V_{\mathrm{avg}}/L_T$, and characteristic Womersley number Wo across age ranges. 6

1.5 Schematic of axisymmetric stenotic tube. 7

2.1 CT image projected onto (a) coronal, (b) sagittal, and (c) transverse planes with trachea identified in red; and (d) three-dimensional model reconstructed from scan with the medial axis identified. 19

2.2 Comparison of (a) normal model to artificially-generated stenosis with (b) 44% area reduction, (c) 75% area reduction, and (d) 94% area reduction. 20

3.1 Stenotic trachea model with its medial axis (red) from just upstream of glottis (left) to carina (right). 22

3.2 Scaled hydraulic radius versus scaled distance along the medial axis for the stenotic model. 23

3.3 The base Ricker wavelet and its apparent width w_{app} identified from trough-to-trough distance. 25

3.4 Stenotic tube model with $\varsigma = 0.5$ and $w/D = 1$. 26

3.5 (a) Modified wavelet coefficients T^* and (b) trough indication coefficient T_t at all variations of feature width w/D_0 and feature location z/D_0, for stenotic tube model with $\varsigma = 0.5$ and $w/D = 1$. 27

3.6 Maximum value of trough indicator coefficient T_t for stenotic tube models with $0 < \varsigma < 1$ and $0.4 \leq w/D_0 \leq 2$, with power-law fit indicating a negligible sensitivity to w/D_0. 29

3.7 Scaled hydraulic diameter D/D_0 versus scaled distance along medial axis s/D_0 for a trachea model with stenosis (top panel), and the corresponding trough indicator coefficient T_t for each location s/D_0 and feature width w/D_0 (bottom panel). A "width bar" is shown at the stenosis location indicating its measured width w/D_0. 30

3.8 Identified glottis and stenosis features for baseline model and simulated stenosis models with varying area reductions and stenosis width, indicating measured stenosis area reduction ς and stenosis width w/D_0 indicated on each plot. On each plot, a "width bar" is shown at the stenosis location indicating its measured width w/D_0. 32

4.1 CFD model of stenotic tube for turbulence model validation, showing (a) axisymmetric model, (b) 2D quadrilateral mesh, and (c) near-wall boundary layer refinement. 35

4.2 Centerline velocity scaled by average velocity ($v_c/\bar{v}$) at Re = 2000 computed with different turbulence models compared to experimental data of Ahmed & Giddens [2]. 35

4.3 Scaled wall shear stress ($\tau_w/\rho\bar{v}^2$) at Re = 2000 computed with different turbulence models compared to experimental data of Ahmed & Giddens [2]. 36

4.4 Scaled pressure drop ($\Delta p/\rho\bar{v}^2$) computed with different turbulence models compared to experimental data of Young & Tsai [47]. 37

4.5 Scaled locations of flow separation and reattachment (z/D_0) computed with different turbulence models compared to experimental data of Young & Tsai [47]. 37

4.6 Surface meshes on inlet (left) and wall (right) boundaries of meshes M1-M5 used in mesh sensitivity study. Note that the wall surface mesh shown is a subset of full domain, which extends in both directions. 39

4.7 Integrated and averaged quantities for ideal stenotic tube along the dimensionless axial distance z/D_0, computed on increasingly fine grids at $\mathrm{Re_D} = 2000$. 41

4.8 RMS profile errors for ideal stenotic tube, computed on increasingly fine grids at $\mathrm{Re_D} = 2000$. RMS errors are computed relative to the $\Delta = 6.8$ mesh. 42

4.9 Discrete measurement errors for ideal stenotic tube, computed on increasingly fine grids at $\mathrm{Re_D} = 2000$. 43

5.1 (a) Front and (b) side views of full airway model from nasopharynx to carina, with computational grid shown (c) for inlet boundary and (d) in its entirety. Note the straight domain extension at the outlet to avoid a recirculation region at the imposed boundary condition. 49

5.2 Convergence of total pressure drop over dimensionless time for all full airway simulations, relative to median pressure drop (left panel); and standard deviation of scaled pressure drop for $tV/L > 5$ (right panel) for different Reynolds numbers. 50

5.3 Streamlines for flow in airway from nasopharynx to carina at trachea Reynolds number of 2500. 52

5.4 Integrated and averaged quantities for flow in airway along the dimensionless distance along the medial axis s/D_0, for $500 \geq \mathrm{Re_D} \geq 2500$. 53

5.5 Flow-averaged turbulence intensity $\bar{I}$ and eddy viscosity ratio $\bar{\nu}_t/\nu$ at the glottis cross-section, computed from full upper airway analysis for a range of Reynolds numbers and turbulence boundary conditions. 54

5.6 Models of baseline model and each variation of stenosis to be used in simulations, with stenosis area reduction ς and width w/D_0 measured by wavelet methods of Chapter 3 (compare to Figure 3.8). Note that although the bifurcation is shown here, this portion of the domain is removed for simulations. 56

5.7 Computational mesh at (a) inlet boundary and (b) wall boundary at stenosis, with (c) cross-section of mesh at stenosis. (d) Full model for CFD with straight domain extension at the outlet to avoid a recirculation region at the imposed boundary condition. 57

5.8 Standard deviation of normalized pressure differential for $tV/L > 5$ as a function of area reduction ς (left panel) and Reynolds number $\mathrm{Re_D}$ (right panel). 59

5.9 Examples of stable and unstable simulations, as qualified by the standard deviations of normalized pressure differential for $tV/L > 5$. The relative amplitudes of oscillation correlate positively with the standard deviations σ, and oscillations may occur with discrete modes or with broadband frequency content. 60

5.10 Relative velocity magnitude (scaled by median velocity V) contours on cross-sections of stenotic trachea for six instantaneous times ($t_1 < t_2 < \cdots < t_6$) for flow field with broadband frequency content ($\sigma = 3.34 \times 10^{-2}$), as shown in Figure 5.9. 61

5.11 Visualization of skin friction coefficient (left panel), pressure coefficient (middle panel), and velocity streamlines colored by z-velocity normalized with respect to the median velocity V (right panel). 62

5.12 Integrated and averaged quantities for flow in stenotic trachea ($\varsigma = 0.905$, $w/D_0 = 1.145$) along the dimensionless distance along the medial axis s/D_0, for $500 \leq \mathrm{Re_D} \leq 2400$. 64

5.13 Minimum pressure coefficient $\bar{C}_{p,\min}$ and maximum skin friction coefficient $\bar{C}_{f,\max}$ for all simulations versus area reduction ς. A 95% confidence interval is indicated with error bars. 65

5.14 Scaled length of separation region immediately behind glottis $L_{\mathrm{sep,g}}/D_0$ and immediately behind stenosis $L_{\mathrm{sep,s}}/D_0$ for all simulations versus area reduction ς. A 95% confidence interval is indicated with error bars. 66

5.15 Loss coefficient K as a function of area reduction ς, compared to the loss coefficient of an orifice plate given in Eq. (5.13). A 95% confidence interval is indicated with error bars. 67

5.16 Data and least-squares best fits for loss coefficient functions $K_0(\varsigma)$ and $K_1(\varsigma, w/D_0)$ as a primary function of ς. A 95% confidence interval is shown for each value of K_0, and each data point of K_1 is colored by its corresponding value of w/D_0. 70

5.17 Relative flow rate Φ for stenosis area reductions ς, with 95% confidence interval on full data set. Analytical correlations are presented for two stenosis widths $w/D_0 = 0.75$ and $w/D_0 = 1.90$. Myer-Cotton Grades I-III are indicated as three regions of area reduction. 71

5.18 Volumetric flow rate $\dot{V}$ and total pressure drop ΔP over time for sinusoidal flow simulation in stenosis model with $\varsigma = 0.76$ and $w/D_0 = 1.75$, with corresponding stationary flow results for comparison... 73

5.19 Contours of velocity magnitude |v| for stenotic trachea ($\varsigma = 0.76$, $w/D_0 = 1.75$) from simulation of sinusoidal inspiration. 75

5.20 Relationship between instantaneous loss coefficient K and instantaneous Reynolds number $\mathrm{Re_D}$ for sinusoidal inflow simulation, compared to the data of the stationary inflow simulation and the stationary inflow correlation of Eq. (5.14). 76

B.1 Inlet boundary plane (left) with the outer radius function $R(\theta)$, scaled by the hydraulic diameter, and (right) dimensionless wall distance y/D_h plotted on the inlet boundary..... 93

B.2 Examples of Gaussian-biased inlet velocity profiles with power-law base profile ($n = 8$), with 6 variations of bias angle. Dotted lines indicating the bias angle are shown for reference..... 94

B.3 (a) Illustration of inflow directivity parameters on a generic inlet boundary plane with tangent vector $\vec{t}$, normal vector $\vec{n}$, angle of incidence ϕ, and azimuthal angle ψ. (b) Maximum possible angle of incidence $2\phi \approx 46^\circ$ measured from superglottic region of airway model. 95

B.4 Minimum pressure coefficient $\bar{C}_{p,\mathrm{min}}$ and maximum skin friction coefficient $\bar{C}_{f,\mathrm{max}}$ for all simulations versus area reduction ς, with all variations of inflow condition. A 95% confidence interval is indicated with error bars..... 97

B.5 Loss coefficient K and relative flow rate Φ as a function of area reduction ς, with all variations of inflow condition. A 95% confidence interval is indicated with error bars. Myer-Cotton Grades I-III are indicated as three regions of area reduction. 98

Abstract

Laryngotracheal stenosis (LTS) is a health condition in which an obstruction in the upper trachea can cause breathing difficulties and increased incidence of infection, among other symptoms. Occurring most commonly due to intubation in infants, LTS often requires corrective surgery. Currently, clinical methods of assessing the blockage region are simplistic and subjective, and it is challenging to determine the most effective surgical strategy for any given patient. In the present work, a comprehensive methodology is proposed for characterizing the stenosis region both in terms of its anatomical parameters and its corresponding aerodynamic properties. The combination of computational fluid dynamics (CFD) and medical imaging provides a non-invasive method for establishing these relationships between anatomy and aerodynamics. As software packages for such analyses have matured in recent years, computational approaches to solving medical problems have gained more widespread appeal. While patient-specific CFD has gained recent popularity, the approach presented in the present work aims to generate parametric correlations which may be applied to any member of a class of patients. These correlations may be used clinically to provide data-driven recommendations for surgical procedures.

Chapter 1
Introduction

1.1. Background and Problem Description

Laryngotracheal stenosis (LTS) is the most common long-term complication of tracheal intubation in children [6]. The pressure exerted on the inner surfaces of the trachea by an endotracheal tube (ETT) can cause superficial ulceration resulting in a buildup of scar tissue, which represents a localized narrowing of the lumen (air volume) of the trachea. This localized narrowing is referred to as a stenosis. Symptoms of LTS include dyspnea (labored breathing), stridor (noisy breathing), increased incidence of infection such as pneumonia, and – in extreme cases – airway collapse.

Otolaryngologists evaluate LTS endoscopically and manage symptomatic cases surgically. The standard evaluation of a stenosis is anatomical, based on the qualitative Myer-Cotton grading system [26]. A stenosis is classified as Grade I-IV according to the percent area reduction relative to the nominal area, as illustrated in Figure 1.1. While this system was originally based on measuring the fitments of different diameters of endotracheal tubes upon intubation, modern clinical classification is based on visual estimation. Published studies report success rates of laryngotracheal reconstruction (LTR) surgeries ranging from 50-95% [23], depending on the severity of the condition. The success of a LTR procedure is usually measured by decannulation – that is, successful removal of tracheostomy tube where the patient is able to breathe self-sufficiently. Patients who are successfully decannulated often have persistent airway symptoms. Such patients are at increased risk of reactive airway disease, recurrent respiratory tract infection, and recurrent airway obstruction.

Since anatomical success of LTR surgery as-qualified by the Myer-Cotton grading system does not seem to be a sufficient indicator of physiological success, the physics of trachea airflow should be considered in order to draw a more direct relationship from anatomy to physiology.

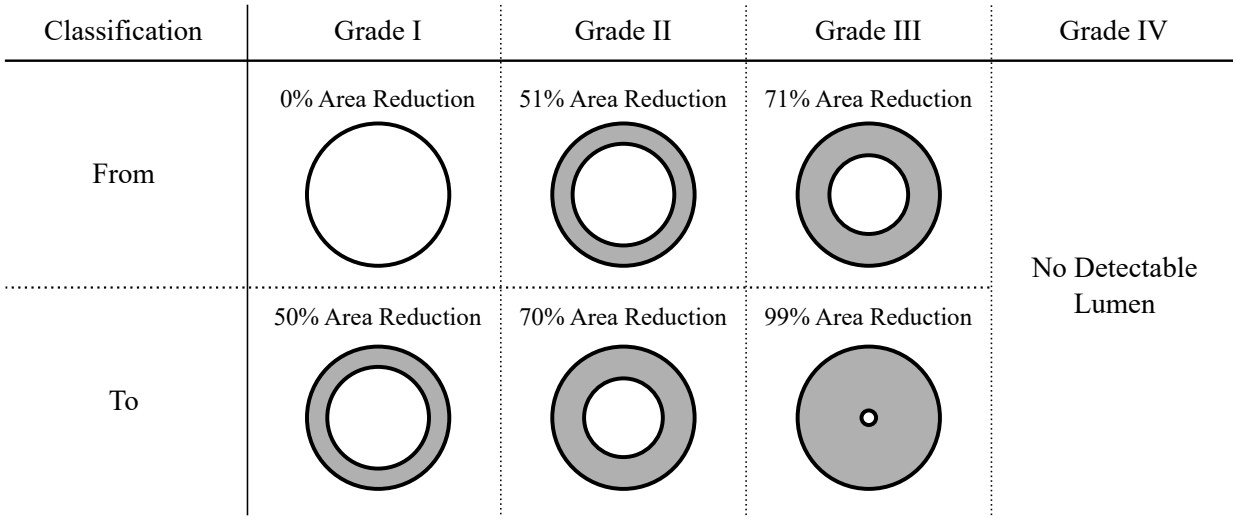

Figure 1.1. Myer-Cotton classification system for subglottic stenosis (adapted from [26]).

1.2. Anatomy of the Human Airway

The human respiratory system is typically separated into the upper and lower respiratory tracts, as illustrated in Figure 1.2. The upper respiratory tract is comprised of the nasal cavity, the pharynx, and the larynx. The nasopharynx and oropharynx are the regions of the pharynx behind the nasal cavity and oral cavity, respectively. The larynx, commonly referred to as the "voice box," contains the vocal folds. The opening between the vocal folds is referred to as the glottis. The lower respiratory tract is comprised of the trachea, the bronchi, and the lungs. The lowest point of the trachea, where the bifurcation occurs, is referred to as the carina. It should be noted that most of the superglottic (above the glottis) tissues are easily-deformable, and tend to change shape during the breathing cycle. Conversely, the subglottic (below the glottis) larynx, trachea, and bronchi are comparatively rigid structures.

1.3. Statistics of Pediatric Ventilation

In order to better understand physical quantities related to ventilation (breathing), it is appropriate to conduct a survey of overall anatomical and airflow parameters. The most basic parameters for ventilation are the mean respiratory rate MRR and the tidal volume TV, which indicate the number of breaths per minute and the total volume of air inhaled

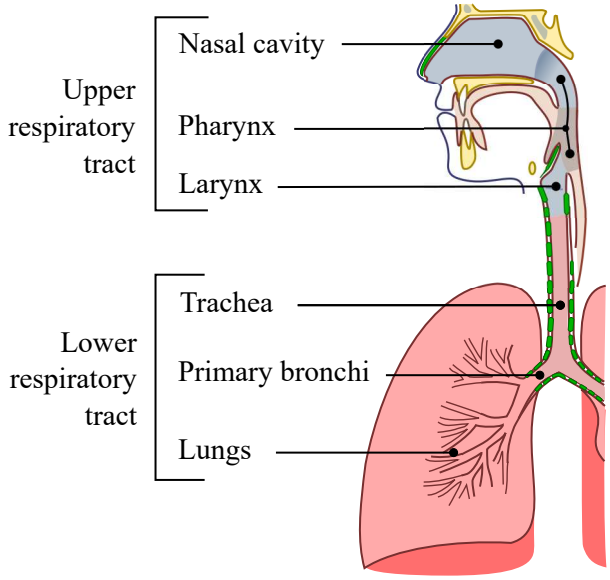

Figure 1.2. Schematic of human respiratory system [42].

Table 1.1. Variations in mean respiratory rate across age groups [9]

Age	MRR [min^{-1}]	Age	MRR [min^{-1}]
$0-6$ mo.	42	$3-4$ yr.	26
$6-12$ mo.	40	$4-6$ yr.	24
$12-18$ mo.	37	$6-12$ yr.	20
$18-24$ mo.	33	$12-18$ yr.	17
$2-3$ yr.	29		

and exhaled over one respiratory cycle, respectively. The mean respiratory rate (MRR) across different age groups is tabulated in Table 1.1.

The time for one complete respiratory cycle T_B (inspiration and expiration) is the reciprocal of MRR by

$$T_B = \text{MRR}^{-1} \tag{1.1}$$

The tidal volume is directly correlated to the ideal body weight based on age and sex, and is approximately 7 cm^3/kg of ideal body weight [30]. The ideal body weight used to calculate the tidal volume is based on World Health Organization standards [44], not the patient's actual weight.

The normal respiratory cycle is well-represented by a sinusoid [17], although this wave-

Table 1.2. Dimensional variations of trachea with respect to age [10]

Age [yrs]	Length [cm]	AP Dia. [cm]	Transv. Dia. [cm]	Open Area [cm^2]
$0-2$	5.4	0.53	0.64	0.28
$2-4$	6.4	0.74	0.81	0.48
$4-6$	7.2	0.80	0.90	0.58
$6-8$	8.2	0.92	0.93	0.69
$8-10$	8.8	1.05	1.07	0.89
$10-12$	10.0	1.16	1.18	1.10
$12-14$	10.8	1.30	1.33	1.39

form may be distorted by some disease. Assuming the respiratory flow rate $Q(t)$ follows a sinusoidal function of time, the maximum flow rate $Q_{\max}$ and average flow rate Q_{avg} are related to tidal volume TV and mean respiratory rate MRR as

$$Q_{\max} = \pi\,(\text{TV} \times \text{MRR})\,, \qquad Q_{\text{avg}} = 2\,(\text{TV} \times \text{MRR}) \tag{1.2}$$

Published statistics of airway dimensions [10] tabulated in Table 1.2 may be used to further estimate flow characteristics. Characteristic airflow velocities of the average trachea cross-section at peak inspiration flow rates $V_{\max}$ and average inspiration flow rates V_{avg} may be calculated as

$$V_{\max} = \frac{Q_{\max}}{A_{\text{avg}}}, \qquad V_{\text{avg}} = \frac{Q_{\text{avg}}}{A_{\text{avg}}} \tag{1.3}$$

where A_{avg} is the average cross-sectional area of the lumen of the trachea, from Table 1.2. In order to better understand the flow regimes involved in inspiration, we may also compute Reynolds number based on the average hydraulic diameter D_h and maximum velocity $V_{\max}$.

$$\text{Re}_{\text{D}} = \frac{V_{\max} D_h}{\nu_{\text{air}}} \tag{1.4}$$

Another important parameter governing the fluid dynamics of the trachea is the aspect ratio L_T/D_h, where L_T is the trachea length and D_h is the average hydraulic diameter of the

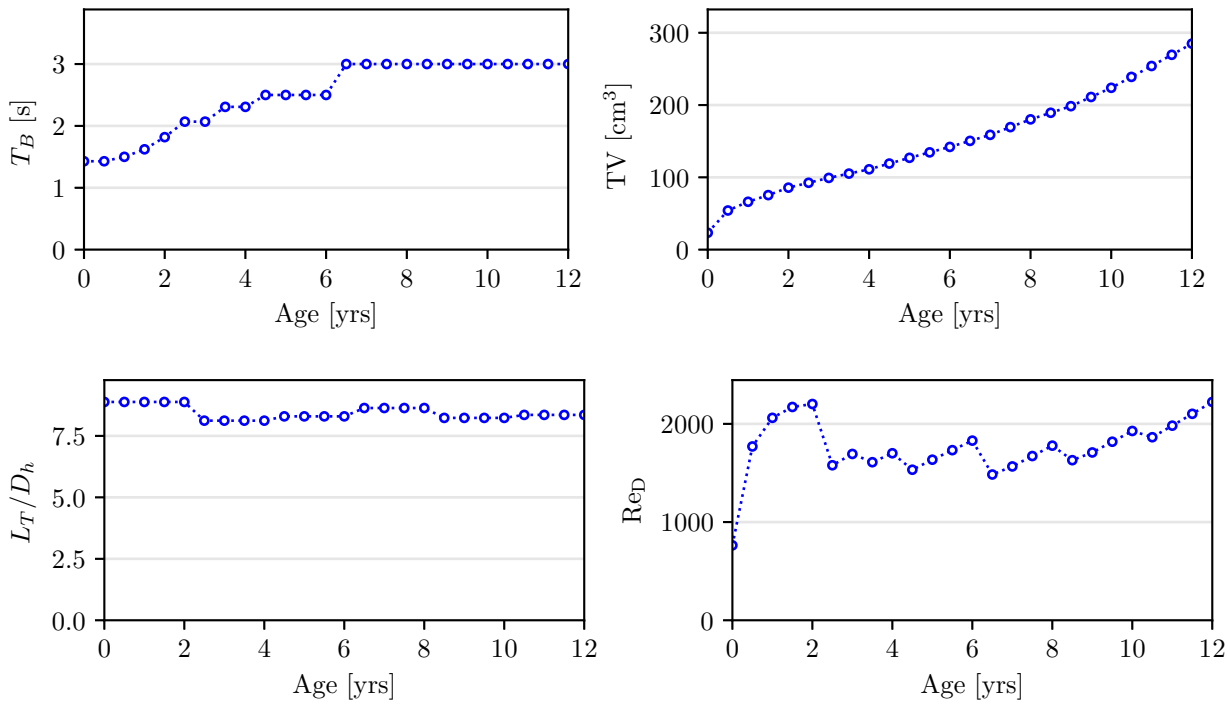

Figure 1.3. Variations in breathing time T_B, tidal volume TV, trachea aspect ratio L_T/D_h, and characteristic Reynolds number $\mathrm{Re_D}$ across age ranges.

trachea, calculated by assuming the trachea is elliptic from the two diameters given in Table 1.2. The time for one breath T_B, tidal volume TV, aspect ratio L_T/D_h and characteristic Reynolds number $\mathrm{Re_D}$ based on maximum flow rate and average trachea dimensions are shown over ages $0-12$ years in Figure 1.3. The aspect ratio remains relatively constant across the age groups; thus, leading-order geometric similarity is maintained throughout early development. The characteristic Reynolds number indicates that the flow may be turbulent (typically a $\mathrm{Re_D} > 2300$ for internal flows in ducts), especially in the case of a localized area reduction. Figure 1.4 shows variations in the dimensionless flow-through time and Womersley number over ages $0-12$. The dimensionless flow-through time indicates how many times a particle may traverse the trachea in one inspiration time period. The Womersley number Wo is a dimensionless ratio of the oscillatory flow momentum to viscous momentum diffusion, defined as

$$\mathrm{Wo} = \sqrt{\frac{\omega D^2}{\nu}} \tag{1.5}$$

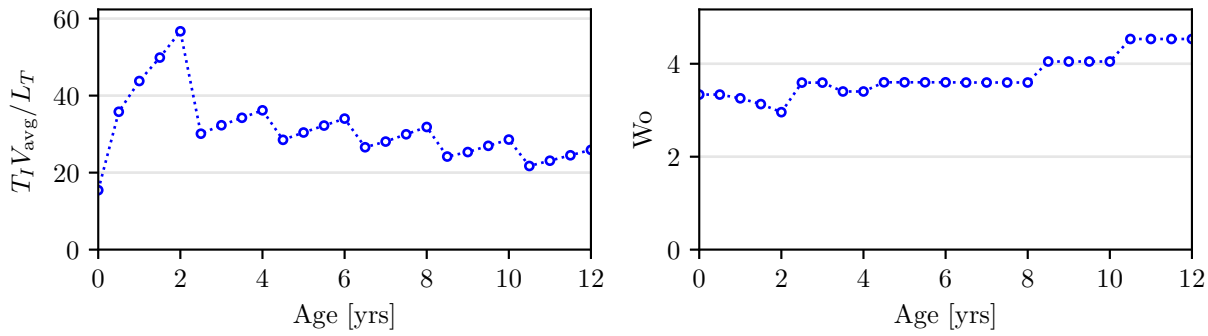

Figure 1.4. Variations in dimensionless flow-through time $T_I V_{\text{avg}}/L_T$, and characteristic Womersley number Wo across age ranges.

where ω is the angular frequency of the oscillations, ν is the kinematic viscosity, and D is the hydraulic diameter of the pipe. The Womersley number based on nominal trachea dimensions and average breathing frequencies is $3 < \text{Wo} < 4.5$, assuming that the flow profile is sinusoidal. To leading order, this indicates that a quasi-steady approximation of trachea flows is appropriate; however, transient effects may still be present [43].

1.4. Literature Survey

Presently, there is a wealth of information on the computational analysis of airways within the research literature. Primary applications of CFD in human airways are in quantifying particle deposition for drug delivery [13, 36, 38] and understanding obstructive sleep apnea [15, 20, 21]. Computational studies of tracheal stenosis do exist [7, 14]; however, they do not sufficiently answer the questions posed in the present work, as discussed later in Section 1.5.

1.4.1. Stenotic Tube Model

A majority of the studies on fluid dynamics of stenotic geometries is motivated by blood flows [2, 12, 22, 32, 39, 40, 45, 46, 47, 48]. Although the problem of arterial blood flow involves a different fluid, different length scales, and different velocity scales from tracheal air flow, the flow regimes characterized by Reynolds number are similar. Although blood is typically cited as an example of a Non-Newtonian fluid, it may be approximated as a Newtonian fluid in the arteries due to the higher rates of shear [19]. Furthermore, most

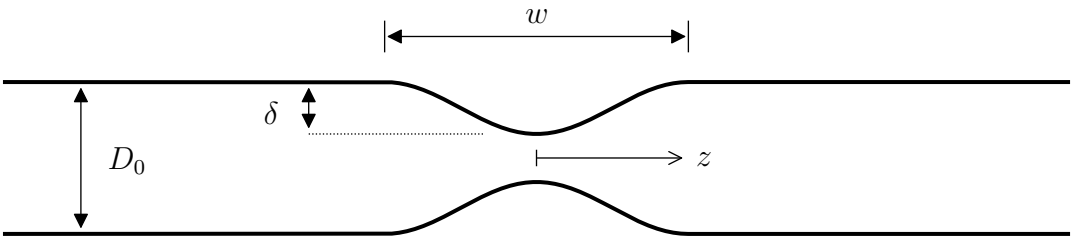

Figure 1.5. Schematic of axisymmetric stenotic tube.

studies of arterial stenosis have studied the characteristics of Newtonian fluids as a leading-order approximation. Thus, the simplified models used to study arterial stenosis scale well to the problem of tracheal stenosis.

The fluid dynamics of arterial stenosis were first studied around 1970 both experimentally [47] and analytically [45]. Rather than try to analyze arterial stenosis in anatomically-precise detail, the problem was simplified by introducing the axisymmetric stenotic tube model. This model consists of a straight, axisymmetric tube with a localized constriction described by a cosine curve, as illustrated in Figure 1.5. The diameter $D(z)$ of the axisymmetric stenotic tube is defined mathematically as

$$\frac{D(z)}{D_0} = \begin{cases} 1, & |z| > w/2 \\ 1 - \frac{1}{2}\left(\frac{\delta}{D_0}\right)\left(1 + \cos\left(\frac{2\pi z}{w}\right)\right), & |z| \leq w/2 \end{cases} \tag{1.6}$$

where z is the distance from the most constricted location along the axis of the tube, D_0 is the nominal diameter, w is the stenosis width/wavelength, and δ is the height of the obstruction from the nominal wall location. Here,

$$\frac{\delta}{D_0} = 1 - \sqrt{1 - \varsigma} \tag{1.7}$$

where ς is the percent area reduction at the most constricted location ($z = 0$).

In 1974, Young & Morgan used an integral method [45] with approximate velocity profiles to develop a nonlinear ordinary differential equation governing steady flow in a

stenotic tube, which was then solved numerically to predict velocity profiles, wall shear stresses, and flow separation/reattachment lengths. Unfortunately, this approach is only applicable to laminar flows, but the result is useful nonetheless. The theoretical results show that even a mild stenosis can cause an alteration in flow characteristics, and that the effect generally becomes more appreciable as the Reynolds number increases. A stenosis with 89% area reduction can cause an order-of-magnitude increase in the maximum shearing stress at low Reynolds numbers (Re $\sim$ 20) and two orders of magnitude at Re $\sim$ 100. It was also shown that flow separation in the diverging section produces a reversed wall shear stress that can extend many diameters downstream of the stenosis.

Young and Tsai experimentally characterized the steady-flow pressure drop, flow separation, and onset of turbulence for the axisymmetric stenotic tube for Reynolds numbers between 100-5000, as well as for some asymmetric stenotic tube models [47]. From their experiments, they proposed a correlation for the pressure drop Δp as

$$\frac{\Delta p}{\rho U^2} = \frac{K_v}{\mathrm{Re}} + \frac{K_t}{2}\left(\frac{\varsigma}{1-\varsigma}\right)^2 \tag{1.8}$$

where K_v and K_t are constants for a given geometry and ς is the maximum percent reduction in area. Upon fitting the experimental data to this form, they obtained values of K_v and K_t given in Table 1.3. The parameter fits for models M-2 and M-3 are indeed the same; that is, the pressure drop of the 89% area-reduction model was found to be insensitive to the stenosis width. Also, the inertial-type losses modeled by K_v are close to the analytical result for sudden expansions. The laminar separation and reattachment locations were measured through near-wall dye injection and visual inspection of separation streamlines. The results matched the laminar analytical results from the integral method [45].

In 1983, Ahmed & Giddens [2] published experimental measurements of the velocity profiles in axisymmetric stenotic tubes for Reynolds numbers from 500-2000. With more sophisticated instruments than Young & Tsai, they measured the instantaneous and av-

Table 1.3. Pressure loss coefficients from axisymmetric stenotic tube experiments (adapted from [47]).

Model	Area reduction, ς	w/D_0	K_v	K_t
M-1	0.56	4	700	0.9
M-2	0.89	4	4500	0.9
M-3	0.89	2	4500	0.9
Laminar	0	–	$32\,(L/D)$	0
Sudden Expansion	–	–	0	1

eraged velocity fields at different locations, and estimated the local wall shear stress from velocity profiles.

More recently, direct numerical simulations (DNS) have been used to study the stability, transition, and turbulent structures of stenotic flows [32, 39, 40]. Varghese et al [39] found that wall shear stresses at the stenosis throat can exceed upstream levels by more than a factor of 30. They also found that a small geometric perturbation – where the stenotic constriction is not coaxial within the tube – can result in an appreciable bias in the post-stenosis flow field. The turbulent jet breakdown in the eccentric model occurs considerably sooner than the axisymmetric model. Thus, small perturbations in geometric parameters can drastically affect the fluid dynamics.

1.4.2. Computational Aerodynamics in Airways

In the airway analysis literature, many studies have been devoted to understanding the fluid dynamics of obstructive sleep apnea [15, 20, 21]. Taherian used CFD to study the aerodynamics of aerosol drug delivery in the case of tracheal stenosis [36] and excessive dynamic airway collapse with fluid-structure interaction (FSI) models [35]. Mylavarapu used CFD in planning upper airway surgery by analyzing geometric variants representing "virtual surgeries" [27]. Brouns et al. used CFD to investigate the flow dynamics of tracheal stenosis with respect to different degrees of area restriction [7] on a 3D model representative of real anatomy. Here, a relationship between pressure differential and flow rate was developed for several variations of stenosis area reduction and two variations of the stenosis

length. A power-law relationship was found between pressure differential ΔP and flow rate Q as $\Delta P \sim Q^n$. The best-fit exponent was found to be $n = 1.77$ for the unobstructed trachea model and $n = 1.92 - 2.00$ for the obstructed trachea models. They found that the pressure drop corresponding to a 40% area reduction is negligible with respect to a 70% area reduction, and concluded that their power-law models could be used as a diagnostic tool for noninvasively evaluating the airflows of stenosis patients.

In these studies, Large Eddy Simulations (LES) and Reynolds-Averaged Navier-Stokes (RANS) simulations were used to model the naturally-occurring turbulent structures in the airflows. Experimental validation of such turbulence models [28, 34] for upper airway flows have shown that the RANS k-ω Shear Stress Transport (SST) turbulence model correlated most strongly with experimental data, while the RANS standard k-ε model gave the least accurate results. The LES models tended to provide slightly more accurate results at the cost of significantly increased computational effort.

1.5. Study Objectives

Currently, clinical manifestations (i.e. symptoms) are correlated directly to the airway anatomy via the visual classification system and empirical "rules of thumb". The overall objective of this work is to develop a more rigorous and physics-based correlation by relating the anatomy of an airway to the aerodynamics, which can be related directly to clinical manifestations. Specific objectives of this work include the following:

(i) Develop a methodology for computational analysis of air flows in the trachea,

(ii) Select and quantify the anatomical features relevant to flow dynamics in the trachea,

(iii) Propose aerodynamic metrics indicative of breathing performance and quantify from numerical simulations,

(iv) Correlate the anatomical and aerodynamic performance parameters,

(v) Identify and characterize the prominent flow structures of tracheal stenosis.

The potential impact of this study is that physicians will have a more thorough understanding of what is important in the shape of the airway, as well as a clearer description of

the sensitivities of aerodynamics to anatomical variations. Thus, surgical decisions can be made based on quantifiable knowledge of the benefits related to the procedural risks and costs.

The present study can be considered as an extension to the study of Brouns et al. [7], which presented flow correlations for stenotic trachea for several variations in stenosis geometry. The present study aims to contribute to the research literature by proposing correlations in dimensionless terms which should apply well across different age groups. By connecting these dimensionless correlations to existing classification methods (i.e. Myer-Cotton), the results of the present study will be readily actionable in future studies in either medical or engineering settings. The present study also proposes a robust method for measuring the anatomical dimensions of a stenosis from a CT scan, which to the knowledge of the author has not yet been attempted.

Chapter 2
Modeling & Numerical Methods

This chapter describes the basic theory of computational fluid dynamics and turbulence modeling and outlines the methodology for generating analyzable models of human trachea.

2.1. Computational Fluid Dynamics (CFD)

The fundamental equations of fluid dynamics – the Navier-Stokes equations – are well-studied and have been found to be be extremely reliable models of fluid motion in most practical applications. For a general fluid of constant density ρ and kinematic viscosity ν with velocity field $\hat{u}_i(\vec{x}, t)$ (with $i = 1, 2, 3$) and pressure field $\hat{p}(\vec{x}, t)$, the incompressible, isothermal Navier-Stokes equations may be written using tensor notation as

$$\frac{\partial \hat{u}_i}{\partial x_i} = 0, \qquad \frac{\partial \hat{u}_i}{\partial t} + \hat{u}_j \frac{\partial \hat{u}_i}{\partial x_j} = -\frac{1}{\rho}\frac{\partial \hat{p}}{\partial x_i} + \frac{\partial}{\partial x_j}\left[\nu\left(\frac{\partial \hat{u}_i}{\partial x_j} + \frac{\partial \hat{u}_j}{\partial x_i}\right)\right] \tag{2.1}$$

Unfortunately, these equations are unable to be solved exactly in most cases. Instead, approximate solutions are sought by solving the Navier-Stokes equations on a finite grid using computers. Additional issues arise in this Computational Fluid Dynamics (CFD) approach; special care must be taken to adequately resolve the flow structures at each length scale. At relatively high flow velocities, this set of equations may give rise to multi-scale turbulent structures, producing features so small that their computation becomes impractical, thereby requiring the implementation of turbulence models.

2.1.1. Turbulence

In general, a fluid flow may be categorized as laminar, turbulent, or transitional between laminar and turbulent. While laminar flows are characterized by smooth, sheet-like motion of fluid layers, turbulent flows are characterized by chaotic behaviors which fluctuate over time. Laminar flows are considerably easier to analyze, but most flows in nature are turbulent. The key dimensionless parameter to characterize the flow regime is the Reynolds

number $\mathrm{Re_D}$, defined as

$$\mathrm{Re_D} = \frac{VD}{\nu} \tag{2.2}$$

where V and D are characteristic velocity and length scales of the flow, and $\nu \equiv \mu/\rho$ is the kinematic viscosity of the fluid. For internal flows in constant-area ducts, V is the area-averaged velocity and D is the hydraulic diameter of the passage. Most internal flows in constant-area ducts transition between laminar and turbulent behavior in the neighborhood of $\mathrm{Re_D} = 2300$.

2.1.2. Reynolds-Averaged Navier-Stokes (RANS) Equations

In order to analyze turbulent flows, a common approach is to use the Reynolds decomposition to separate a time-varying signal into mean and fluctuating components. Defining the ensemble average (notated by angular brackets) of a time-varying signal $\hat{\phi}(t)$ as the instantaneous average over a large collection of N imaginary experiments

$$\langle \hat{\phi}(t) \rangle \equiv \frac{1}{N} \sum_{n=1}^{N} \left[\hat{\phi}(t) \right]^{(n)} \tag{2.3}$$

where the superscript (n) indicates the nth experiment. We may decompose the signal $\hat{\phi}_i$ into the sum of its mean ($\Phi_i \equiv \langle \hat{\phi}_i \rangle$) and its fluctuations ($\phi_i'$) about the mean:

$$\hat{\phi}_i \equiv \Phi_i + \phi_i' \tag{2.4}$$

Using a Reynolds decomposition of velocity ($\hat{u}_i \equiv U_i + u_i'$) and pressure ($\hat{p} \equiv P + p'$) and taking the ensemble average of the Navier-Stokes equations, we obtain the Reynolds-averaged Navier-Stokes (RANS) equations, which are written in tensor notation as

$$\frac{\partial U_i}{\partial x_i} = 0, \qquad \frac{\partial U_i}{\partial t} + U_j \frac{\partial U_i}{\partial x_j} = -\frac{1}{\rho}\frac{\partial P}{\partial x_i} + \frac{\partial}{\partial x_j}\left[\nu \left(\frac{\partial U_i}{\partial x_j} + \frac{\partial U_j}{\partial x_i} \right) - \langle u_i' u_j' \rangle \right] \tag{2.5}$$

We note here that this equation is identical to the non-averaged Navier-Stokes equations of Eq. (2.1), albeit with one additional term, $-\langle u_i' u_j' \rangle$, commonly referred to as the Reynolds

stress [29]. It is common to define the turbulence kinetic energy (TKE, or k) in terms of the trace of the Reynolds stress

$$k \equiv \frac{\langle u_i' u_i' \rangle}{2} \tag{2.6}$$

Since there is no exact way to calculate the Reynolds stresses, we must use some approximations to close the problem mathematically. For more information on Reynolds averaging and the RANS equations, refer to an advanced text on fluid dynamics or turbulence [18, 29].

2.1.3. Turbulence Modeling

The Boussinesq hypothesis is often used to estimate the Reynolds stresses by relating them to the mean velocity gradients with an eddy viscosity ν_t:

$$-\langle u_i' u_j' \rangle = \nu_t \left(\frac{\partial U_i}{\partial x_j} + \frac{\partial U_j}{\partial x_i} \right) - \frac{2}{3} \left(k + \nu_t \frac{\partial U_k}{\partial x_k} \right) \delta_{ij} \tag{2.7}$$

For the incompressible RANS equations, we may then write the averaged momentum equation as

$$\frac{\partial U_i}{\partial t} + U_j \frac{\partial U_i}{\partial x_j} = -\frac{1}{\rho} \frac{\partial P}{\partial x_i} + \frac{\partial}{\partial x_j} \left[(\nu + \nu_t) \left(\frac{\partial U_i}{\partial x_j} + \frac{\partial U_j}{\partial x_i} \right) - \frac{2}{3} k \delta_{ij} \right] \tag{2.8}$$

Introducing another variable, ε, as the mass-specific kinetic energy dissipation rate at the smallest scales of turbulence (SI units of W/kg, or $\mathrm{m}^2/\mathrm{s}^3$), we may relate the eddy viscosity to k and ε by dimensional analysis:

$$\nu_t \sim \frac{k^2}{\varepsilon} \tag{2.9}$$

Rather than using k and ε, the k-ω model uses a specific eddy dissipation rate $\omega \equiv \varepsilon / k$. Then, the eddy viscosity ν_t is calculated by introducing a proportionality coefficient α:

$$\nu_t = \frac{\alpha k}{\omega} \tag{2.10}$$

where the coefficient α may be a constant or function of the flow field, depending on the specific model. Then, the semi-empirical transport equations for k and ω may be written

in tensor notation as

$$\frac{\partial k}{\partial t} + U_i \frac{\partial k}{\partial x_i} = \frac{\partial}{\partial x_j}\left[\left(\nu + \frac{\nu_t}{\sigma_k}\right)\frac{\partial k}{\partial x_j}\right] + G_k - Y_k \tag{2.11}$$

$$\frac{\partial \omega}{\partial t} + U_i \frac{\partial \omega}{\partial x_i} = \frac{\partial}{\partial x_j}\left[\left(\nu + \frac{\nu_t}{\sigma_\omega}\right)\frac{\partial \omega}{\partial x_j}\right] + G_\omega - Y_\omega + D_\omega \tag{2.12}$$

where G_k and G_ω represent the generation of k and ω, Y_k and Y_ω represent the dissipation of k and ω due to turbulence, and D_ω represents the cross-diffusion term. Note here that the subscripts k and ω do not refer to tensor indices. The precise formulation of these terms determines the "flavor" of the k-ω model. In the Shear-Stress Transport (SST) k-ω model, the cross-diffusion term D_ω effectively blends the k-ω and k-ε models together, attempting to provide the most beneficial aspects of both models. Details of the k-ω SST turbulence model may be found in Appendix A and in the ANSYS Fluent documentation [4].

2.1.4. Scale Analysis

Additional insight into the eddy-viscosity momentum equation of Eq. (2.8) can be found by scaling the physical variables to be order unity. The nominal hydraulic diameter D and average breathing time T provide natural length and time scales. The velocity U_i may be scaled with the velocity V corresponding to a nominal cross-sectional area. Since it is expected that pressure gradients be proportional to the flow inertia, the pressure is scaled with ρV^2. The turbulent kinetic energy k may be scaled with V^2, based on its definition. From on these scales, a set of dimensionless variables is defined:

$$x_i^* = \frac{x_i}{D}, \qquad t^* = \frac{t}{T}, \qquad U_i^* = \frac{U_i}{V}, \qquad P^* = \frac{P}{\rho V^2}, \qquad k^* = \frac{k}{V^2} \tag{2.13}$$

The eddy-viscosity momentum equation is non-dimensionalized:

$$\frac{1}{2\pi}\frac{\mathrm{Wo}^2}{\mathrm{Re_D}}\frac{\partial U_i^*}{\partial t^*} + U_j^*\frac{\partial U_i^*}{\partial x_j^*} = -\frac{\partial P^*}{\partial x_i^*} + \frac{\partial}{\partial x_j^*}\left[\left(\frac{1+\nu_t/\nu}{\mathrm{Re_D}}\right)\left(\frac{\partial U_i^*}{\partial x_j^*} + \frac{\partial U_j^*}{\partial x_i^*}\right) - \frac{2}{3}k^*\delta_{ij}\right] \tag{2.14}$$

where Wo is the Womersley number defined in Eq. (1.5), $\mathrm{Re_D}$ is the Reynolds number, and ν_t/ν is the eddy viscosity ratio. It is evident from this scaling that transient effects of the average flow field may be negligible when $\mathrm{Wo}^2/2\pi\mathrm{Re_D} \ll 1$. Indeed, the statistics presented in Section 1.3 give

$$\mathcal{O}\left(\frac{1}{2\pi}\frac{\mathrm{Wo}^2}{\mathrm{Re_D}}\right) = 10^{-3}. \tag{2.15}$$

Hence, it is expected that an instantaneous flow field within the trachea during a sinusoidal respiration cycle should be well-represented by a stationary flow field – that is, with time-independent boundary conditions. This expectation is explored further in Section 5.6.

While it is expected that the instantaneous flow field is largely uninfluenced by the long time scales of respiration, it is possible that oscillations on shorter time scales will cause mean-flow unsteadiness. In fact, it is shown in Section 5.3.2 that hydrodynamic instabilities give rise to oscillations on a much shorter time scale than the breathing cycle.

2.1.5. Boundary Conditions

For two-equation turbulence models, two additional boundary conditions are needed. It is typical to specify the turbulence intensity I and the eddy viscosity ratio EVR at a boundary as

$$\mathrm{I} = \frac{\sqrt{2k/3}}{U_0}, \qquad \mathrm{EVR} = \frac{\nu_t}{\nu} \tag{2.16}$$

where U_0 is the average velocity at the boundary. The eddy viscosity ratio is the ratio of turbulent stresses to mean viscous stresses – indicating the overall effect of the turbulence model – while the turbulence intensity is the average turbulent fluctuation amplitude relative to the mean-flow velocity. The inlet RANS turbulence model quantities k and ω (or k and ε) can be fully specified from these two quantities. Unfortunately, there is no unique method for specifying turbulence intensity and eddy viscosity ratio other than by rule-of-thumb; thus, their sensitivities should be taken into account for any study. The turbulence intensity may in some cases be measured from experiments, and is typically very low ($\mathrm{I} \ll 1\%$) for flows initially at rest, such as the flow drawn into the nostrils from

ambient air.

2.1.6. Numerical Methods

All computational fluid dynamics simulations described in this study were performed using ANSYS Fluent 17 [4], a commercial finite-volume method (FVM) numerical solver. All computational grids were created using ANSYS ICEM CFD or ANSYS Meshing, as described for each application in Chapters 4 and 5. A second-order upwind spatial discretization was used for each transport equation, and a bounded second-order implicit time discretization was used for each transient simulation. A least-squares, cell-based method was used to compute gradients and a second-order method was used to calculate the pressure at cell interfaces. Since a pressure-based algorithm is used to solve the incompressible flow equations, a coupled pressure-velocity scheme was used to satisfy the continuity constraint while solving the momentum equations [4].

2.1.7. Solution Initialization

For the simulations described in this report, the initial condition is provided by the Hybrid Initialization routines of ANSYS Fluent [4]. The velocity field is initialized using potential flow theory, which satisfies the no-penetration condition at the wall boundaries and provides cursory flow paths, but does not satisfy the no-slip condition at the walls. The pressures and turbulence quantities are initialized as constant from the inlet boundary. It should be noted that this method provides an unphysical initial condition to the initial-boundary-value problem of transient fluid flow, since the no-slip condition is not satisfied at wall boundaries initially. Thus, a time-accurate transient solution initialized from this condition cannot be trusted for small time. For any transient solution with constant boundary conditions, it is assumed and verified that the flow converges to either a steady state or a stable limit-cycle in finite time, after which the solution may be considered to be independent of the initial condition.

2.2. Airway Model Generation

The three-dimensional trachea models used in CFD analysis are generated from computed tomography (CT) scans of real airways using the Simpleware ScanIP software. The data structure of a CT image is a three-dimensional grid of voxels (volumetric pixels), each with a value of Hounsfield units indicating normalized radiation absorption from the CT scan – i.e. an indicator of how "open" that portion of the volume is. By identifying a point in the trachea lumen and a threshold Hounsfield value, the trachea lumen is identified as a contiguous set of voxels. Figure 2.1a-c illustrates the identification of the trachea from a CT image projected onto coronal, sagittal, and transverse planes. The set of voxels identified as the trachea lumen is then used to create a triangulated surface mesh (".stl" file format). From the resultant surface model, the medial axis, or "skeleton", is also computed, indicating the effective central axis of the trachea. A 3D surface mesh of the trachea and its corresponding medial axis are shown in Figure 2.1d. The surface mesh can be used to define physical boundaries for the computational analysis as described in Chapter 5, and the medial axis can be used to identify geometric features as described in Chapter 3, in addition to postprocessing of analysis as described in Chapter 5. It should be noted that there is some ambiguity in the creation of the airway lumen model, as the threshold value for Hounsfield units indicating air volume is not uniquely defined. Note also that a medial axis itself is generally non-unique, as some variation may exist due to differences in its method of construction [33].

In order to quantify the sensitivity of aerodynamic performance to anatomical variations in the stenosis region, an artificial stenosis is created in the 3D modeling software Autodesk 3ds Max 2017. A stenosis is simulated by specifying a cylindrical region of the model to shrink. The parameters of the "shrinkage" tool may be varied in order to change the shape of the stenosis. Three variations of artificial stenosis are illustrated adjacent to the normal model in Figure 2.2. The artificial stenosis is used in lieu of models created from stenosis patients because it is currently uncommon for a physician to order CT or MRI

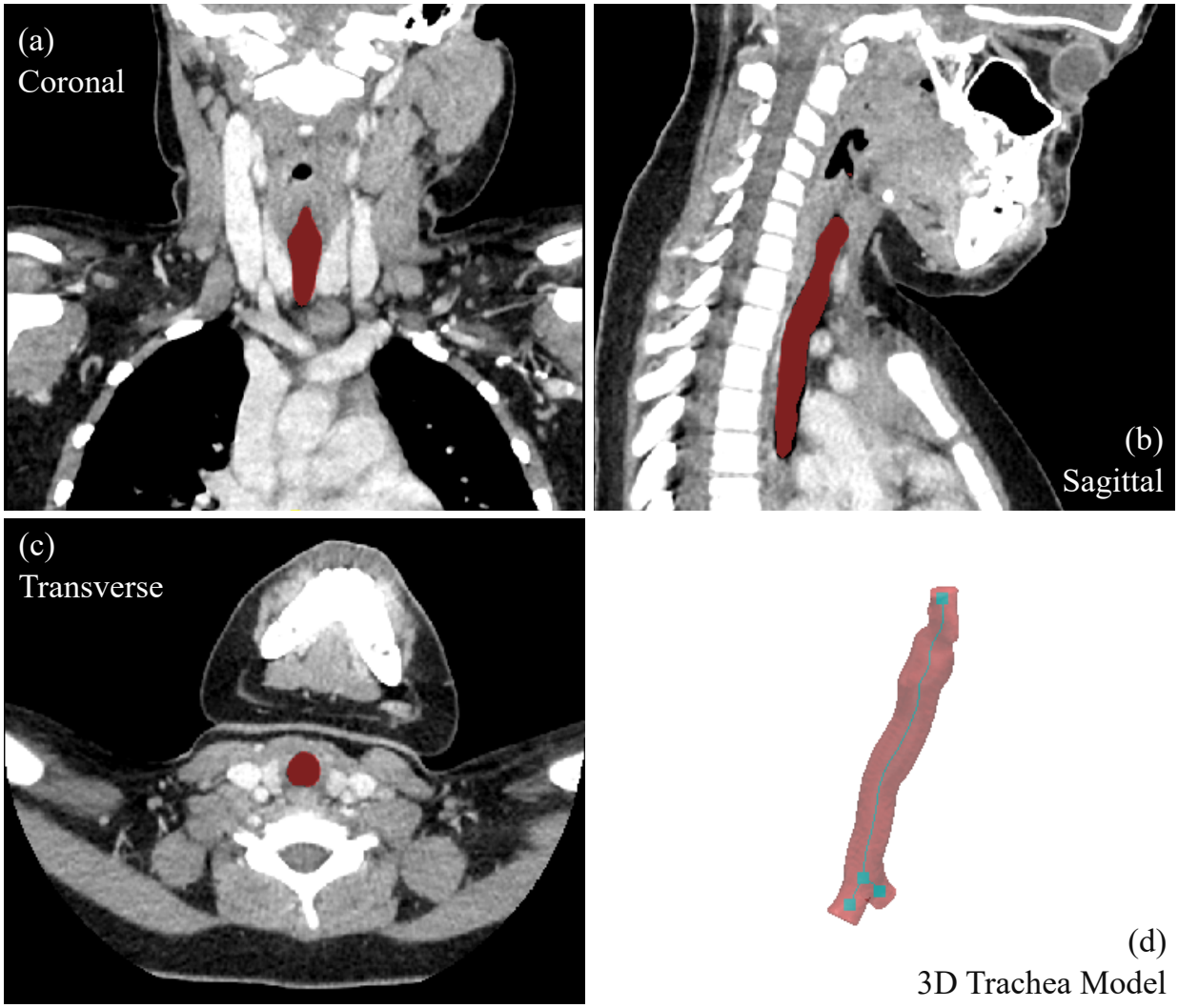

Figure 2.1. CT image projected onto (a) coronal, (b) sagittal, and (c) transverse planes with trachea identified in red; and (d) three-dimensional model reconstructed from scan with the medial axis identified.

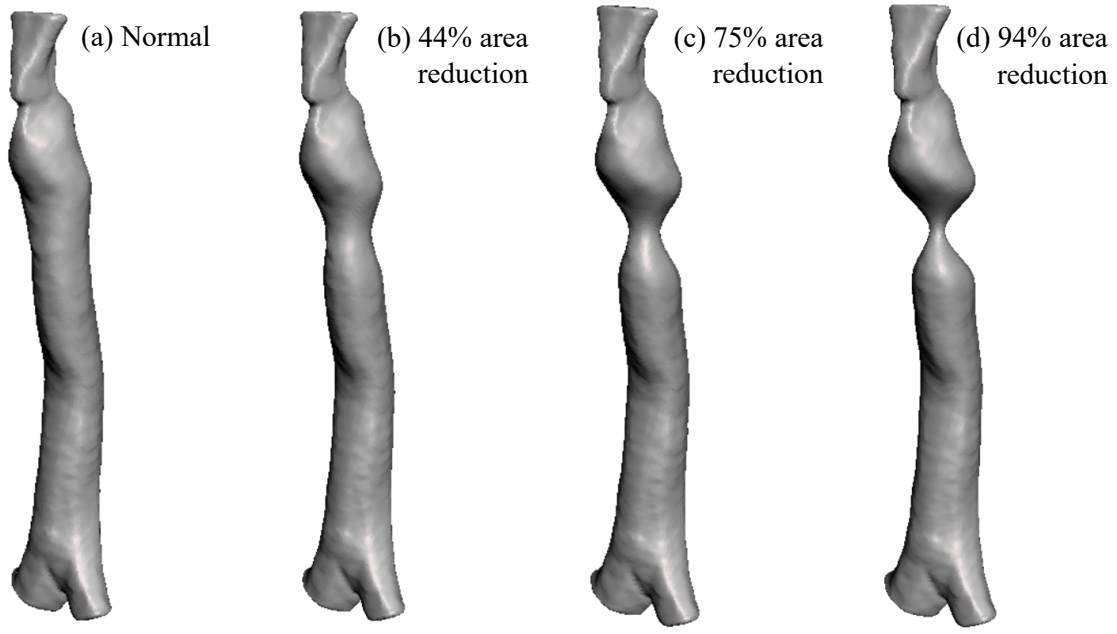

Figure 2.2. Comparison of (a) normal model to artificially-generated stenosis with (b) 44% area reduction, (c) 75% area reduction, and (d) 94% area reduction.

scans of patients with stenotic airways, and because it is more straightforward to quantify sensitivities between models which are identical except for the stenosis variations. Scans of real stenotic airways, though rare, may be compared to the results of simulated stenosis as a supplemental study.

Chapter 3
Anatomical Characterization of Stenosis

The current method of assessing stenosis in the airway is visual classification from an endoscopic image using the Myer-Cotton grading system [26]. As discussed in Chapter 1, the Myer-Cotton system is deficient in that it is overly subjective and tends to overlook the three-dimensional aspects of the trachea anatomy. A wavelet-based approach is proposed in order to automate and remove subjectivity from the measurement of anatomical features, while also accommodating three-dimensional effects.

Wavelet transforms are rapidly being adopted in many fields due to their ability to reveal the frequency content of non-stationary signals, while the familiar Fourier transform performs poorly for these cases. In the medical field, wavelets have been useful in early detection of coronary artery disease from heart-sound waveforms, detecting irregular heart beats, compressing medical images, reducing background noise in hearing aids, and in the early detection of breast cancer [3]. A reader unfamiliar with wavelets is referred to an introductory text on wavelet applications [1, 8].

3.1. Characteristic Dimensions

It is a natural result of dimensional analysis that physical processes may be characterized through dimensionless ratios of domain measurements rather than the measurements themselves. Since the inner surface of the trachea contains many undulations and effective length scales, it is impractical to consider a complete set of length scales. Rather, the leading-order characteristic dimensions are identified as the glottis-to-carina length L_{gc}, the glottis-to-stenosis length L_{gs}, the stenosis width w_s, the glottis hydraulic diameter D_g, the stenosis hydraulic diameter D_s, and the nominal hydraulic diameter D_0, as illustrated in Figure 3.1. Note that the definition of stenosis width w_s is somewhat ambiguous, as the measurement locations are themselves ambiguous. Also, the illustration of nominal diameter D_0 is approximate, as the nominal diameter is mathematically defined to be the statistical median hydraulic diameter between the glottis and carina. Thus, in order to

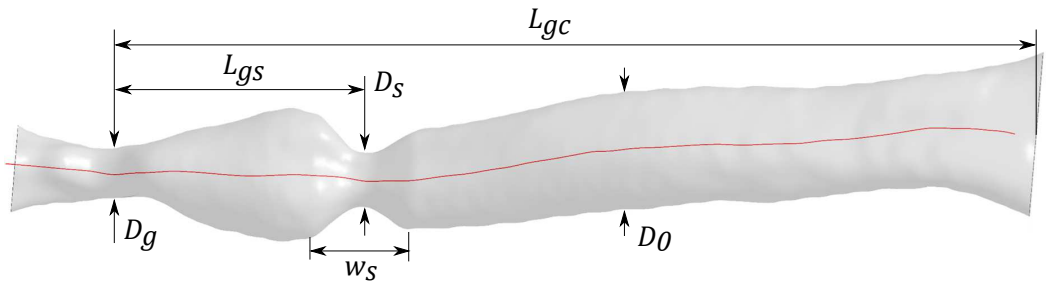

Figure 3.1. Stenotic trachea model with its medial axis (red) from just upstream of glottis (left) to carina (right).

characterize the physics, these six dimensions may be combined into five dimensionless ratios:

$$\frac{L_{gc}}{D_0}, \qquad \frac{L_{gs}}{D_0}, \qquad \frac{w_s}{D_0}, \qquad \frac{D_g}{D_0}, \qquad \frac{D_s}{D_0} \tag{3.1}$$

The diameter ratios may be written instead as approximate area reductions ς relative to the nominal area as

$$\varsigma_g = 1 - \left(\frac{D_g}{D_0}\right)^2, \qquad \varsigma_s = 1 - \left(\frac{D_s}{D_0}\right)^2 \tag{3.2}$$

3.2. Medial Axis Projection

Since the three-dimensional data describing the boundaries of the trachea lumen are highly complex, the three-dimensional data are reduced in dimension. The natural projection of this data is along the medial axis. By placing cross-sections along the medial axis and computing areas and perimeters of these cross-sections, it is possible to then analyze their variations using signal processing techniques. Figure 3.2 shows the medial axis projection of hydraulic radius (half the hydraulic diameter) over the length of the medial axis. In order to generalize this analysis, the hydraulic diameter and distance along the medial axis are scaled by the median hydraulic diameter D_0. Since it was shown in Chapter 1 that the trachea aspect ratio (L/D_0) remains relatively constant throughout aging, this scaling should apply well to many different age groups. Note that this transformation effectively "straightens" the trachea model, losing some three-dimensional information. This analysis may be extended to include more three-dimensional data by including other medial axis

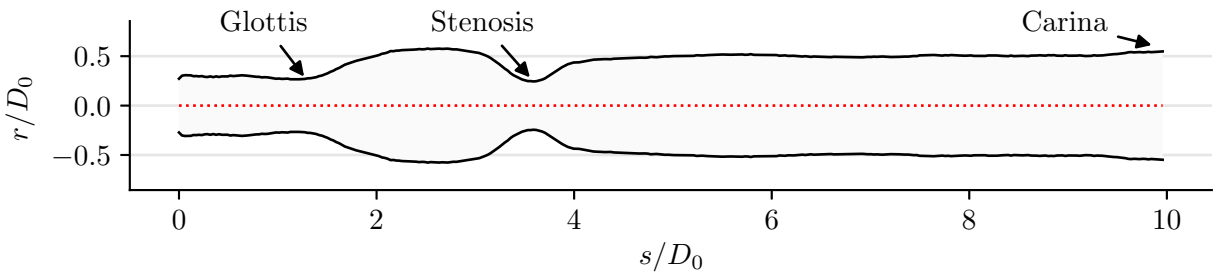

Figure 3.2. Scaled hydraulic radius versus scaled distance along the medial axis for the stenotic model.

data such as the local curvature or eccentricity (in the sense of describing conic sections), as outlined in Section 3.7.

3.3. Feature Location Identification

It is desired to identify the locations, diameters, and width (i.e. wavelength) of the glottis feature as well as a stenosis region; however, it is not as simple as taking the global minimum diameter, since the glottis may represent a smaller diameter than the stenosis in some cases. Various local minima may also be present due to natural undulations in the trachea surface. A relatively simple algorithm was designed to robustly identify the locations of the glottis and stenosis from a medial axis waveform of diameter $D(s)$, as described below:

(1) Eliminate edge artifacts by removing data spanning $\Delta s/D = 1/2$ from both sides. These artifacts originate from the method used to calculate the hydraulic diameter along the centerline. In particular, the cross-sectional planes used to calculate area and perimeter close to the inlet and outlet boundaries tend to intersect those boundaries, giving incorrectly low areas and perimeters.

(2) Find the location of maximum diameter s_m, which is assumed to correspond to the post-glottic expansion.

(3) Bisect the domain into pre-maximum ($s \leq s_m$) and post-maximum ($s \geq s_m$). The glottis should be in the pre-maximum region, while any stenosis should be in the post-maximum region.

(4) Define the glottis location s_g as the minimum-diameter location in the pre-maximum region, and define the leading-order stenosis location s_s as the minimum-diameter location in the post-maximum region.

Additional stenosis features may be identified by successive bisection at stenosis locations and identification of intermediate minima (i.e. not located at boundaries) within these sub-regions, but this is outside the scope of the present study.

3.4. Feature Length Scale Identification

It is also desirable to measure the length scale of an identified stenosis feature; however, there exist no unique datum points for measuring the width of the stenosis. A two-point measurement based purely on physical dimensions would thus be subjective, either clinically or virtually. In order to repeatably and objectively quantify the feature length scale, a wavelet-based method is proposed. The standard continuous wavelet transform of the signal $f(s)$ produces wavelet coefficients $\hat{T}(s,a)$ via a convolution operation as

$$\hat{T}(s,a) = \frac{1}{\sqrt{a}} \int_{-\infty}^{+\infty} f(\eta)\psi\left(\frac{\eta - s}{a}\right) d\eta \tag{3.3}$$

where ψ is the wavelet basis function, a is the scale of the feature, and s is the location of the feature. The prefactor $a^{-1/2}$ is applied to produce wavelet coefficients proportional to the energy content of the signal at that scale a and location s. While this property may be desirable for most time series analyses, it is undesirable for the present application. Each length scale should instead receive equal weighting because a reduction in diameter over a short length scale should be equally as important as a reduction diameter over a longer length scale. Hence, the modified wavelet transform $T^*(s,a)$ is defined in order to maintain a wavelet coefficient whose amplitude is independent of the scale s of the feature:

$$T^*(s,a) = \int_{-\infty}^{+\infty} f(\eta)\psi\left(\frac{\eta - s}{a}\right) d\eta \tag{3.4}$$

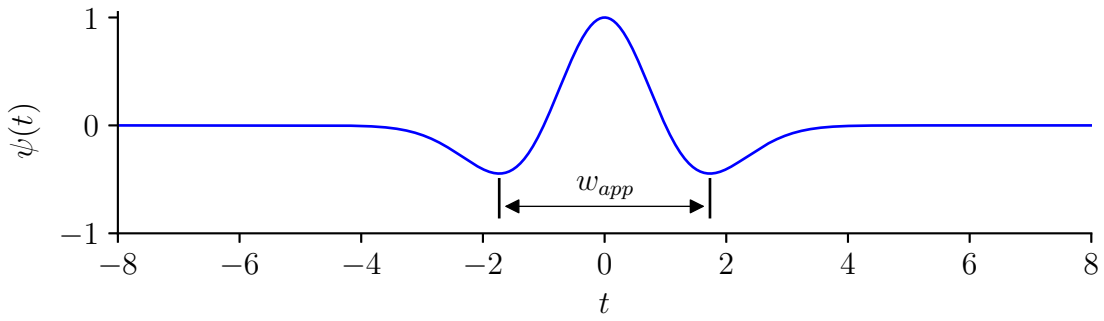

Figure 3.3. The base Ricker wavelet and its apparent width w_{app} identified from trough-to-trough distance.

The modified wavelet coefficient $T^*(s,a)$ at a given location s and scale a may be interpreted as the similarity between the wavelet ψ when it is scaled/stretched by the scale a and translated to the location s. Thus, the choice of wavelet basis function should be qualitatively similar to the feature which is to be identified.

The wavelet basis function $\psi(t)$ was chosen to be the widely-used Ricker wavelet, defined mathematically as

$$\psi(t) = \left(1 - t^2\right) \exp\left(-t^2/2\right) \tag{3.5}$$

The Ricker wavelet is a natural choice for identifying a stenosis because it contains a well-defined peak at its center – which will be useful in identifying the stenosis constrictions – and because it has a well-defined apparent feature width. The apparent width w_{app} of the wavelet is the trough-to-trough distance as shown in Figure 3.3, which can be expressed analytically in terms of scale a as

$$w_{app} = 2\sqrt{3}a \tag{3.6}$$

A local maximum value of the modified wavelet transform $T^*(s,a)$ at $a = a^*$ and $s = s^*$ will indicate a peak of $f(s)$ located at $s = s^*$ with an apparent length scale of $w = 2\sqrt{3}a^*$. Conversely, a local minimum value will indicate a trough of $f(s)$ located at $s = s^*$ with an apparent length scale of $w = 2\sqrt{3}a^*$.

Consider the stenotic tube model with $\varsigma = 0.5$ and $w/D_0 = 1$ as illustrated in Figure

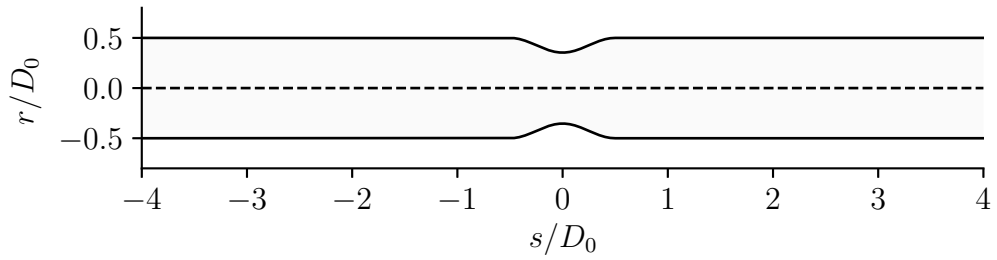

Figure 3.4. Stenotic tube model with $\varsigma = 0.5$ and $w/D = 1$.

3.4, where the diameter $D(s)/D_0$ was defined in Chapter 1. The modified wavelet transform T^* of scaled diameter $D(s)/D_0$ of the stenotic tube model is shown in Figure 3.5a. Note that the edge effects appear as positive values, while the trough region appears as negative values. It is expected also that if local peaks existed in the signal of D/D_0, these would also appear as positive values of T^*. Note also that the minimum value of T^*, identified by a red dot, occurs at $s/D_0 = 0$ and $w/D_0 = 1$. This agrees well with the parameters usd to construct the model. Since stenosis regions appear only as negative values of the modified wavelet coefficient T^*, a trough indication coefficient $T_t(s, a)$ is defined in order to give a more direct indication of constriction regions:

$$T_t(s, a) = -\min\left(0, T^*(s, a)\right) \tag{3.7}$$

The trough indication coefficient T_t of the stenotic tube model is shown in Figure 3.5b. Note here that the edge effects have been filtered out, and again that the maximum value of T_t occurs at $s/D_0 = 0$ and $w/D_0 = 1$. Thus, it is proposed that the feature width w^*/D_0 of a location s/D_0 is given by the maximum trough indicator coefficient at that location:

$$w^*/D_0 = \max_{T_t}\left(w/D_0\right) \tag{3.8}$$

3.5. Verification

The axisymmetric stenotic tube model was used in order to verify that the proposed wavelet method provides consistent prediction of the stenosis width w/D_0 and location

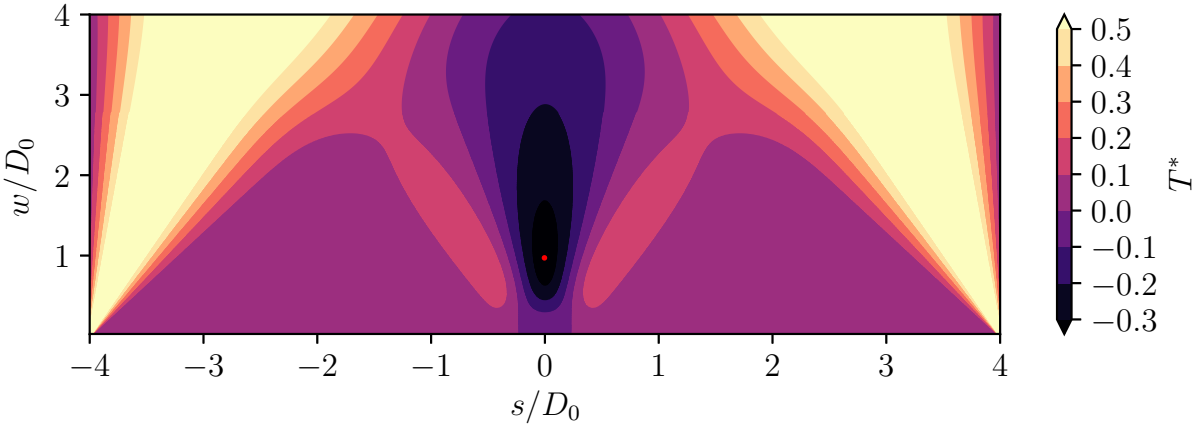

(a)

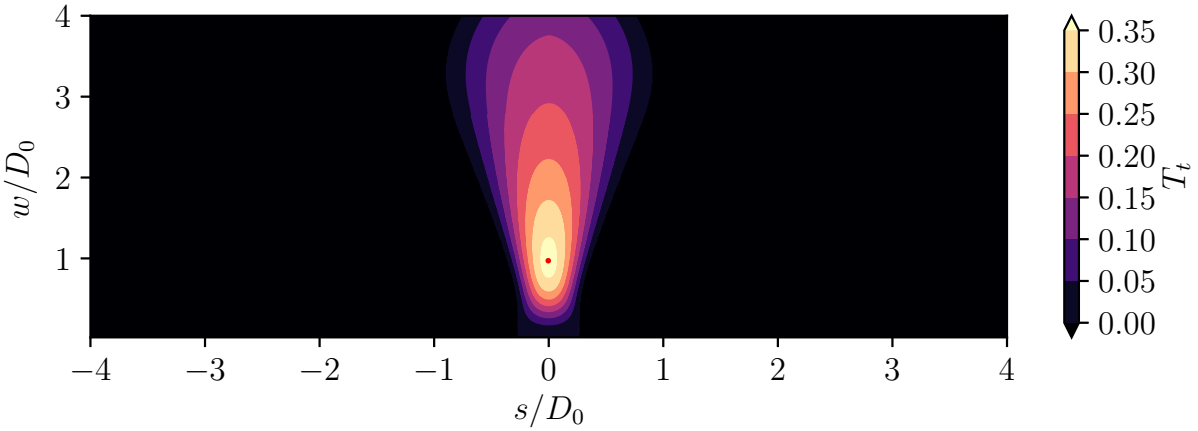

(b)

Figure 3.5. (a) Modified wavelet coefficients T^* and (b) trough indication coefficient T_t at all variations of feature width w/D_0 and feature location z/D_0, for stenotic tube model with $\varsigma = 0.5$ and $w/D = 1$.

Table 3.1. Verification of wavelet-based feature length scale identification algorithm using axisymmetric stenotic tube model.

ς	Specified w/D_0	Measured w/D_0	w/D_0 Error	$\max(T_t)$
0.25	0.10	0.098	−2.0%	0.167
	0.25	0.243	−2.8%	0.167
	0.50	0.488	−2.4%	0.167
	0.75	0.730	−2.6%	0.167
	1.00	0.975	−2.5%	0.167
0.50	0.10	0.098	−2.0%	0.365
	0.25	0.243	−2.8%	0.365
	0.50	0.488	−2.4%	0.365
	0.75	0.730	−2.6%	0.365
	1.00	0.975	−2.5%	0.365
0.75	0.10	0.098	−2.0%	0.624
	0.25	0.243	−2.8%	0.624
	0.50	0.488	−2.4%	0.624
	0.75	0.730	−2.6%	0.624
	1.00	0.975	−2.5%	0.624
0.90	0.10	0.098	−2.0%	0.853
	0.25	0.243	−2.8%	0.853
	0.50	0.488	−2.4%	0.853
	0.75	0.730	−2.6%	0.853
	1.00	0.975	−2.5%	0.853

s/D_0. With this model, the parameters used to create the model are compared against the parameters produced by the wavelet method. Firstly, the width measured by the maximum trough indication coefficient was verified against the input width, as shown in Table 3.1. Four variations of area reduction ς are used, each with five variations of w/D_0. It is evident from this result that the predicted stenosis width w/D_0 is consistently within 3% of the specified stenosis width, with typically low predictions. It is also evident that the amplitude of the trough indication coefficient corresponding to the stenosis is indeed invariant to feature width w/D_0, as constructed. The maximum value of trough indicator coefficient T_t for stenotic tube models with $0 < \varsigma < 1$ and $0.4 \leq w/D_0 \leq 2$ is plotted in Figure 3.6. A power-law fit to the area reduction ς and the relative width w/D_0 gives the

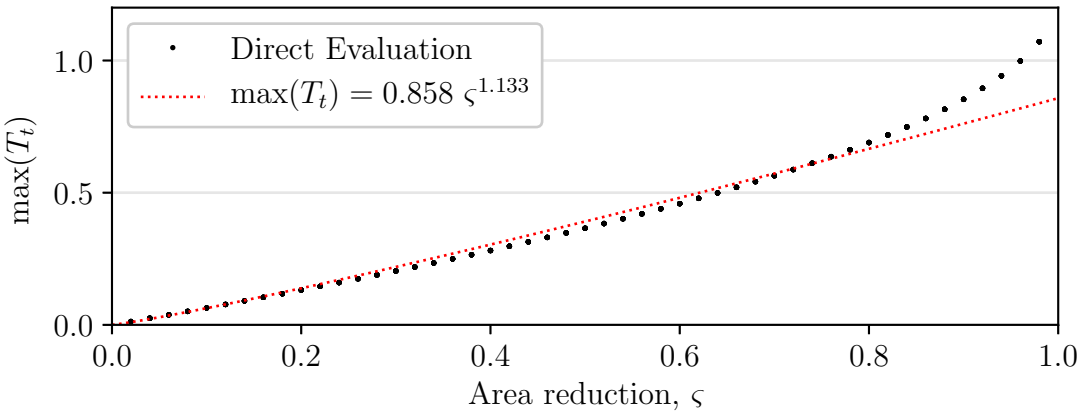

Figure 3.6. Maximum value of trough indicator coefficient T_t for stenotic tube models with $0 < \varsigma < 1$ and $0.4 \leq w/D_0 \leq 2$, with power-law fit indicating a negligible sensitivity to w/D_0.

equation:

$$\max(T_t) = 0.858\ \varsigma^{1.133}(w/D_0)^{1.6\times10^{-4}} \tag{3.9}$$

Thus, the peak amplitude of trough indicator coefficient T_t is approximately linearly proportional to ς and is independent of the stenosis width w/D_0.

3.6. Feature Identification of Stenosis in Real Airways

The feature location and length-scale algorithms are combined to identify and measure the glottis and stenosis for an airway with stenosis. The airway model was created with a stenosis as-described in Chapter 2. The results of the full algorithm applied to a stenotic trachea are shown in Figure 3.7. In the top panel, the scaled hydraulic diameter D/D_0 is plotted against scaled distance along medial axis s/D_0. The corresponding trough indicator coefficient T_t for each location s/D_0 and feature width w/D_0 is plotted in the bottom panel. Note the two peaks of T_t corresponding to the glottis and stenosis, which correspond to their local widths and locations. A "width bar" is shown at the stenosis location indicating its measured width w/D_0.

The same algorithm is applied to several simulated stenosis models, as illustrated in Figure 3.8. Here, each stenosis was generated in the 3D model as described in Chapter

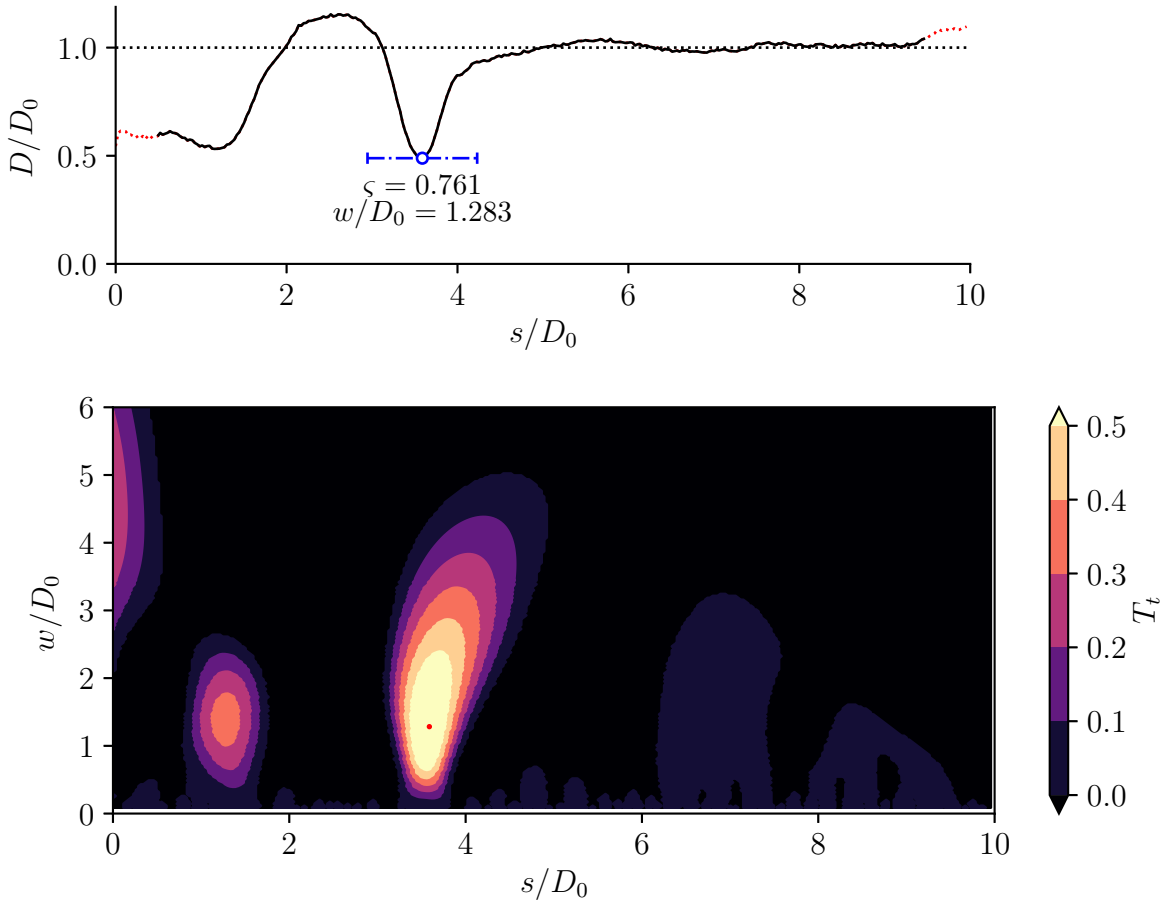

Figure 3.7. Scaled hydraulic diameter D/D_0 versus scaled distance along medial axis s/D_0 for a trachea model with stenosis (top panel), and the corresponding trough indicator coefficient T_t for each location s/D_0 and feature width w/D_0 (bottom panel). A "width bar" is shown at the stenosis location indicating its measured width w/D_0.

2, with one of four variations of area reduction and one of four variations of stenosis width. Note that in the base case, a minor "stenosis" is detected with an area reduction of $\varsigma = 0.164$ and a width of $w/D_0 = 2.38$, due to naturally-occurring undulations in the airway. Thus, only area reductions above some nonzero threshold should be considered to be stenotic. Note also that on each plot, a "width bar" is shown at the stenosis location indicating its measured width w/D_0. From this result, the algorithms generally give results with qualitatively consistent with intuition. One outlying case is the case of lowest area reduction ς and smallest feature size $w/D_0 = 1.48$ as in Figure 3.8d. In this case, it seems that the feature width is determined by the natural shape of the airway, rather than that of the stenosis. This is because the "strength" of the stenosis in the signal is overpowered by the signal related to natural diameter variations in the airway. Fortunately, this misdetection only occurs for the extremely sharp, low-area-reduction cases. It is also evident from these plots that the median hydraulic diameter appears to be unaffected by the virtual stenosis, since the stenosis affects only a small region of the trachea.

3.7. Discussion

The medial-axis-based feature-detection algorithms presented in this chapter have been shown to provide robust parameterization of the location, area reduction, and feature width of both the glottic and stenotic constrictions. Thus, quantifiable anatomical parameters have been presented, which can be correlated directly to aerodynamic (or otherwise physiological) performance. This type of characterization can be extended to any sort of structure for which a medial axis may be identified.

It is possible in some cases for a patient to have multiple stenosis regions. The methodology presented here extends naturally to regions of multiple stenosis. The feature location algorithm of Section 3.3 may be augmented with sequential bisection steps. Once the glottis region has been separated from the stenosis region, the primary stenosis is detected by the minimum diameter. Then, the original stenosis region may be bisected by the primary stenosis. In each subregion, a local minimum (not at the boundary) may be sought.

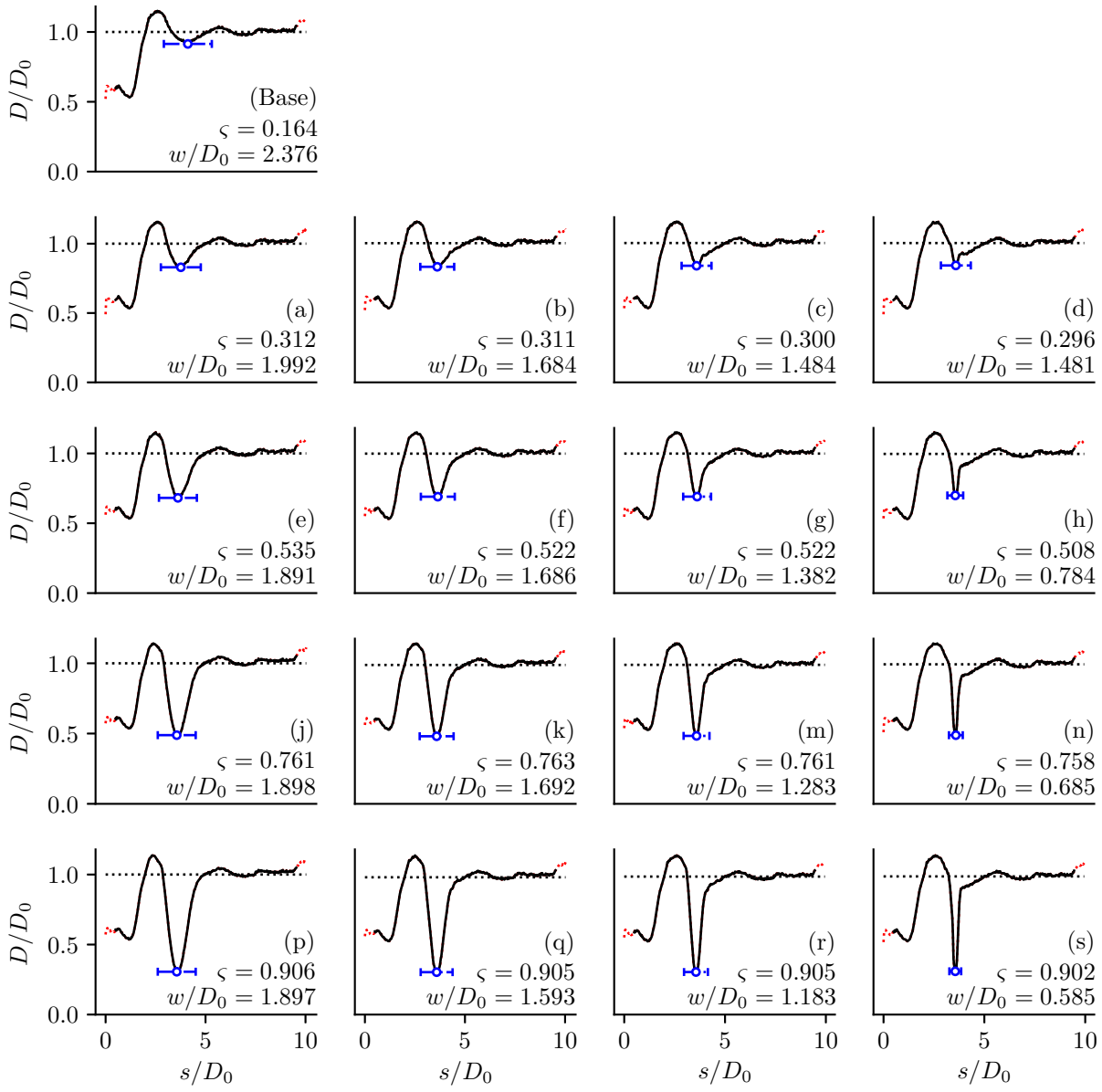

Figure 3.8. Identified glottis and stenosis features for baseline model and simulated stenosis models with varying area reductions and stenosis width, indicating measured stenosis area reduction ς and stenosis width w/D_0 indicated on each plot. On each plot, a "width bar" is shown at the stenosis location indicating its measured width w/D_0.

For each new local minimum discovered, the domain is bisected. The process continues recursively until no further stenosis features are detected beyond some threshold of area reduction ς. With the location of each stenosis identified, the width may be determined directly from the trough indicator coefficient T_t, with an identical feature length scale identification algorithm to that shown in Section 3.4.

Although the present work only offers a method for characterizing the location, area reduction, and width of stenosis features, the medial-axis projection may be used to characterize additional three-dimensional effects – for example, the medial axis curvature. Since the medial axis is an ordered set of coordinates ($\vec{X}(s) = \vec{f}(s)$), the three-dimensional tangent vector $\vec{T}(s)$, curvature vector $\vec{C}(s)$, and radius of curvature $R(s)$ may be found as

$$\vec{T}(s) = \frac{d\vec{f}(s)}{ds}, \qquad \vec{C}(s) = \frac{d\vec{T}(s)}{ds}, \qquad R(s) = ||\vec{C}(s)||^{-1} \tag{3.10}$$

Wavelet methods can then be used to compute more information on the curvature, such as the length of trachea affected by different amounts of curvature.

One potential improvement of the wavelet method is to mitigate edge effects by modifying the near-boundary behavior of the wavelet transform. This can be done by adding constant-valued "ghost-length" to the left and right boundaries of the data. By using the wavelet transform on the extended domain, the edge effects might be pushed to the extension, which can then be removed after computing the wavelet transform. It should be noted that while this approach may mitigate the edge effects, it does so by introducing new edge effects which are a function of the "ghost-length" values. The "ghost-length" approach was not used in the present work because it did not produce appreciable improvements in results; however, it may be more valuable in other applications.

Chapter 4
Computational Fluid Dynamics of Stenotic Tube

Generally, experimental validation is required in order to select the most appropriate turbulence model for simulations. Since experimental studies were outside the scope of the present study, the ideal stenotic tube model studied experimentally by Young & Tsai [47] and Ahmed & Giddens [2] was used to validate the turbulence model. Since this stenotic tube model represents a simple, standard model for analysis, it was also used to study the sensitivity of simulation results to variations in the computational grid resolution. A schematic of the ideal stenotic tube model is shown in Figure 1.5.

4.1. Turbulence Model Validation

In order to determine the best two-equation RANS turbulence model for stenosis-type flows, three turbulence models were used – the k-ε Realizable model, the k-ω SST model, and the k-ω SST model with a low-Reynolds number correction (k-ω SST LRC). Two variations on the inlet turbulence intensity – 0.1% and 5% turbulence intensity – were used for each model. The other turbulence boundary condition was set implicitly in Fluent by a correlation with the pipe diameter [5]. For each geometry, a two-dimensional axisymmetric structured quadrilateral mesh was created using ANSYS Meshing, as illustrated in Figure 4.1. Note that although the final analysis will be three-dimensional, a two-dimensional analysis was used to validate the turbulence model since the domain is axisymmetric and the averaged flow field is also expected to be axisymmetric for this case. A maximum cell size of $\Delta x/D_0 = 0.0125$ was used, with additional refinement close to the walls, as shown in Figure 4.1c. The mesh contains approximately 150,000 cells with 110 cells across the diameter. The near-wall inflation layer region was designed to have a first-cell y^+ value of approximately 1, in accordance with the k-ω and k-ε turbulence models [4], with a smooth transition to the freestream mesh.

Firstly, the center-velocity and shear stress profiles at Re = 2000 for area reductions of $\varsigma = 0.25,\ 0.50,$ and 0.75 are compared with the experimental measurements of Ahmed

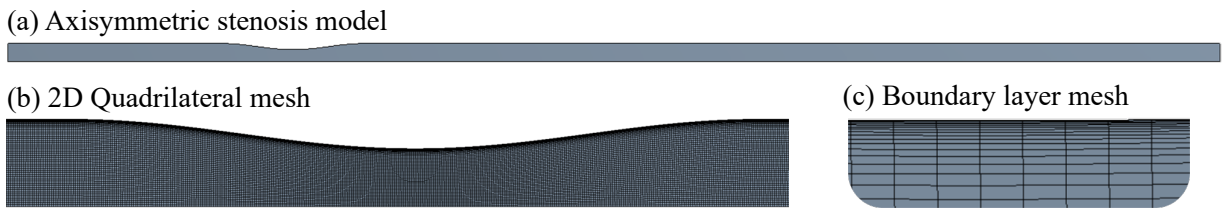

Figure 4.1. CFD model of stenotic tube for turbulence model validation, showing (a) axisymmetric model, (b) 2D quadrilateral mesh, and (c) near-wall boundary layer refinement.

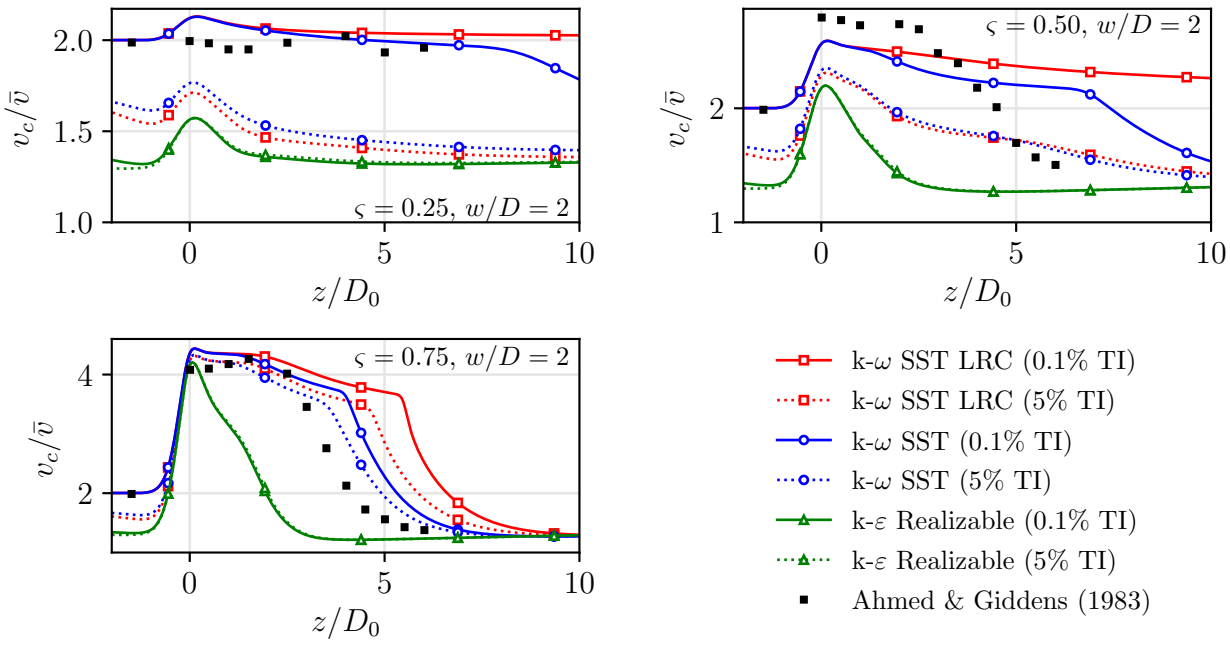

Figure 4.2. Centerline velocity scaled by average velocity ($v_c/\bar{v}$) at Re = 2000 computed with different turbulence models compared to experimental data of Ahmed & Giddens [2].

and Giddens [2] in Figures 4.2 and 4.3, respectively. From these plots, it is evident that (1) low inlet turbulence intensities match well with the experiments, (2) the k-ε model predicts much shorter separation regions than the k-ω models, and (3) the k-ω SST model appears to give the most accurate profiles. Note that none of the models match perfectly.

The experimental measurements of pressure drop and separation/reattachment locations of Young & Tsai [47] provide another perspective – perhaps a better indicator of overall performance. Simulation results for area reductions of $\varsigma = 0.56$ and 0.89 over a wide range of Reynolds number are shown in Figures 4.4 and 4.5, respectively. The pressure drop is computed from locations of ± 8 diameters of the stenosis, and is compared to

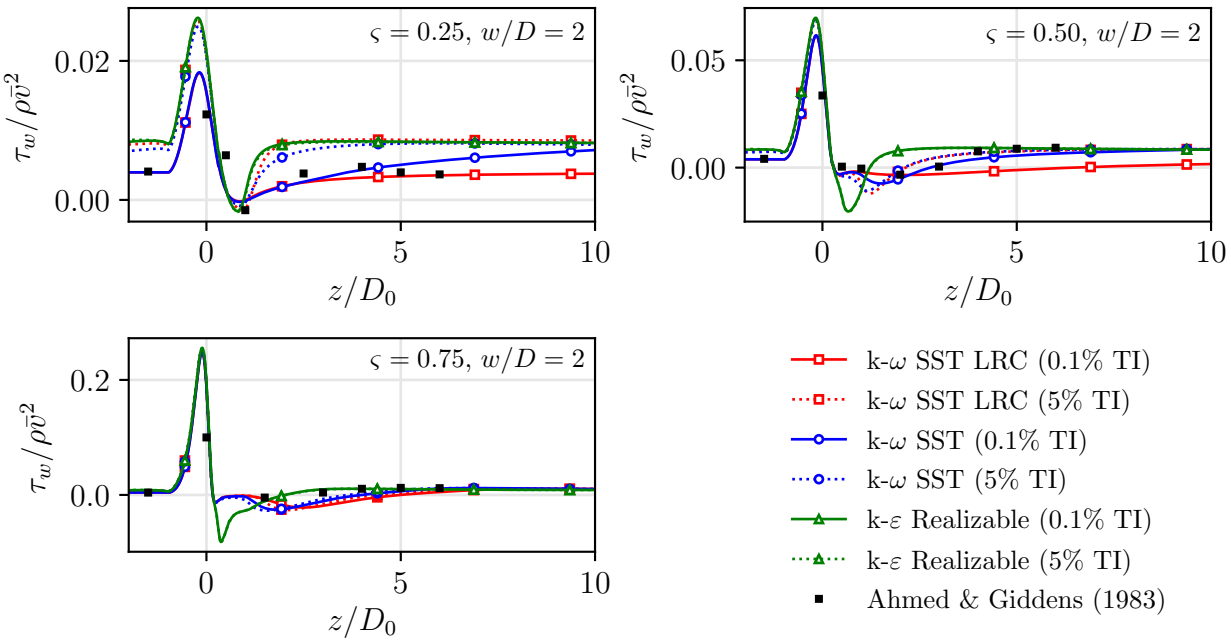

Figure 4.3. Scaled wall shear stress ($\tau_w/\rho\bar{v}^2$) at Re = 2000 computed with different turbulence models compared to experimental data of Ahmed & Giddens [2].

the theoretical results of Hagen-Poiseuille flow (laminar, fully-developed pipe flow), and the Sudden Expansion, whose losses are independent of Reynolds number. Once again, the k-ε consistently has the worst predictions, and underpredicts separation region size. The k-ω SST model seems to most accurately predict pressure drop, while the k-ω SST LRC model has some aberrant behavior at low Reynolds numbers. This can be attributed to the fact that the low-Reynolds number correction uses a nonlinear damping function to artificially reduce the eddy viscosity at low strain rates. Thus, the transition is much more abrupt. The k-ω SST LRC model also inaccurately predicts for $\varsigma = 0.56$ that the pressure drop approaches that of Hagen-Poiseuille flow at higher Reynolds numbers. The separation region data also seems to indicate reasonable performance of the k-ω SST model in predicting separation and reattachment locations. The k-ω SST model also tends to agree well with the Sudden Expansion prediction at higher Reynolds numbers, as does the experimental data.

Based on these validation cases, the k-ω SST model was chosen for the remainder of

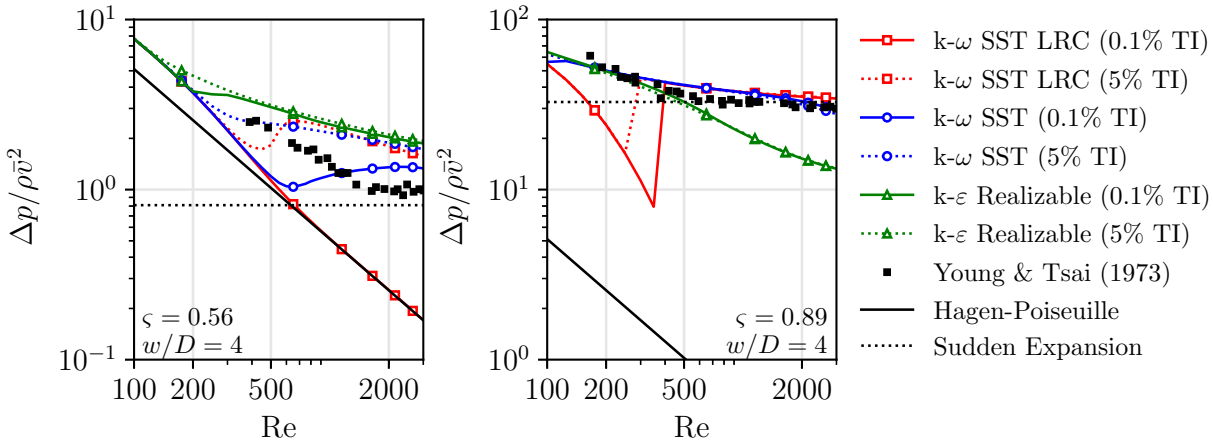

Figure 4.4. Scaled pressure drop ($\Delta p/\rho\bar{v}^2$) computed with different turbulence models compared to experimental data of Young & Tsai [47].

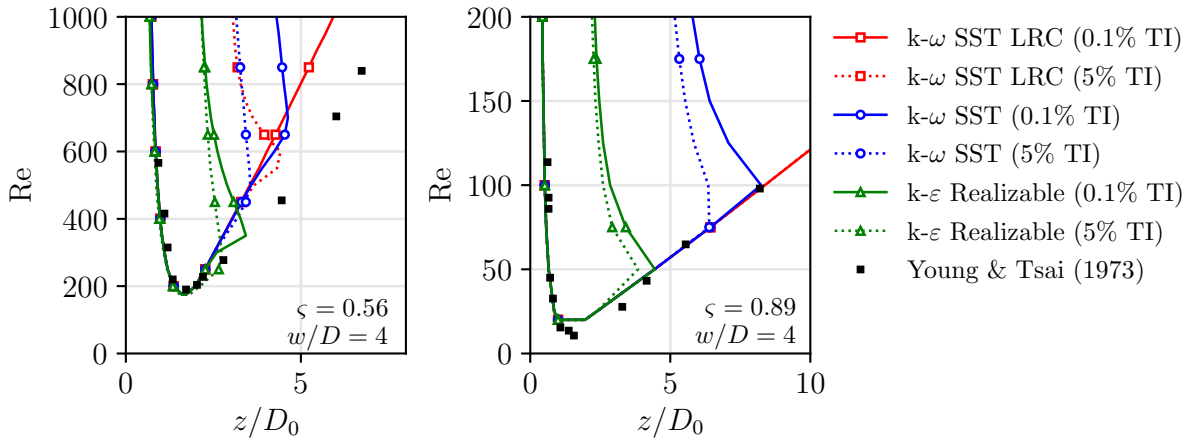

Figure 4.5. Scaled locations of flow separation and reattachment (z/D_0) computed with different turbulence models compared to experimental data of Young & Tsai [47].

the simulations described in this thesis. It should be noted that although there are some discrepancies in the velocity profiles, pressure drops, and shear stresses, the trends are faithful to experiments. Furthermore, exactly accurate predictions are not the expressed purpose of the present study; rather, the framework for aerodynamics predictions of tracheal stenosis is the most important goal.

4.2. Mesh Sensitivity

In order to assess the adequacy of the computational grid on a stenotic airway, the stenotic tube model was used with an area reduction of $\varsigma = 0.75$ and a stenosis width of $w/D_0 = 4$. In order to ensure that the boundary conditions do not affect the physics near the stenosis, the inlet boundary was placed 10 diameters upstream of the stenosis, and the outlet boundary was placed 25 diameters downstream of the stenosis. A three-dimensional unstructured tetrahedron volume mesh was generated in ANSYS ICEM CFD using the octree method, using prism inflation layers to resolve the near-wall velocity gradients. The near-wall inflation layer region was designed to have a first-cell y^+ value of approximately 1 in accordance with the k-ω turbulence model [4], with a smooth transition to the freestream mesh. This mesh generation process is identical to the process used for the simulations discussed in Chapter 5.

A nondimensional approach was used in order to characterize the mesh sensitivity. The global cell size δx of the mesh is scaled by the nominal diameter D_0 as the average number of cells across one diameter, $\Delta \equiv D_0/\delta x$. Five meshes were used to characterize the mesh sensitivity, as described in Table 4.1. The relative computational cost of each mesh are indicated to leading-order by the total number of cells in each mesh. Here, Mesh M5 with $\Delta = 29.0$ is assumed to be over-refined, nearly perfectly satisfying the mathematical models. Each mesh is illustrated in Figure 4.6. The necessary mesh size for a production simulation run is determined by comparing the results of Meshes M1-M4 to Mesh M5. In each case, a Reynolds number of 2000 was used with a parabolic inlet velocity profile.

Dimensionless flow quantities are again used to compare results. Here, all pressures are

Table 4.1. Mesh parameters used in mesh sensitivity study.

Mesh	Avg. Cells per Diameter, Δ	Total Cells
M1	6.80	512,000
M2	10.2	1,170,000
M3	15.2	3,130,000
M4	22.8	8,560,000
M5	29.0	15,400,000

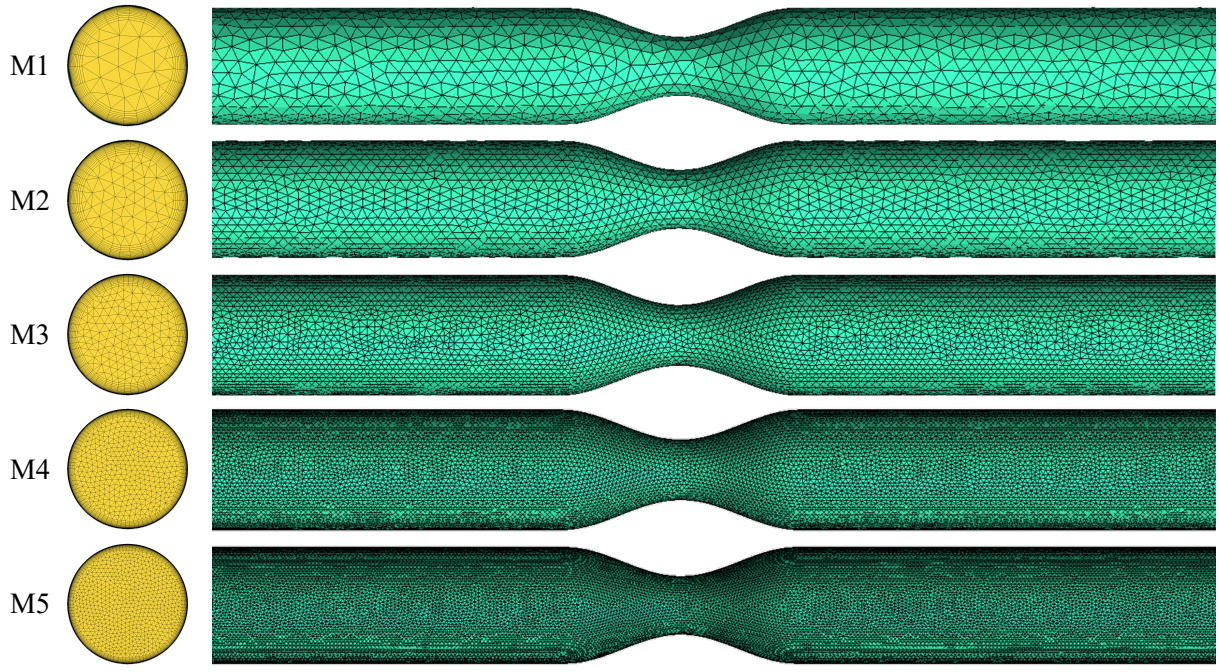

Figure 4.6. Surface meshes on inlet (left) and wall (right) boundaries of meshes M1-M5 used in mesh sensitivity study. Note that the wall surface mesh shown is a subset of full domain, which extends in both directions.

scaled by the dynamic pressure $p_d = \frac{1}{2}\rho\bar{v}^2$, where $\bar{v}$ is the average velocity at the tube inlet (nominal diameter). Cross-sections are placed at regular intervals along the tube, on which are computed a perimeter-averaged skin friction coefficient $\bar{C}_f$, a flow-averaged pressure coefficient $\bar{C}_p$, a flow-averaged total pressure coefficient $\bar{C}_{pt}$, a flow-averaged eddy viscosity ratio $\bar{\nu}_t/\nu$, a flow-averaged turbulence intensity $\bar{I}$, and a flow reversal ratio Q_r/Q. Note that the flow-averaging of a scalar ψ is defined as

$$\bar{\psi} = \frac{\iint_{CS} \psi(\vec{v}\cdot\vec{n})dA}{\iint_{CS}(\vec{v}\cdot\vec{n})dA} \tag{4.1}$$

and the flow reversal ratio on a given cross-section is defined to be an indicator of the relative size of the flow separation region, as

$$\frac{Q_r}{Q} = -\frac{\iint_{CS} \min\left[0, (\vec{v}\cdot\vec{n})\right] dA}{\iint_{CS}(\vec{v}\cdot\vec{n})dA} \tag{4.2}$$

where $\vec{v}$ is the velocity vector and $\vec{n}$ is the unit normal vector, pointing in the mean direction of flow. Flow averaging is used rather than area averaging because it provides a more meaningful indicator of total pressure drop. It can be shown through an application of the second law of thermodynamics that a flow-averaged total pressure must monotonically decrease along the direction of a decreasing pressure gradient, while there is no such property for area averaging. The profiles of the six quantities are plotted in Figure 4.7. As expected, the profiles converge to the most-refined case of M5. An RMS error may be computed in order to quantify the "residual error" of each case as compared to the most refined case. Let $\hat{f}(x)$ be an approximation of $f(x)$, then the RMS profile error e_{rms} is defined as

$$e_{rms} = \sqrt{\frac{1}{L}\int_0^L \left[f(z) - \hat{f}(z)\right]^2 dz} \tag{4.3}$$

The residual for these quantities is shown below in Figure 4.8 with a power-law fit to estimate the convergence rate. Note that the convergence rate of approximately 1.6 agrees

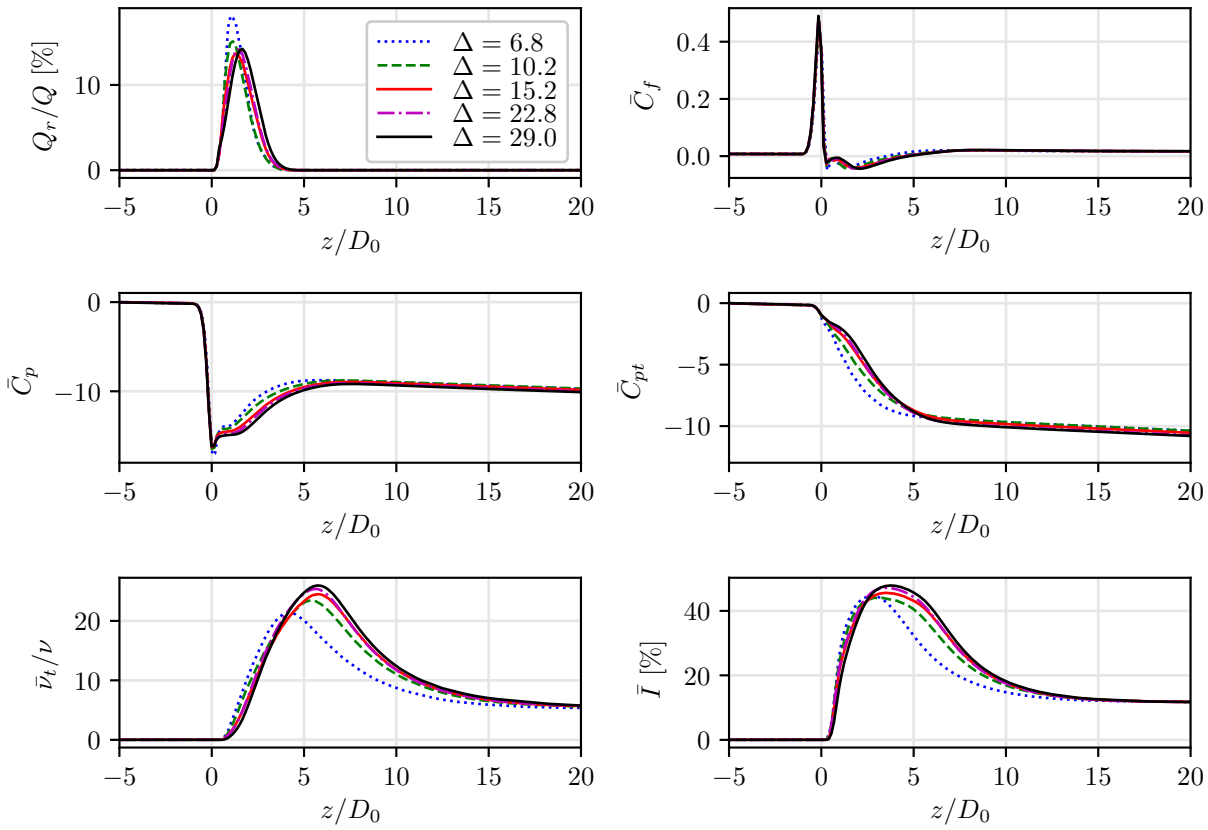

Figure 4.7. Integrated and averaged quantities for ideal stenotic tube along the dimensionless axial distance z/D_0, computed on increasingly fine grids at $\mathrm{Re_D} = 2000$.

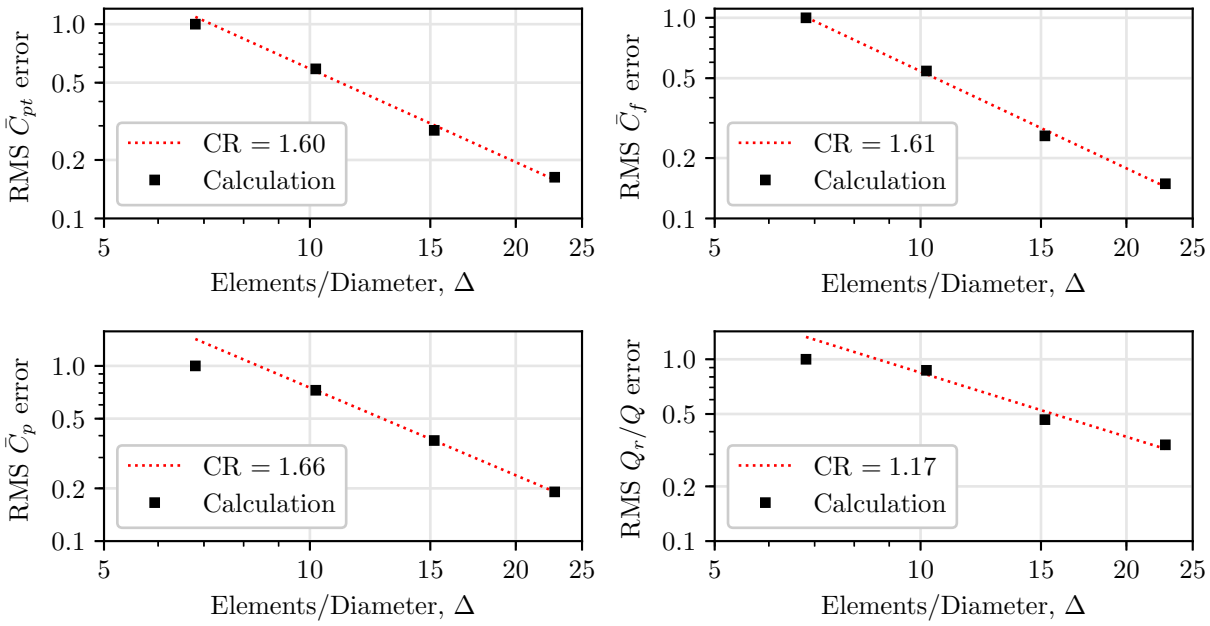

Figure 4.8. RMS profile errors for ideal stenotic tube, computed on increasingly fine grids at $\mathrm{Re_D} = 2000$. RMS errors are computed relative to the $\Delta = 6.8$ mesh.

well with the fact that a second-order spatial discretization scheme is used. A reduction from the ideal convergence rate of 2 is expected due to the use of a non-uniform and non-orthogonal mesh [11], as well as the standard use of flux limiters in the spatial discretization used by ANSYS Fluent [4]. In order to develop a rule of thumb for an appropriately-sized mesh, the mesh-sensitivity of discrete measurements must be examined. Let $\hat{f}$ be an approximation of the exact value f of the measurement, then the discrete measurement error e_m is defined as

$$e_m = |f - \hat{f}| \tag{4.4}$$

In order to assess the overall convergence of scalar flow parameters, the maximum skin friction coefficient, maximum pressure coefficient, maximum flow reversal, and loss coefficient ($\Delta\bar{C}_{pt}$ from $z/D_0 = -5$ to 25) are computed, as shown in Figure 4.9. Note that the loss coefficient has a comparable convergence rate to the residuals, while the extrema have much higher sensitivity to the mesh. This is due to the fact that extrema are highly sensitive to variations in parameters, while the residuals and loss coefficient represent "averaged"

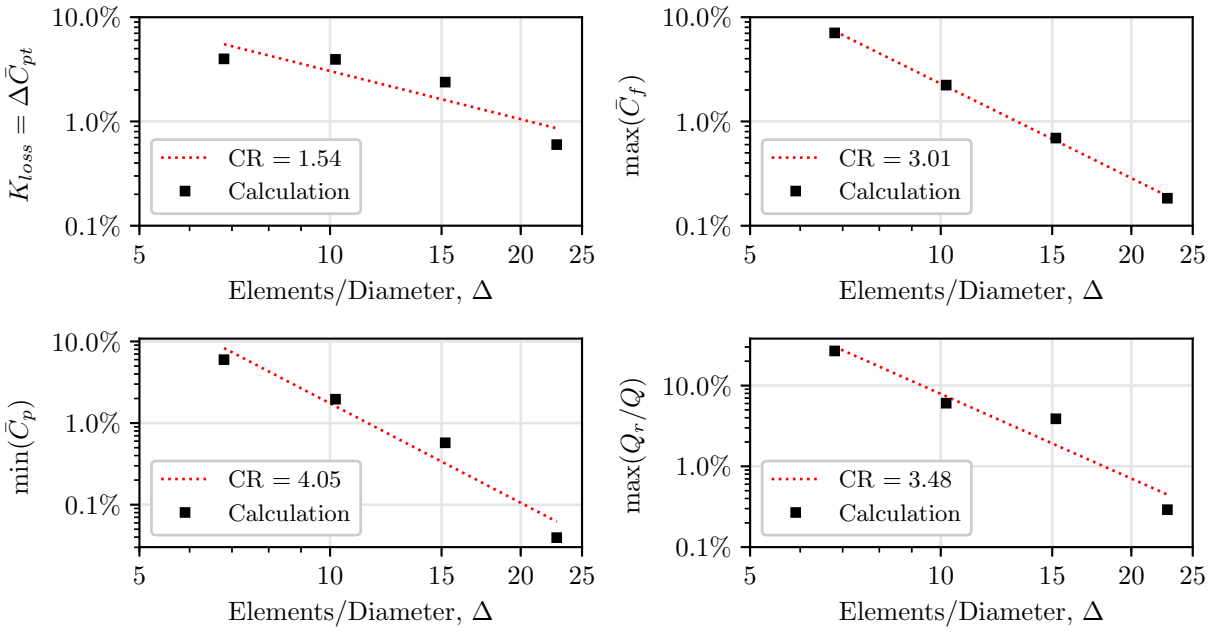

Figure 4.9. Discrete measurement errors for ideal stenotic tube, computed on increasingly fine grids at $\mathrm{Re_D} = 2000$.

sensitivities.

4.3. Discussion

The ideal stenotic tube model has provided a useful basis for validating the turbulence model to be used in the simulations on the real airways, as well as a useful "clean" model for evaluating the mesh sensitivity. It seems from these analyses that the k-ω turbulence model gives gives the most accurate results, as compared to the data of Ahmed & Giddens and Young & Tsai. The mesh sensitivity study indicates that using $\Delta \geq 18$ will give results within 1% of the highly-refined case (M5, with $\Delta = 29$). It should be noted that this mesh sensitivity was performed for $\mathrm{Re} = 2000$ (for the incoming flow) and $\varsigma = 0.75$. Higher Reynolds numbers and area restrictions will likely produce higher shear rates, hence higher velocity gradients. Thus, it is recommended to use conservatism – that is, larger Δ – in designing grids for flows with higher Reynolds numbers and area restrictions.

Chapter 5
Computational Fluid Dynamics of Real Airways

In this chapter, the aerodynamics of stenotic trachea are analyzed using real CT scans of pediatric airways. Efforts are made to simplify the analysis to a form which gives physiologically meaningful results with minimal model complexity. The primary goals of this chapter are as follows:

(i) Develop a methodology for computational analysis of air flows in stenotic trachea,

(ii) Propose aerodynamic metrics indicative of breathing performance and quantify from numerical simulations,

(iii) Correlate the geometric and aerodynamic performance parameters,

(iv) Identify and characterize the prominent flow structures of tracheal stenosis.

Here, a primary focus is placed on the inspiratory part of the respiratory cycle, since symptomatic breathing difficulties are limited by inspiration rather than expiration. Simulations are performed up to Reynolds numbers of 2500 to adequately capture the physically relevant range, as determined from the statistics in Chapter 1.

5.1. Model Complexity

As discussed in Chapter 2, the model equations for the trachea airflow are the Reynolds-Averaged Navier-Stokes (RANS) equations. In Chapter 4, it was shown that a k-ω SST model provides the most accurate results for flows in stenotic geometries at the relevant Reynolds numbers. While it is possible to use Large Eddy Simulations (LES) or even Direct Numerical Simulations (DNS), such approaches tend to be too time-consuming and costly for the quantity and scale of simulations in the present work, and are left to future studies.

In order to simplify the analysis to a reasonable scope for leading-order-accurate results, the following assumptions are made:

(i) The trachea walls are perfectly rigid.

(ii) Effect of mucociliary transport at the trachea walls on the airflow is negligible.

(iii) Although inspiratory flow is inherently transient, the instantaneous flow is well-

represented by a stationary flow – that is, with time-invariant boundary conditions. Each of these assumptions represents an opportunity for future studies. Section 5.6 further explores the stationary-flow assumption. The purpose of the present study is served well by simplifying the physics as much as possible while retaining the most relevant geometric complexity. It should be noted that although the flow is being modeled as stationary (i.e. constant boundary conditions), a transient flow solver is used for simulations. This is due to minor instabilities in the averaged turbulent flows typically observed at higher Reynolds numbers, as discussed in Section 5.3.2.

5.2. Aerodynamic Indicators

One major goal of the present study is to propose a set of relevant aerodynamic indicators which may be related to clinical symptoms. The primary aerodynamic indicator is the flow resistance, which measures the work required to breathe by relating the flow rate and pressure differential across the trachea. An airway with a higher resistance to flow will undoubtedly be correlated with dyspnea (difficulty breathing). Additional aerodynamic indicators of airway symptoms may be proposed based on physiology. For example, the increased incidence of infection in airways has been linked to dysfunction of mucociliary transport [37]. It is likely that abnormally high levels of surface shear related to stenosis can damage the cilia and contribute to such mucociliary dysfunction, though the clinical correlation has not been investigated specifically for stenosis patients. Nonetheless, it may be useful to quantify the shear forces in the stenotic trachea. In the condition of excessive dynamic airway collapse, the trachea walls are weakened, allowing suction pressures within the trachea to decrease its cross-sectional area by 50-80% [25]. Hence, it may also be useful to quantify the static pressures within the airflow.

In order to properly characterize flow resistance, shear stresses, and wall normal stresses from the CFD simulations, the following dimensionless parameters are defined:

$$\mathrm{Re_D} = \frac{VD}{\nu}, \qquad K = \frac{\Delta P}{\frac{1}{2}\rho V^2}, \qquad C_{f,\max} = \frac{\tau_{w,\max}}{\frac{1}{2}\rho V^2}, \qquad C_{p,\min} = \frac{p_{w,\min}}{\frac{1}{2}\rho V^2} \tag{5.1}$$

where $\mathrm{Re_D}$ is the Reynolds number of the mean flow, K is the loss coefficient of the trachea, $\tau_{w,\max}$ is the maximum wall shear stress, $p_{w,\min}$ is the minimum value of the static pressure at the wall, $C_{f,\max}$ is the maximum value of the local skin friction coefficient, $C_{p,\min}$ is the minimum value of the pressure coefficient, V is a reference velocity, D is a reference length scale, ν is the kinematic viscosity of air, and ρ is the density of air. The reference velocity V used to calculate these parameters is the mean-flow normal velocity calculated a-priori from the mass flow rate and median open area in the trachea region. The reference diameter D for the Reynolds number is the median hydraulic diameter of the trachea between glottis and carina. The reported pressure drop ΔP refers to the difference in mass-flow-averaged total pressure between the glottis cross-section and carina cross-section. The mass-flow average is defined in Eq. (4.1).

By dimensional analysis, these dimensionless parameters may be correlated to the geometric length scales ℓ_i/D $(i = 1, 2, 3, \dots)$ via generalized functions as

$$K = \hat{f}_1\left(\mathrm{Re_D}, \frac{\ell_1}{D}, \frac{\ell_2}{D}, \cdots\right) \tag{5.2}$$

$$C_{f,\max} = \hat{f}_2\left(\mathrm{Re_D}, \frac{\ell_1}{D}, \frac{\ell_2}{D}, \cdots\right) \tag{5.3}$$

$$C_{p,\min} = \hat{f}_3\left(\mathrm{Re_D}, \frac{\ell_1}{D}, \frac{\ell_2}{D}, \cdots\right) \tag{5.4}$$

where each length scale required to completely specify the geometry is included in this correlation. Since the trachea is a complicated organ where each undulation may be associated with a unique length scale, there is a multiplicity of length scales. To mitigate this issue, we consider only the most important length scales and model sensitivities to remaining length scales as an error term ε. As discussed in Chapter 3, the six most obvious anatomical parameters have been identified as

$$\frac{L_{gc}}{D_0}, \qquad \frac{L_{gs}}{D_0}, \qquad \frac{w_s}{D_0}, \qquad \frac{D_g}{D_0}, \qquad \frac{D_s}{D_0} \tag{5.5}$$

where L_{gc} is the glottis-to-carina length, the L_{gs} is the glottis-to-stenosis length, w_s is the stenosis width, D_g is the the glottis hydraulic diameter, D_s is the stenosis hydraulic diameter, and D_0 is the nominal hydraulic diameter (measured as the median between glottis and carina). For the present study, geometric similarity is considered in the glottis diameter ratio (D_g/D_0), trachea aspect ratio (L_{gc}/D_0), and the relative stenosis location (L_{gs}/D_0). Then, the dimensionless ratios may be correlated to Reynolds number and the two remaining geometric parameters, modeling sensitivities to higher-order length scales as a statistical error ε:

$$K = f_1\left(\mathrm{Re_D}, \varsigma, \frac{w}{D_0}\right) + \varepsilon_1 \tag{5.6}$$

$$C_{f,\max} = f_2\left(\mathrm{Re_D}, \varsigma, \frac{w}{D_0}\right) + \varepsilon_2 \tag{5.7}$$

$$C_{p,\min} = f_3\left(\mathrm{Re_D}, \varsigma, \frac{w}{D_0}\right) + \varepsilon_3 \tag{5.8}$$

where $\varsigma = 1 - (D_s/D_0)^2$ is the approximate area reduction of the stenosis relative to the nominal area, w/D_0 is the relative stenosis width (dropping "s" notation), and the error terms are assumed to be negligible ($|\varepsilon_i/f_i| \ll 1$, for $i = 1, 2, 3$).

To directly establish the correlation between these aerodynamic indicators and breathing symptoms, the trachea of symptomatic patients must be scanned and simulated with a statistically-significant sample size. As such clinical studies are presently nonexistent, the sensitivities of the proposed aerodynamic indicators will be correlated to geometric variations and left for further clinical investigation.

5.3. Reduction of the Computational Domain

In order to avoid the modeling difficulties associated with flexible tissues in the pharynx and superglottic larynx – as well as those of flow-splitting between the bronchi – it is desirable to restrict the domain of the analysis to the region between the glottis and the carina. However, placing an inlet boundary so close to the region of interest may sensitize the results to the details of the inlet boundary condition. Hence, special care must be taken

in the prescription of this inlet boundary.

5.3.1. Extended Airway Domain

Preliminary calculations on a full airway from the nasal volume to the carina are performed in order to understand the sensitivity to the boundary conditions, so that the region above the glottis may be removed from the computational domain. A mesh was generated using ICEM CFD as described in Section 4.2, using a global cell size of $\Delta = 16.4$. The model and mesh used for this analysis is shown in Figure 5.1. Note that a straight domain extension was added in-between the carina and outlet boundary in order to avoid any potential recirculation region near the outlet. The near-wall inflation layer region was designed to have a first-cell y^+ value of approximately 1, in accordance with the k-ω turbulence model [4], with a smooth transition to the freestream mesh. Since the turbulence conditions are unknown at the inlet boundary, all four combinations of inlet turbulence intensity $I = [0.01\%, 5\%]$ and eddy viscosity ratio $\nu_t/\nu = [0.01, 10]$ were considered. Note that these values represent lower and upper bounds of reasonable values for turbulence parameters [5]. Simulations are run with flow rates giving Reynolds numbers of approximately $\mathrm{Re_D} \approx 500$, 1000, 1500, 2000, and 2500, based on the average hydraulic diameter of the trachea and velocities at the average trachea cross-section.

5.3.2. Transient Solution

As mentioned previously, a transient solver was used for all simulations due to minor flow instabilities, which prevent the mean flow from being truly steady. Since the flow was initialized using the Hybrid Initialization routines described in Chapter 2, it is prudent to examine the convergence to a stationary state – that is, either a steady flow or a stable limit cycle. In order to monitor this convergence, the difference in total pressure from inlet to outlet of the model ΔP is measured over flow time t. The flow time is nondimensionalized by the typical residence time of a fluid particle L/V, where L is the model length and V is the average velocity within the model. The relative error between instantaneous pressure drop and the median pressure drop is plotted against dimensionless "flow-through time"

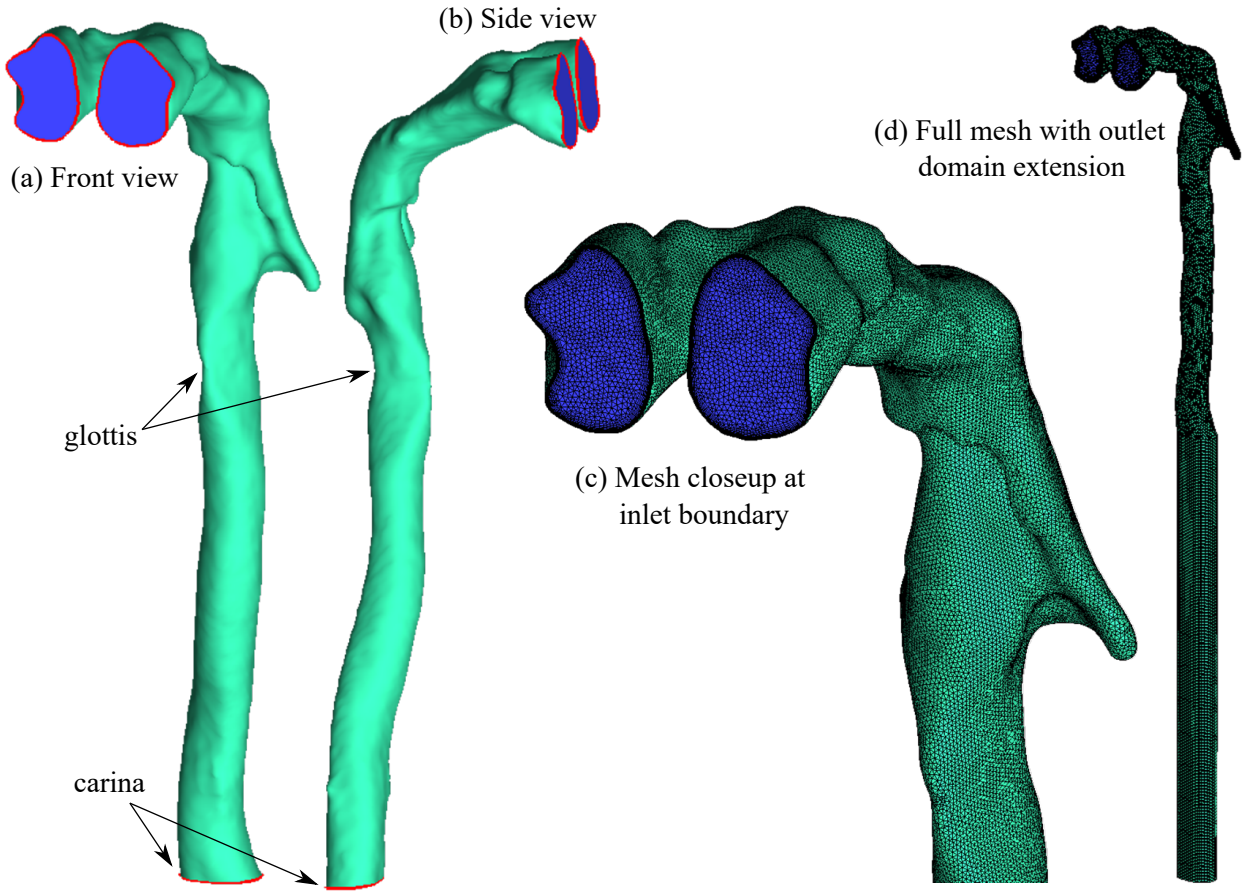

Figure 5.1. (a) Front and (b) side views of full airway model from nasopharynx to carina, with computational grid shown (c) for inlet boundary and (d) in its entirety. Note the straight domain extension at the outlet to avoid a recirculation region at the imposed boundary condition.

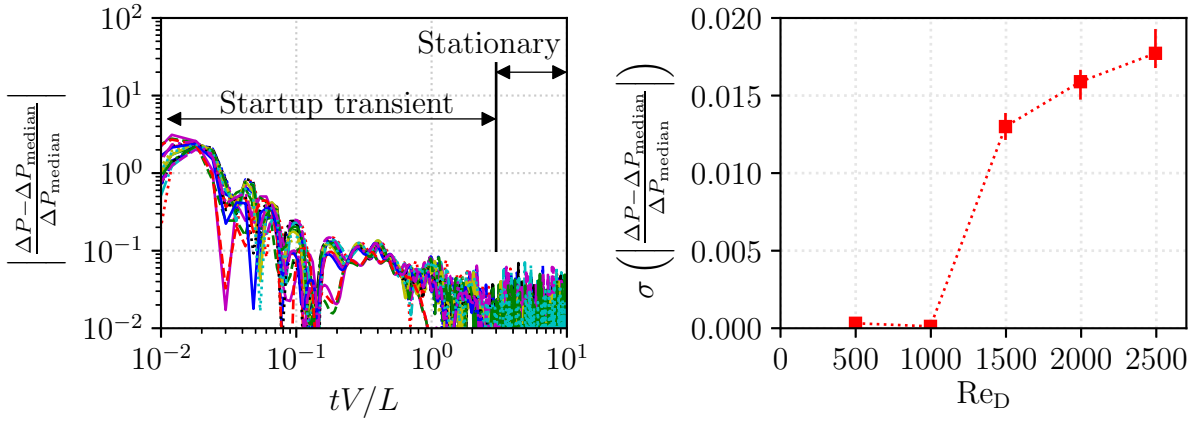

Figure 5.2. Convergence of total pressure drop over dimensionless time for all full airway simulations, relative to median pressure drop (left panel); and standard deviation of scaled pressure drop for $tV/L > 5$ (right panel) for different Reynolds numbers.

in the left panel of Figure 5.2. The right panel shows the standard deviation of this scaled pressure drop (for $tV/L > 5$) as a measure of unsteadiness for different Reynolds numbers. The mean-flow unsteadiness observed here can be attributed to hydrodynamic instabilities associated with shear. It is evident that the solution converges to within approximately 4% of its average value for $tV/L \geq 3$, after which the solution may be considered to be stationary. It is also evident that the amount of deviation relative to the average is dependent on Reynolds number, with very little unsteadiness occurring at $\text{Re}_\text{D} < 1000$. At $\text{Re}_\text{D} = 2500$, the standard deviation of pressure drop is approximately 1.8% of the median pressure drop. Therefore, running simulations up to $tV/L = 10$ should give sufficiently-converged, stationary solutions which are independent of the initialized conditions for all Reynolds numbers.

5.3.3. Flow Structures

The primary flow structures in the full airway model can be visualized qualitatively via streamlines, as shown in Figure 5.3. Here, regions of recirculation occur in the pharynx (i.e. above the glottis) and just after the glottis. These recirculation regions are caused by boundary layer separation due to the adverse pressure gradient associated with increasing cross-sectional area, and may be visualized as velocities in the positive "z" direction in

Figure 5.3. The maximum velocity occurs at the smallest cross-sectional area: the glottis.

In order to more clearly identify the flow characteristics, flow quantities may be integrated over the cross-sectional area of the airway along the medial axis, as shown in Figure 5.4. Here, the nondimensional parameters of scaled, area-averaged normal velocity v_n/V, flow-averaged turbulence intensity $\bar{I}$, eddy viscosity ratio $\bar{\nu}_t/\nu$, flow reversal ratio Q_r/Q, flow-averaged total pressure coefficient $\bar{C}_{p,t}$, flow-averaged pressure coefficient $\bar{C}_p$, and the perimeter-averaged skin friction coefficient $\bar{C}_f$ are plotted against scaled distance along the medial axis s/D_0. Note that the glottis is located at $s/D_0 = 0$. It is clear from these plots that the flow reversal (recirculation) regions are in the nasopharynx several diameters upstream of the glottis, as well as just after the glottis. The magnitude of flow reversal increases with Reynolds number, and the flow tends to separate earlier at higher Reynolds numbers. The reattachment location upstream of the glottis is independent of Reynolds number, likely due to the fact that the reattachment is driven by the favorable pressure gradient caused by flow acceleration into the glottis region. The turbulence intensity plot shows that the recirculation regions tend to produce turbulence. As such, the turbulence intensity and eddy viscosity ratio are highly sensitive to the Reynolds number. It is also shown that the skin friction coefficient scales very well with $\mathrm{Re_D^{-1/2}}$, in agreement with boundary layer theory [31]. As expected, the shear stresses take maximum values at the glottis, with local minima in the recirculation regions and local maxima at the reattachment locations. Note that the skin friction coefficient represents a perimeter-averaged value, so regions of flow reversal do not necessarily correspond to negative values of averaged skin friction coefficient.

5.3.4. Glottis Conditions

In order to determine the appropriate turbulence boundary conditions for a model beginning at the glottis, the flow-averaged turbulence intensity and eddy viscosity ratio are computed at the glottis for each case of Reynolds number and upstream turbulence boundary condition. As shown in Figure 5.5, the glottis conditions are relatively insensitive to

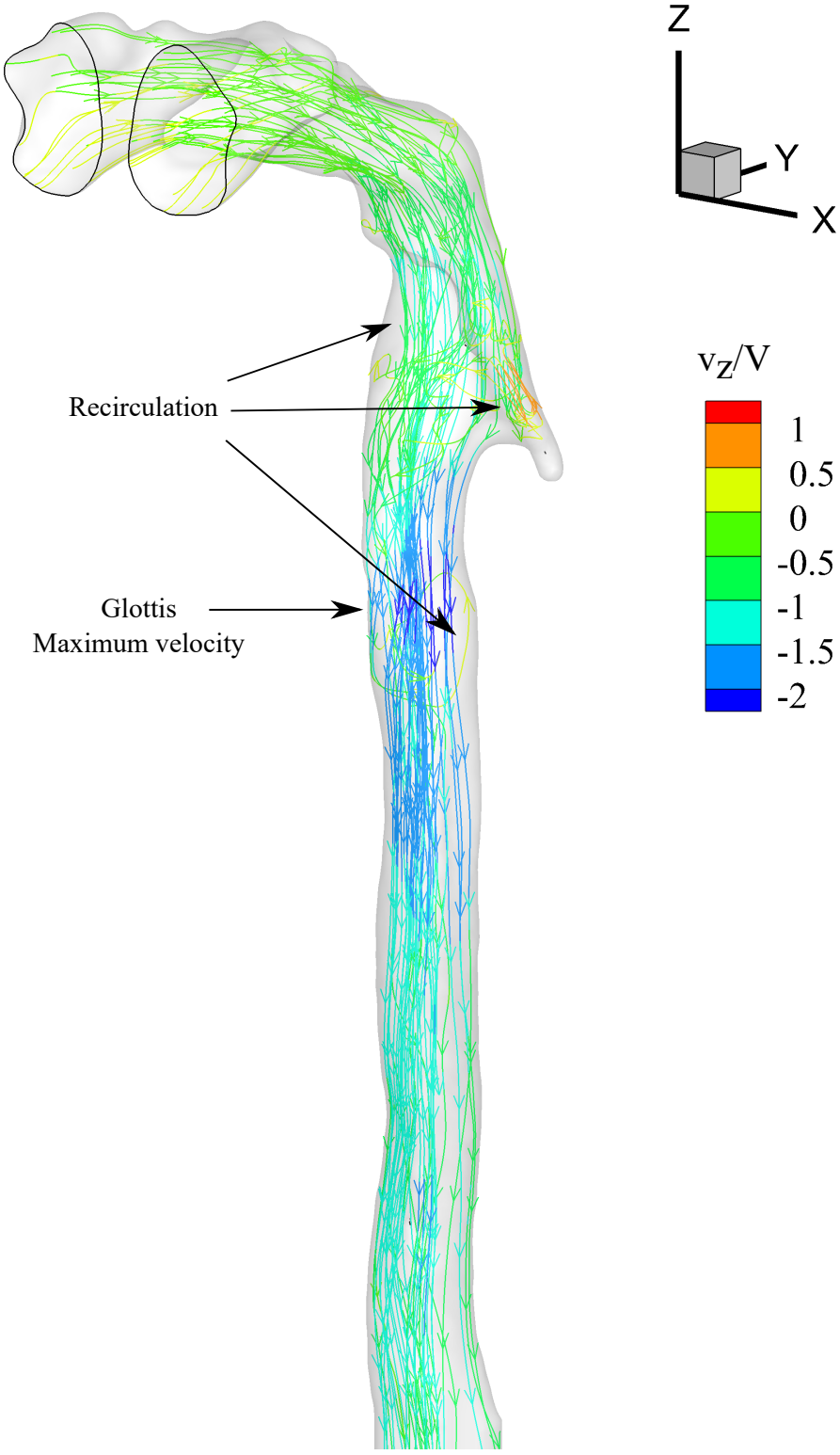

Figure 5.3. Streamlines for flow in airway from nasopharynx to carina at trachea Reynolds number of 2500.

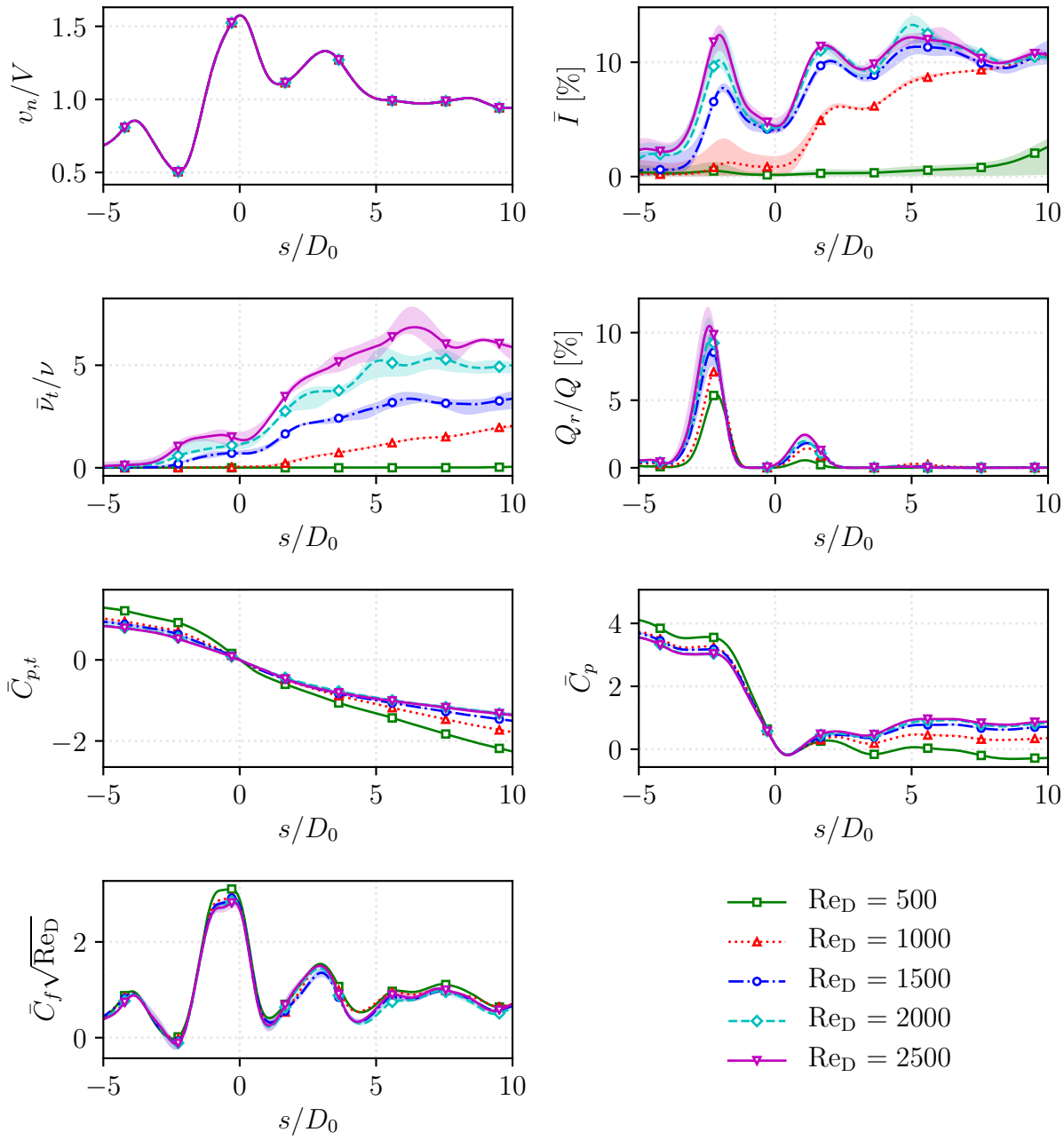

Figure 5.4. Integrated and averaged quantities for flow in airway along the dimensionless distance along the medial axis s/D_0, for $500 \geq \mathrm{Re_D} \geq 2500$.

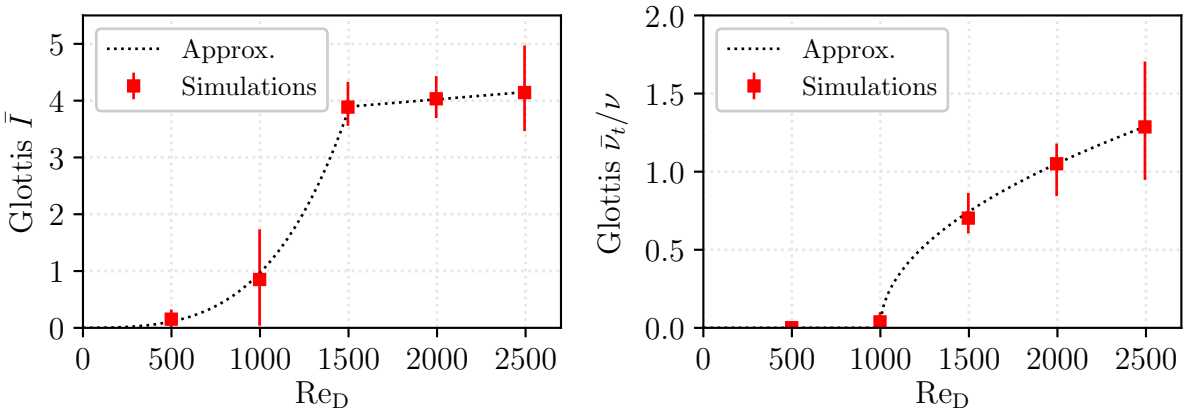

Figure 5.5. Flow-averaged turbulence intensity $\bar{I}$ and eddy viscosity ratio $\bar{\nu}_t/\nu$ at the glottis cross-section, computed from full upper airway analysis for a range of Reynolds numbers and turbulence boundary conditions.

inlet turbulence boundary conditions, and are correlated most strongly to the characteristic Reynolds number of the flow. The error bar shown for each Reynolds number indicates the full range of values in the four cases of turbulence boundary conditions. Note that both turbulence parameters are relatively low until a Reynolds number of approximately 1000, after which the glottis turbulence intensity is approximately 4% and the glottis turbulence viscosity ratio begins to increase at a rate of approximately 1 per 1000 units of Reynolds number. As illustrated in Figure 5.5, it was found that the following correlations approximate the average glottis turbulence intensity $\bar{I}_{\mathrm{glottis}}$ and eddy viscosity ratio $(\bar{\nu}_t/\nu)_{\mathrm{glottis}}$:

$$\bar{I}_{\mathrm{glottis}} = \begin{cases} \left[0.64\left(\frac{\mathrm{Re_D}}{1000}\right)^2 + 0.345\left(\frac{\mathrm{Re_D}}{1000}\right)\right]^2, & \mathrm{Re_D} < 1500 \\ 0.257\left(\frac{\mathrm{Re_D}}{1000}\right) + 3.51, & \mathrm{Re_D} \geq 1500 \end{cases} \tag{5.9}$$

$$(\bar{\nu}_t/\nu)_{\mathrm{glottis}} = \begin{cases} 10^{-3}, & \mathrm{Re_D} < 1000 \\ \sqrt{1.11\left(\frac{\mathrm{Re_D}}{1000} - 1\right)}, & \mathrm{Re_D} \geq 1000 \end{cases} \tag{5.10}$$

These values may be used to specify the turbulence inlet conditions for simulations on truncated domains, where the inlet boundary is placed at the glottis.

5.4. Simulations on Truncated Domains with Stenosis

By simulating the flow in an extended domain from the nasopharynx to the carina, the groundwork has been laid for simulations on truncated domains. Conditions for convergence have been set on the basis of a pressure drop residual and the turbulence parameters at the glottis have been quantified. Similar flow structures are expected in the truncated domains if appropriate inlet boundary conditions are specified.

5.4.1. Anatomical Variations

As a basis for calculations, a baseline airway model was generated from a CT scan of an 11-year-old female patient with no reported stenosis condition, using the methods described in Section 2.2. The domain of the airway is restricted from several diameters upstream of the glottis to just upstream of the bifurcation at the carina. As described in Section 2.2, the baseline model was then augmented with an artificial stenosis with four variations of stenosis width (w/D_0) and four variations of stenosis area reduction (ς), and a consistent stenosis location relative to the glottis (L_{gs}/D_0). In total, 17 models are considered: 1 baseline model and 16 models with stenosis variations. Each of these 17 models is illustrated in Figure 5.6. The stenosis area reduction ς and relative width w/D_0 are shown, measured using the wavelet-based algorithms presented in Chapter 3. Note that each model in Figure 5.6 corresponds to the medial axis data of Figure 3.8. The values of ς and w/D_0 are not perfectly uniformly distributed on a rectangular grid since the method of creating the stenosis in software is not exact and is subject to three-dimensional complications. This should not impact the results of the present study since the stenosis parameters ς and w/D_0 have been identified from the resulting geometry rather than its constructional parameters.

5.4.2. Computational Mesh

For each airway model, a mesh was generated using ICEM CFD as described in Section 4.2, using a global cell size of $\Delta = 16.4$. An example of a mesh used for this analysis is shown in Figure 5.7. A straight domain extension was added in-between the carina and

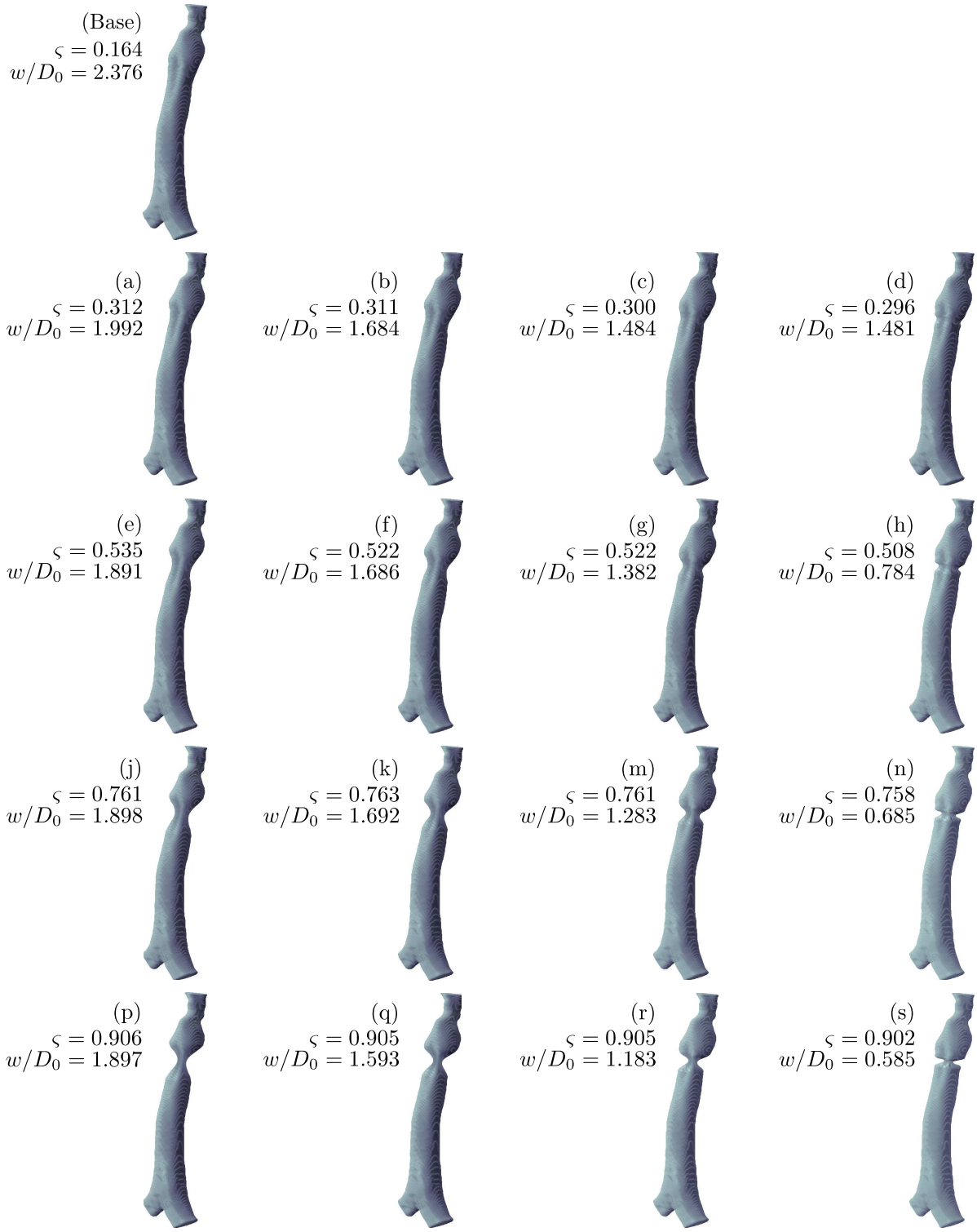

Figure 5.6. Models of baseline model and each variation of stenosis to be used in simulations, with stenosis area reduction ς and width w/D_0 measured by wavelet methods of Chapter 3 (compare to Figure 3.8). Note that although the bifurcation is shown here, this portion of the domain is removed for simulations.

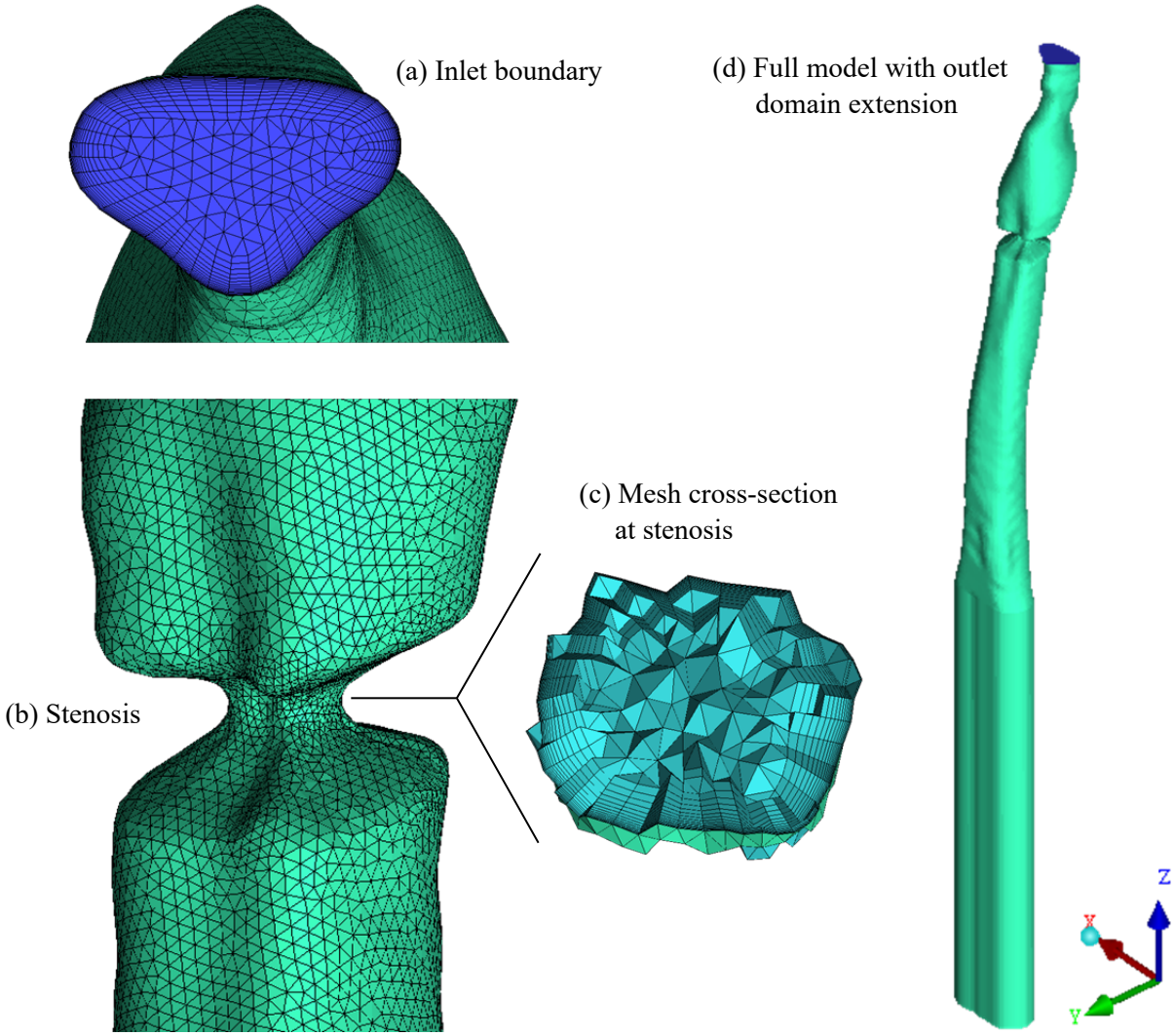

Figure 5.7. Computational mesh at (a) inlet boundary and (b) wall boundary at stenosis, with (c) cross-section of mesh at stenosis. (d) Full model for CFD with straight domain extension at the outlet to avoid a recirculation region at the imposed boundary condition.

outlet boundary in order to avoid any potential recirculation region near the outlet. The near-wall inflation layer region was designed to have a first-cell y^+ value of approximately 1, with a smooth transition to the freestream mesh.

5.4.3. Transient Solution

For each of the 17 models described in Section 5.4.1, five flow rates were simulated corresponding to Reynolds numbers spanning $500 < \mathrm{Re_D} < 2500$. The inlet turbulence conditions were uniquely set by the Reynolds number, using the equations formulated in Section 5.3.4. The velocity at the inlet boundary was prescribed to be normal to the boundary, with a power-law profile in terms of the distance from the wall y as

$$\frac{v}{v_{\max}} = 1 - \left(1 - \frac{y}{y_{\max}}\right)^8 \tag{5.11}$$

This velocity profile was examined to be reasonably accurate from the results of the domain reduction study of Section 5.3. The "bluntness" of the profile may be attributed to the fact that the favorable pressure gradient leading to the glottis region causes the flow to become more uniform across the cross-section. Additional sensitivities to this inlet boundary condition are examined in Appendix B.

Each case was run with a transient solver up to a final time of 10 flow-through times ($tV/L = 10$) with a fixed timestep based on maintaining a Courant number of less than 10 at the smallest cross-section, which is adequate for the time-implicit method used. Since many of the simulations were unstable – thus, unable to achieve steady-state – the extent of unsteadiness is indicated by the standard deviation of relative pressure drop measured for $tV/L > 5$. The standard deviation for relative pressure drop is shown in Figure 5.8 as a function of area reduction (left) and Reynolds number (right). The error bars indicate 95% confidence intervals. Note here that the unsteadiness is primarily a function of area reduction, but much variation exists between cases. The most unsteady cases are at moderately high area reductions ($\varsigma \approx 0.75$) and moderate Reynolds numbers ($\mathrm{Re_D} \approx 1500$).

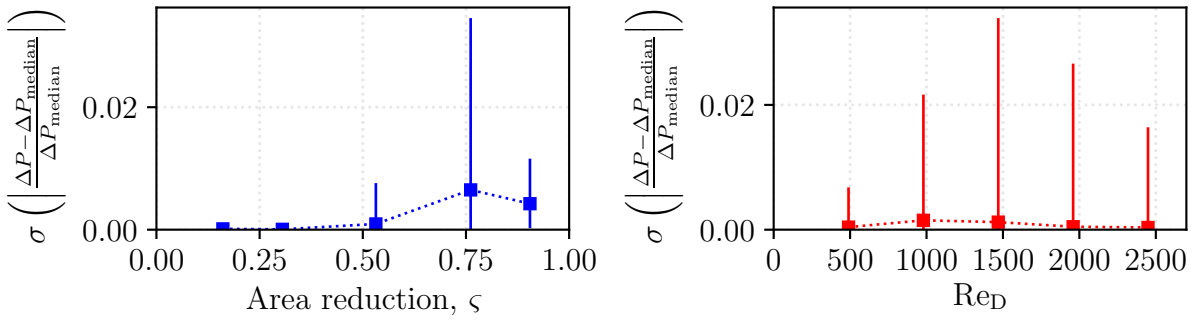

Figure 5.8. Standard deviation of normalized pressure differential for $tV/L > 5$ as a function of area reduction ς (left panel) and Reynolds number Re_D (right panel).

This non-monotonic behavior indicates competing mechanisms. At lower Reynolds numbers and area reductions, the inertial forces are not high enough to incite instability; however, at high Reynolds numbers, this unsteadiness is shifted toward the smaller scales of turbulence and contributes to eddy viscosity in the mean flow via the turbulence model. The mean-flow oscillations are then damped by the eddy viscosity. Examples of a stable (low-deviation) and two unstable (high-deviation) simulations are illustrated in Figure 5.9. Here, the moderately unstable simulation ($\sigma = 4.38 \times 10^{-3}$) contains a discrete mode of oscillation with a low relative amplitude, while the most unstable simulation ($\sigma = 3.34 \times 10^{-2}$) contains a broadband spectrum of oscillations (i.e. chaotic behavior).

In order to examine the qualitative behavior of such oscillations, the flow field with broadband frequency content ($\sigma = 3.34 \times 10^{-2}$) is shown over several instants in time in Figure 5.10, where $t_1 < t_2 < \cdots < t_6$. Here, the velocity magnitude is plotted on cross-sections along the length of the trachea (red indicates high speeds, blue indicates low speeds). Note the relatively high fluid speeds at the stenosis – the small red cross-section, and the jet regions downstream of the glottis and the stenosis. It is clear from this figure that the overall flow structures in the unstable case remain qualitatively coherent over time, while the details of their shapes may vary slightly.

It should also be noted that the time scales of oscillations due to instability are on the order of $\Delta tV/L \sim 1$, i.e. the time scale for one particle to traverse the trachea. From the

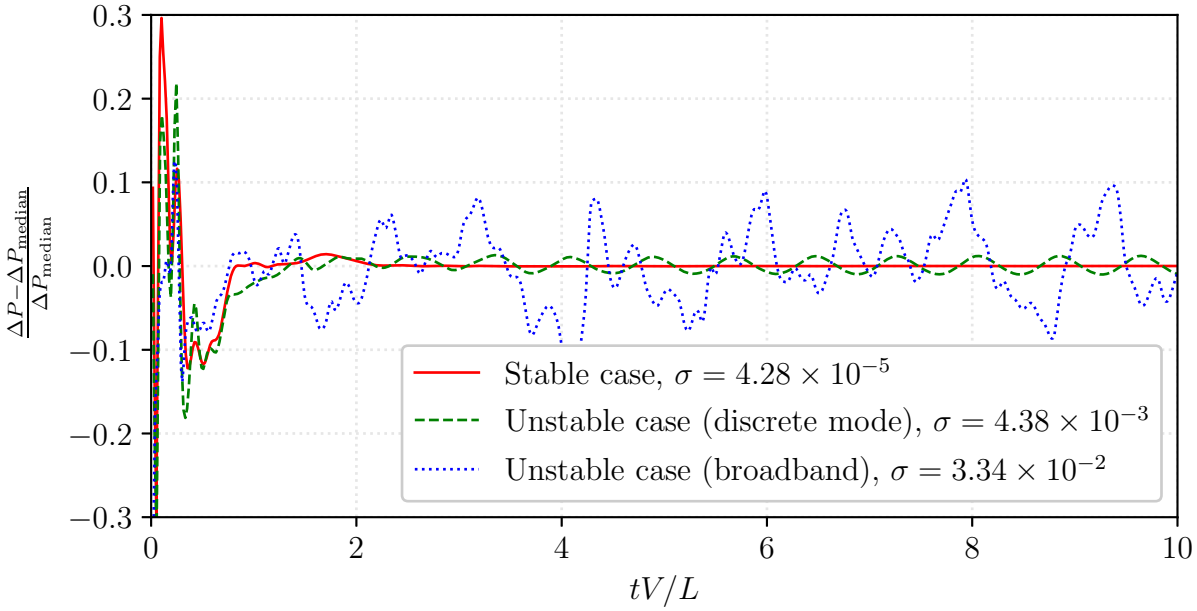

Figure 5.9. Examples of stable and unstable simulations, as qualified by the standard deviations of normalized pressure differential for $tV/L > 5$. The relative amplitudes of oscillation correlate positively with the standard deviations σ, and oscillations may occur with discrete modes or with broadband frequency content.

statistics of pediatric ventilation discussed in Section 1.3, time scales for inspiration are typically $20 < tV/L < 60$; thus, the oscillations seen here exist on a much shorter time scale than the breathing cycles.

5.4.4. Flow Structures

The overall flow structures for a representative case ($\varsigma = 0.905$, $w/D_0 = 1.145$, $\text{Re}_\text{D} \approx 2500$) are shown in Figure 5.11. In the left panel it is shown that the skin friction coefficient is at a local maximum at the minimum-area cross-section of the stenosis, as expected. It is also seen that there are some elevated wall shear stresses on one side of the trachea downstream of the stenosis. This is due to the stenotic jet impinging on the wall, as can be seen in the right panel. The center panel shows the local pressure coefficient at the wall. It can be noted that the minimum pressure occurs at the stenosis due to a Bernoulli effect related to fluid acceleration. The pre-stenotic region contains considerably higher pressure coefficients than the post-stenotic region due to the large pressure gradient

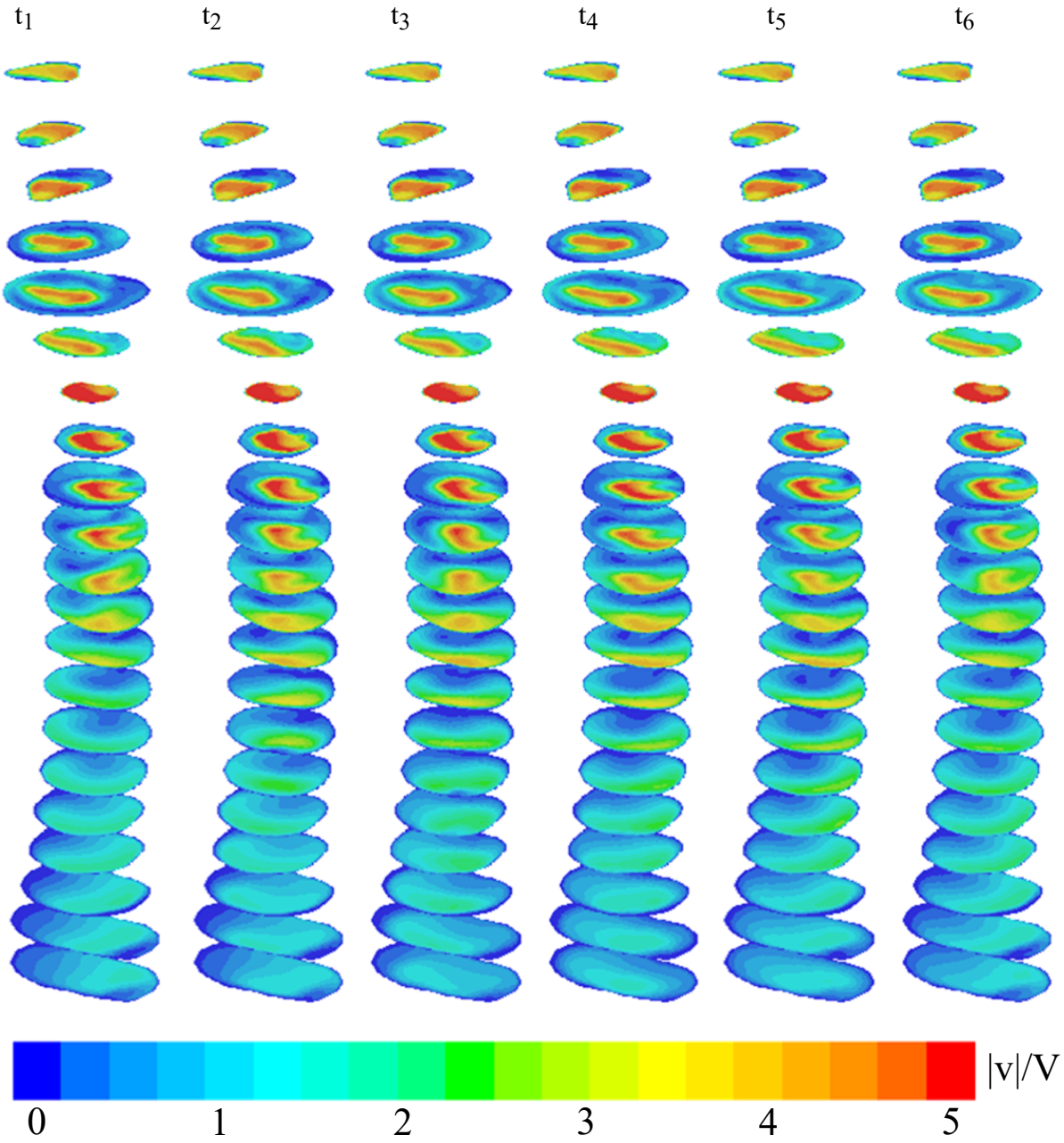

Figure 5.10. Relative velocity magnitude (scaled by median velocity V) contours on cross-sections of stenotic trachea for six instantaneous times ($t_1 < t_2 < \cdots < t_6$) for flow field with broadband frequency content ($\sigma = 3.34 \times 10^{-2}$), as shown in Figure 5.9.

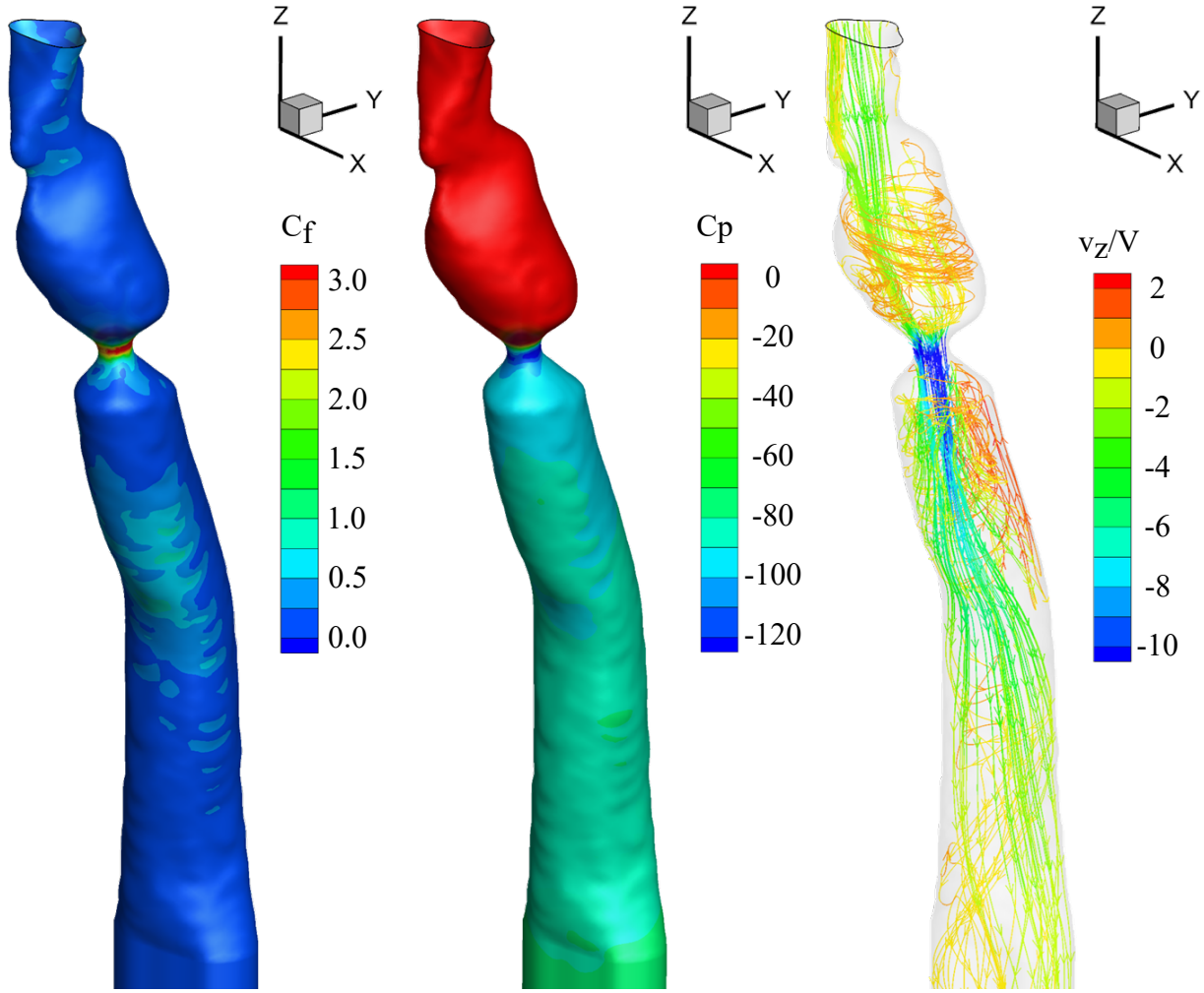

Figure 5.11. Visualization of skin friction coefficient (left panel), pressure coefficient (middle panel), and velocity streamlines colored by z-velocity normalized with respect to the median velocity V (right panel).

required to overcome the viscous dissipation associated with the flow restriction. From the velocity streamline plot (right panel), it is evident that the stenosis produces an air jet downstream of the stenosis surrounded by a large region of recirculation. Additionally, the region between the glottis and stenosis contains an appreciable recirculation region before the flow is accelerated through the stenosis.

The flow characteristics are more clearly examined by integrating flow quantities over the cross-sectional area of the airway along the medial axis, as shown in Figure 5.12. Here, the nondimensional parameters of scaled, area-averaged normal velocity v_n/V, flow-

averaged turbulence intensity $\bar{I}$, eddy viscosity ratio $\bar{\nu}_t/\nu$, flow reversal ratio Q_r/Q, flow-averaged total pressure coefficient $\bar{C}_{p,t}$, flow-averaged pressure coefficient $\bar{C}_p$, and the perimeter-averaged skin friction coefficient $\bar{C}_f$ are plotted against scaled distance along the medial axis s/D_0. Note that the glottis is located at $s/D_0 = 0$.

It is interesting in this case that most of the scaled flow characteristics each seem to collapse to a narrow band for the full range of Reynolds numbers. Here, the stenosis is located at approximately $s/D_0 = 2.4$ as seen in the scaled normal velocity (v_n/V) plot. The normal velocity is driven by area, so there is no variation with respect to Reynolds number, by-construction. At the stenosis, a precipitous drop in pressure coefficient $\bar{C}_p$ is seen due to a Bernoulli effect. The fluid jet caused by the stenosis gives rise to a large amount of viscous dissipation, as seen by the steep gradients of total pressure coefficient $\bar{C}_{p,t}$ after the stenosis. Note that the flow-averaged total pressure may only decrease due to entropy-generating phenomena such as viscous dissipation. Regions of flow reversal are indicated by nonzero values of Q_r/Q in the regions between the glottis and stenosis and the post-glottic region. The flow reattachment point occurs when Q_r/Q approaches 0 – i.e. where there is no portion of the cross-sectional area which contains reversed flow. The flow reattachment point is relatively insensitive to the Reynolds number at approximately $s/D_0 = 7.5$, which is approximately 5 diameters downstream of the stenosis. It is noted that the skin friction coefficient $\bar{C}_f$ scales well with $\mathrm{Re_D}^{-1/2}$, and its local maximum clearly occurs at the stenosis.

5.5. Correlations Between Aerodynamics and Anatomy

While the flow visualizations of Figure 5.11 and the integrated flow quantities of Figure 5.12 provide useful information for individual models, a yet elevated perspective must be taken to understand the variations of aerodynamics with respect to anatomical differences. Here, the aerodynamic indicators introduced in Section 5.2 are examined with respect to variations in stenosis width, area reduction, and Reynolds number.

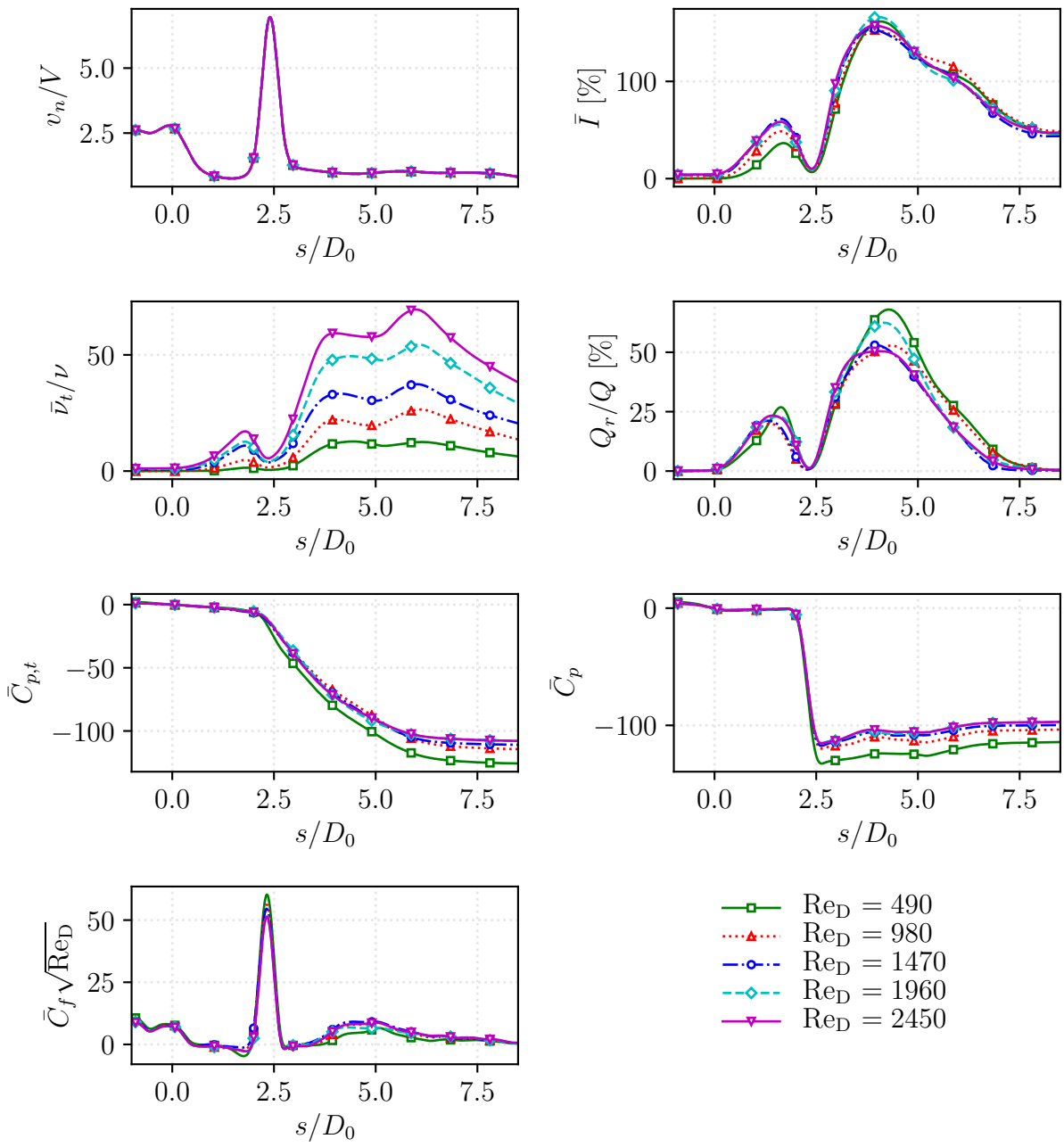

Figure 5.12. Integrated and averaged quantities for flow in stenotic trachea ($\varsigma = 0.905$, $w/D_0 = 1.145$) along the dimensionless distance along the medial axis s/D_0, for $500 \leq \mathrm{Re_D} \leq 2400$.

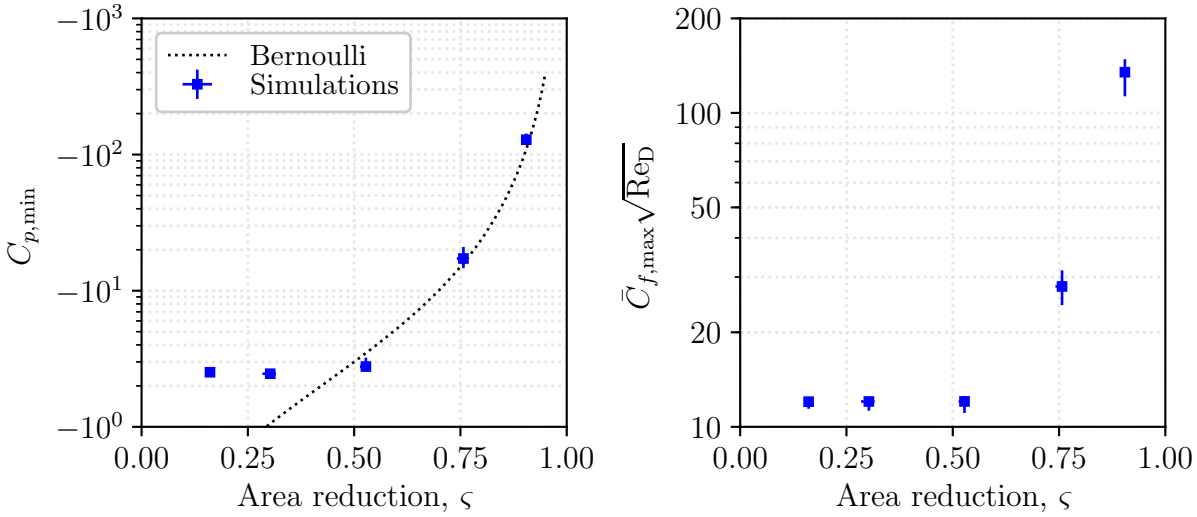

Figure 5.13. Minimum pressure coefficient $\bar{C}_{p,\min}$ and maximum skin friction coefficient $\bar{C}_{f,\max}$ for all simulations versus area reduction ς. A 95% confidence interval is indicated with error bars.

5.5.1. Pressure and Skin Friction Coefficients

Firstly, the minimum pressure coefficient $\bar{C}_{p,\min}$ and maximum skin friction coefficient $\bar{C}_{f,\max}$ are shown in Figure 5.13 as a function of area reduction ς with error bars indicating 95% confidence interval. Here, it is clear that these two aerodynamic quantities are strong functions of stenosis area reduction ς, with only weak sensitivities to the stenosis width w/D_0 and Reynolds number (except for the uniform scaling of $\bar{C}_{f,\max}$ by $\mathrm{Re_D}^{-1/2}$). In both cases, it is clear that a 50% area reduction is a threshold value for the minimum pressure coefficient and the maximum skin friction coefficient. This indicates that the minimum pressure and maximum shear stress inside the trachea is not driven by the stenosis until a threshold of 50% area reduction. For $\varsigma > 0.5$, the minimum pressure coefficient occurs at the throat of the stenosis, agreeing well with the result of the Bernoulli equation, assuming negligible viscous pressure losses between the glottis and stenosis:

$$C_{p,\min,\mathrm{Bernoulli}} \approx 1 - (1-\varsigma)^{-2} \tag{5.12}$$

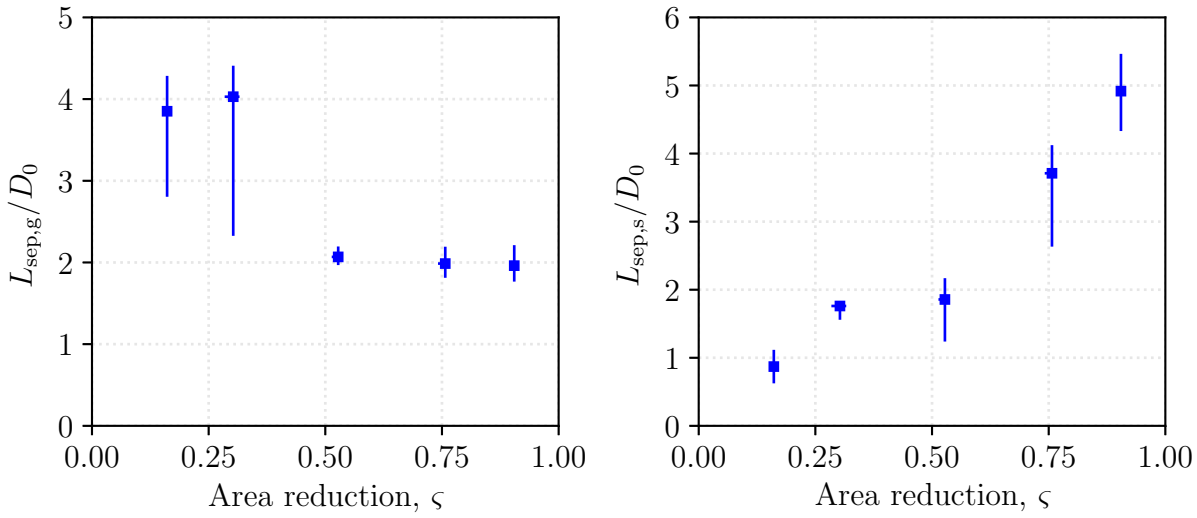

Figure 5.14. Scaled length of separation region immediately behind glottis $L_{\text{sep,g}}/D_0$ and immediately behind stenosis $L_{\text{sep,s}}/D_0$ for all simulations versus area reduction ς. A 95% confidence interval is indicated with error bars.

The skin friction coefficient scaled by the square root of Reynolds number is also explained mostly by area reduction, remaining relatively constant for $\varsigma < 0.5$ and increasing precipitously for $\varsigma > 0.5$.

5.5.2. Separation Region Lengths

Another quantity of interest is the relative size of the separation regions. It was shown qualitatively in Figure 5.11 that there generally exists a separation region behind the glottis, which reattaches in the favorable pressure gradient leading up to a stenosis constriction. Then, a second separation region exists behind the stenosis, which reattaches more gradually several diameters downstream of the stenosis. We define a separation region as the region where $Q_r/Q > 0.01$ – that is, where a net flow rate in the reversed direction is larger than 1% of the total flow rate. We may examine the lengths of the post-glottis separation length $L_{\text{sep,g}}/D_0$ and post-stenosis separation length $L_{\text{sep,s}}/D_0$ individually, as shown in Figure 5.14 with error bars indicating a 95% confidence interval. Here, two trends are clear. Firstly, the post-glottis separation region (left panel) is much longer for low area reductions $\varsigma < 0.5$. This can be attributed to the fact that for large ς, the favorable pres-

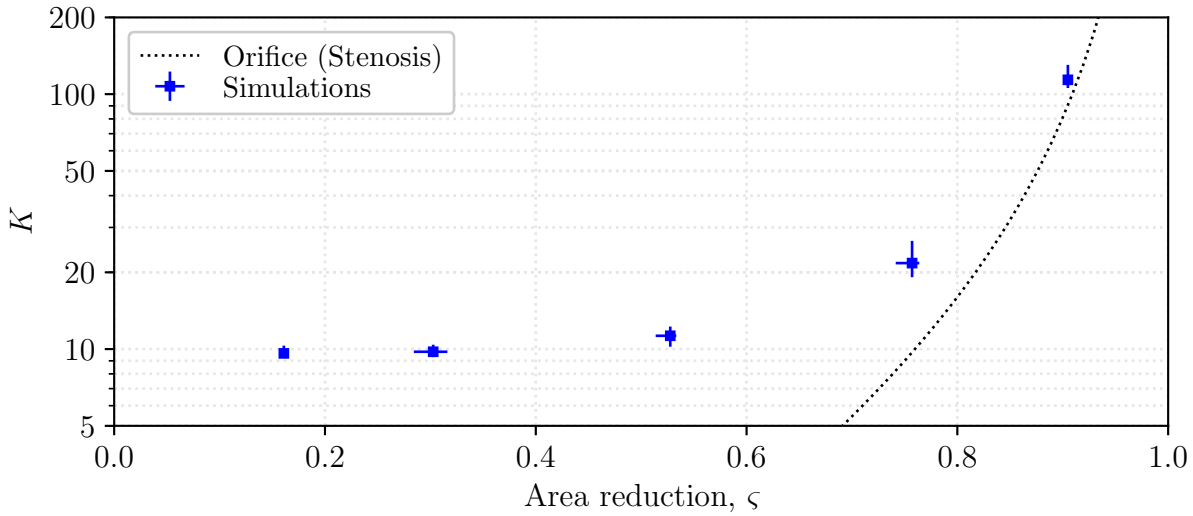

Figure 5.15. Loss coefficient K as a function of area reduction ς, compared to the loss coefficient of an orifice plate given in Eq. (5.13). A 95% confidence interval is indicated with error bars.

sure gradient leading to the stenosis causes the flow to reattach – thus, it is driven by the geometry. Secondly, the length of the post-stenosis separation region (right panel) tends to increase with increasing area reductions. This can be attributed to the increased relative momentum of the stenotic jet with increasing ς. This additional momentum carries farther before diffusing into the mean flow via fluid viscosity.

5.5.3. Loss Coefficient

Finally, the overall pressure drop is quantified by the loss coefficient K, which indicates the work required to breathe associated with the flow through the trachea. The loss coefficient for all Reynolds numbers and variations of anatomy are shown in Figure 5.15 with error bars indicating a 95% confidence interval. Since it is expected that the loss coefficient should resemble that of an orifice for large area reductions ($\varsigma \to 1$), the orifice loss coefficient is compared to the results as

$$K_{\text{orifice}} = \left(\frac{\varsigma}{1-\varsigma}\right)^2 \tag{5.13}$$

It is clear from the figure that the loss coefficients are generally much higher than that of the orifice except for high area reductions, where the results seem to agree with the orifice equation. Thus, there is a competition of mechanisms for the viscous pressure losses. At low area reductions, the pressure loss is dominated by other mechanisms: losses associated with the post-glottis expansion as well as the "major losses" associated with all internal flows. Clearly, the majority of variations within the loss coefficient data can be explained by the area reduction ς. The sensitivities of K with respect to Reynolds number $\mathrm{Re_D}$ and stenosis width w/D_0 are nearly negligible compared to the sensitivity to ς. In order to create a general correlation for these results, an orifice-type equation is used, similarly to the work of Young & Tsai [47]. Here, the deviations from the orifice calculation are separated into primary effects K_0 and secondary effects K_1, as

$$K = \underbrace{K_0(\varsigma)}_{\substack{\text{primary}\\ \text{effects}}} \underbrace{[1 + K_1(\varsigma, w/D_0)]}_{\text{secondary effects}} \underbrace{\left(\frac{\varsigma}{1-\varsigma}\right)^2}_{\text{orifice losses}} \tag{5.14}$$

Assuming that $K_1 \ll 1$, the functions K_0 and K_1 may be fit sequentially such that K_1 may be considered a next-order "correction" to the K_0 fit. In order to fit the functions to the data, a least-squares estimation of parameters was used with a functional form chosen by the author to most simply and accurately represent the data. Representative fits for K_0 and K_1 were found as

$$K_0(\varsigma) = 2.708 \times 10^5 \exp\left(-12.74\sqrt[3]{\varsigma}\right) \tag{5.15}$$

$$K_1(\varsigma, w/D_0) = -0.845\left(\frac{w}{D_0} - 1.398\right)\left[(\varsigma - 0.161) - 0.926(\varsigma - 0.161)^2\right] \tag{5.16}$$

which are shown in the left and right panels of Figure 5.16, respectively. The fit for K_0 is shown alongside the data, with a 95% confidence interval. Evidently, the Reynolds number and stenosis width play only a minor role in K_0. The bivariate data for K_1 as a function of both stenosis area reduction ς and stenosis width w/D_0 is shown in the right panel,

with corresponding fits. Note here that $K_1 = 0$ for $w/D_0 = 1.398$. Smaller values of $w/D_0 < 1.419$ represent sharper stenosis transitions and yield larger loss coefficients, while larger values of $w/D_0 > 1.398$ represent more gradual stenosis transitions and yield lower loss coefficients. Clearly, the fit of K_0 is much more accurate than the fit of K_1, while the fit of K_1 is meant only to provide a leading-order sensitivity to stenosis width.

5.5.4. Relative Flow Rate

While the flow correlations developed in the previous sections may be used to calculate the pressure drop given a certain flow rate and anatomical measurements, their clinical significance is not immediately obvious. A more clinically-relevant measure may be derived by assuming that a patient of a certain age can produce a given differential pressure across the trachea. The pressure differential produced by a patient will yield a certain flow rate if their trachea is normal, or some lower flow rate if their trachea contains a stenosis. Hence, we consider the relative flow rate between a stenotic trachea and a corresponding healthy trachea by fixing the differential pressure. Rearranging the definition of loss coefficient K introduced in Eq. (5.1), the pressure differential ΔP is isolated:

$$\frac{2D^2\Delta P}{\mu\nu} = \mathrm{Re}_\mathrm{D}^2 K \tag{5.17}$$

Since the Reynolds number here is based on the median diameter of the trachea, it is independent of the stenosis conditions; thus, the relative flow rate Φ between a stenotic trachea and a corresponding normal trachea is equal to the ratio of their Reynolds numbers:

$$\Phi = \frac{\mathrm{Re}_{\mathrm{D,stenosis}}}{\mathrm{Re}_{\mathrm{D,normal}}} = \sqrt{\frac{K_\mathrm{normal}}{K_\mathrm{stenosis}}} \tag{5.18}$$

Using the resultant fit for K given by Eqs. (5.14), (5.15), and (5.16), the relative flow rate to a normal trachea is calculated for two different trachea widths w/D_0 and shown in Figure 5.17. Here, the normal trachea is defined by $\varsigma = 0.161$ and $w/D_0 = 2.38$. The plot is divided into the three regions of the Myer-Cotton grading system, as described in Chapter

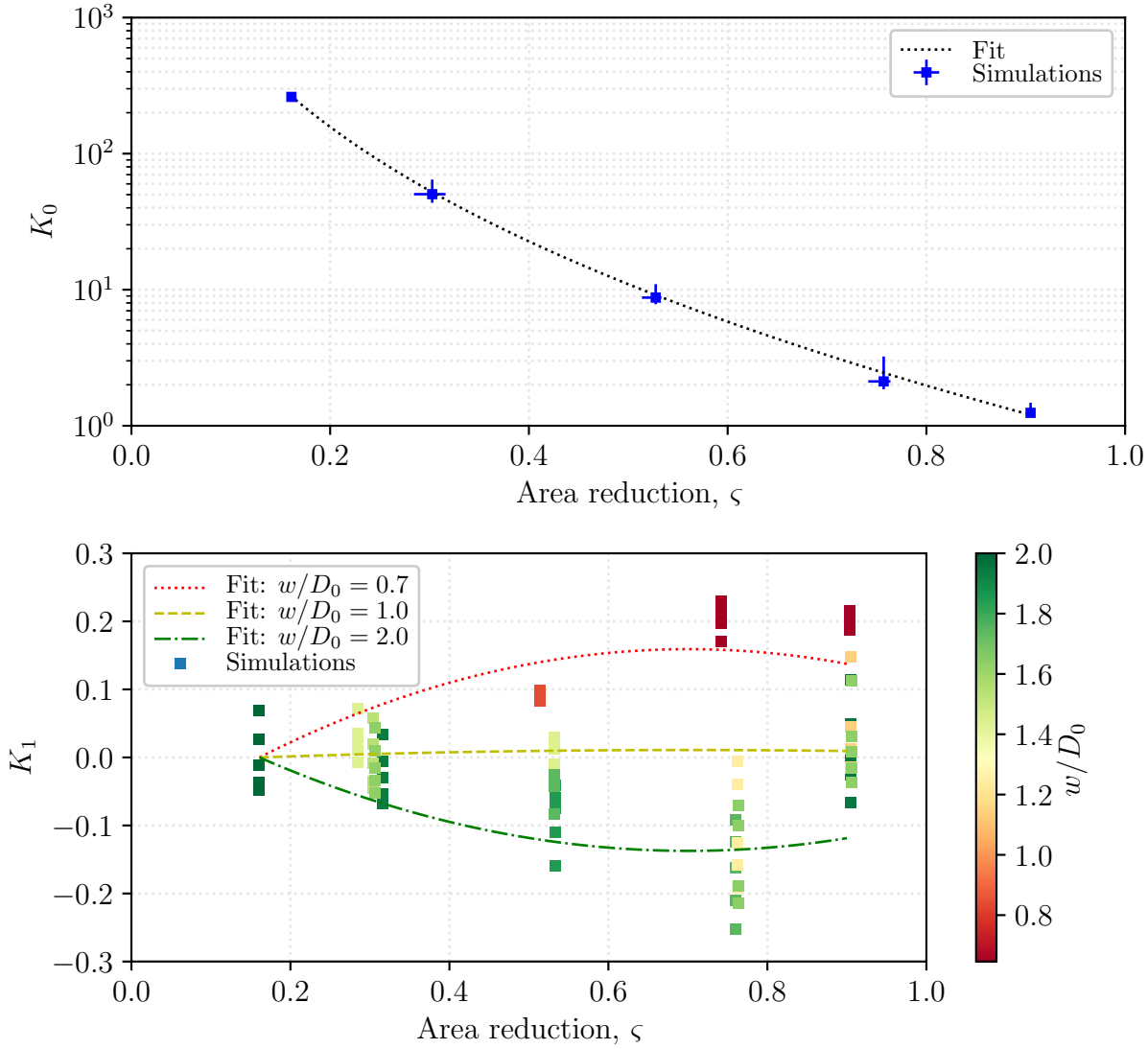

Figure 5.16. Data and least-squares best fits for loss coefficient functions $K_0(\varsigma)$ and $K_1(\varsigma, w/D_0)$ as a primary function of ς. A 95% confidence interval is shown for each value of K_0, and each data point of K_1 is colored by its corresponding value of w/D_0.

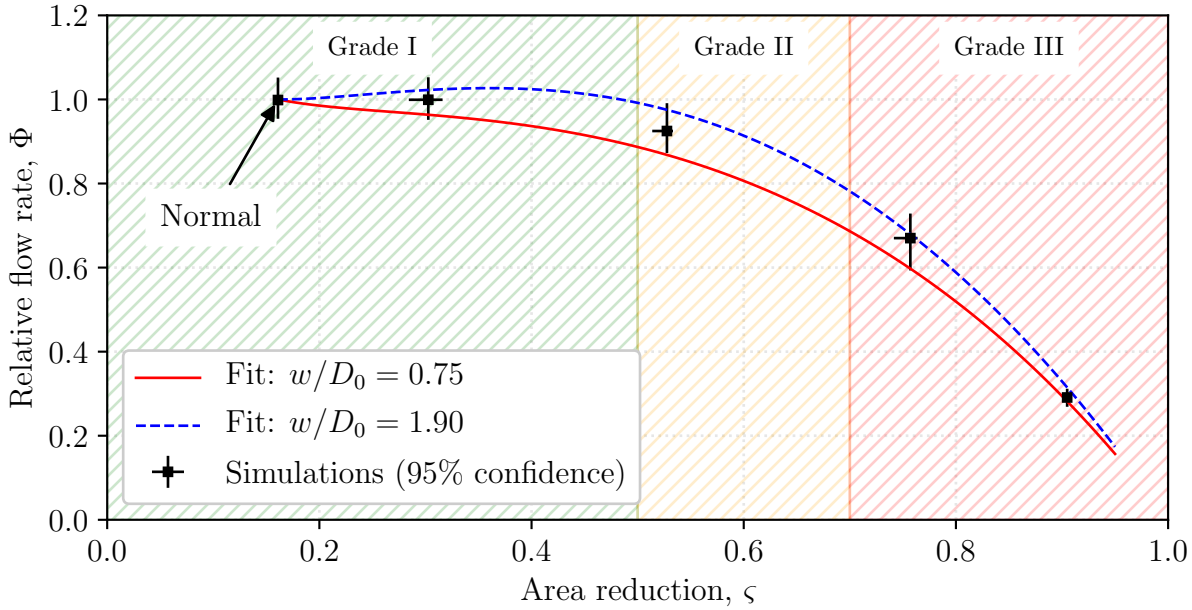

Figure 5.17. Relative flow rate Φ for stenosis area reductions ς, with 95% confidence interval on full data set. Analytical correlations are presented for two stenosis widths $w/D_0 = 0.75$ and $w/D_0 = 1.90$. Myer-Cotton Grades I-III are indicated as three regions of area reduction.

1. Additionally, the data for all widths w/D_0 and Reynolds numbers $\mathrm{Re_D}$ are shown with a 95% confidence interval based on the range of possible values. The error bars extend to values of $\Phi > 1$ in some cases of the simulation data, representing natural variations in flow rates. The best-fit data tend to take values greater than 1 for area reductions of $\varsigma < 0.5$ and $w/D_0 = 1.90$ due to artifacts in the fit. This should not be interpreted as a potential improvement by reducing the area of the trachea. Rather, the qualitative differences between these fits should be considered. As such, it is clear that the relative flow rate Φ is slightly higher for the wider stenosis, although the sensitivity is relatively weak. Thus, the sharper stenosis (with smaller w/D_0) will result in a more severe reduction in flow relative to a normal airway. In both cases, the relative flow rate is above 90% for area reductions up to $\varsigma = 0.5$, where the flow begins to reduce appreciably.

The ranges of relative flow rate Φ for each Myer-Cotton grade are tabulated in Table 5.1. Here, Grade III encompasses relative flow rates between 70% and 0%. Since the

Table 5.1. Ranges of relative flow rate Φ for Myer-Cotton Grades I-III based on best fits for two stenosis widths $w/D_0 = 0.75$ and $w/D_0 = 1.90$.

		Relative flow rate, Φ	
Grade	Area Reduction, ς	$w/D_0 = 0.75$	$w/D_0 = 1.90$
I	$0.0 - 0.5$	$1.000 - 0.887$	$1.000 - 0.992$
II	$0.5 - 0.7$	$0.887 - 0.687$	$0.992 - 0.781$
III	$0.7 - 1.0$	$0.687 - 0.000$	$0.781 - 0.000$

range of Φ is so large for Grade III, more granularity may be prudent in a grading system such that a 75% area reduction with approximately 65% relative flow would be classified differently from a 90% area reduction with approximately 35% relative flow.

5.6. Simulation of a Sinusoidal Inspiration Cycle

An additional simulation was performed in order to examine the validity of the stationary-flow assumption discussed in Section 5.1, as well as the effects of flow instabilities on a representative inspiration cycle. Hence, a stenosis model exhibiting appreciable flow oscillations in the stationary case was used ($\varsigma = 0.76$, $w/D_0 = 1.75$) with a sinusoidal flow profile for one inspiration, with typical inspiration parameters from the statistics in Chapter 1. The flow was initially taken to be at rest, and the simulation spanned the time for one complete inspiration. The corresponding expiration cycle was not simulated. Since the model corresponds to an 11-year-old patient, a maximum flow rate of 260 cm^3/s was used with an inspiration time of 1.5 seconds. The volumetric flow rate $\dot{V}$ and total pressure differential ΔP are shown over the inspiration cycle in Figure 5.18. Here, the relationship between pressure drop and volumetric flow rate for stationary flow is shown for reference.

It is evident from the pressure differential ΔP that the flow instabilities tend to set in for higher flow rates, but they are at a much shorter time scale than that of the inspiration cycle. An abrupt change in pressure was seen at $t = 1.5$ s, since the flow rate was imposed as 0 cm^3/s at that time. An abrupt change in pressure was needed in order to completely decelerate the fluid to prevent it from crossing the boundaries at that time. It is clear from the "phase-space" plot of ΔP versus $\dot{V}$ that only a minor hysteresis was seen over

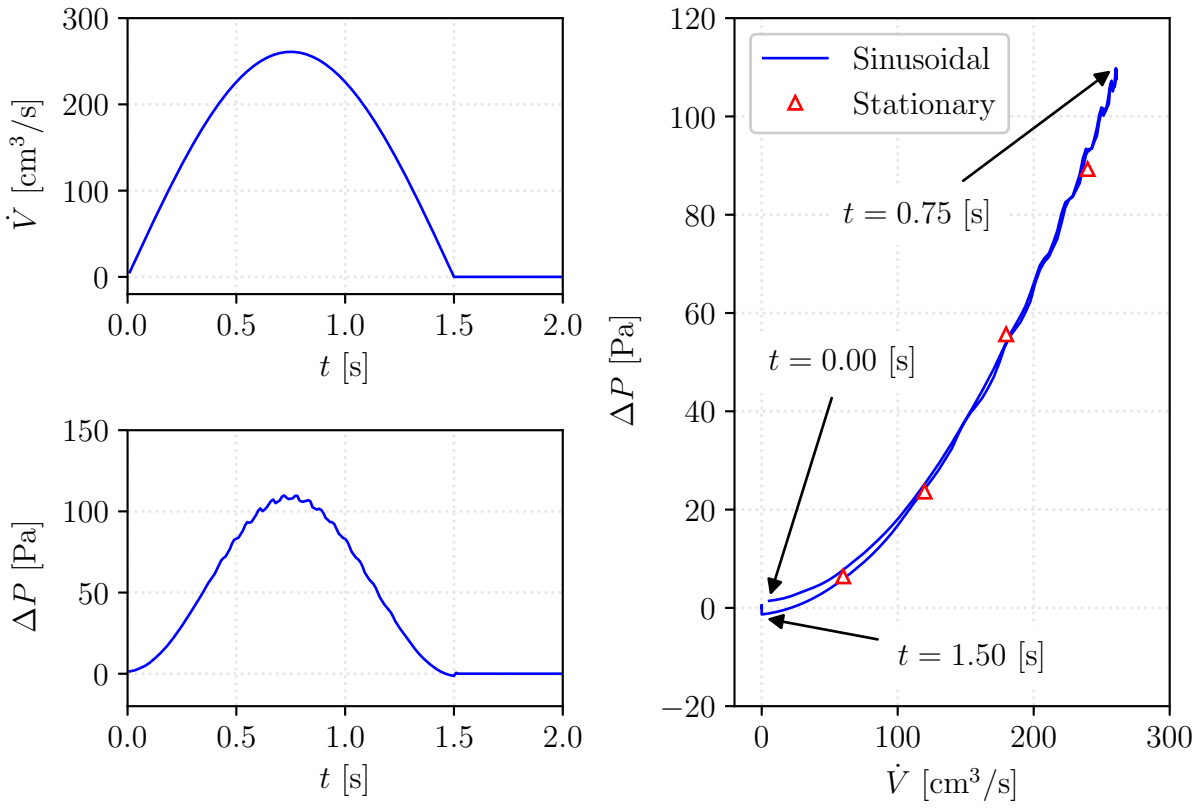

Figure 5.18. Volumetric flow rate $\dot{V}$ and total pressure drop ΔP over time for sinusoidal flow simulation in stenosis model with $\varsigma = 0.76$ and $w/D_0 = 1.75$, with corresponding stationary flow results for comparison.

the inspiration cycle, and the instantaneous flow pressure drop is consistent with that of stationary flow. Thus, the pressure drop at an instant in time is weakly dependent on the time-history of the flow, and the stationary flow approximation holds well.

Figure 5.19 shows the velocity magnitude at regular time intervals on cross-sections of the trachea. Here, it is possible to see some of the oscillations ($0.7\text{s} \leq t \leq 1.0\text{s}$) in the jet regions. The flow structures do not appear to be qualitatively different from those of the stationary-flow simulations.

Additionally, the loss coefficient may be compared to the data from stationary simulations, in addition to the stationary-flow correlation of Eq. (5.14). Figure 5.20 compares the instantaneous loss coefficient to the instantaneous Reynolds number. At low Reynolds numbers – the beginning and end of the simulation – the sinusoidal simulation tends to diverge from the stationary simulations. These differences seem to be large since they are scaled by the square of instantaneous average velocity, which is very low. Dimensionally, they correspond to very small differences in pressure drop ΔP, as shown in Figure 5.18.

At $\text{Re}_\text{D} > 1000$, the loss coefficient for the sinusoidal case is relatively insensitive to Reynolds number and agrees relatively well with the stationary data. A minor discrepancy (approximately 9%) exists between the correlation and the stationary data because widely-applicable correlations tend to produce a systematic bias for specific cases in order to hold true for general cases.

5.7. Discussion

The dimensionless quantities developed in this chapter were used to provide insight into the physics of the airways. Additionally, they can be used to predict the dimensional flow quantities within normal and stenotic airways. Given an airway, the length scales (median hydraulic diameter, stenosis area reduction, stenosis width) can be computed from measurements along the hydraulic diameter. Given a flow rate, the average velocity can be calculated from the median trachea area. From these parameters, each relevant nondimensional quantity can be found from correlations or plots, which can be converted

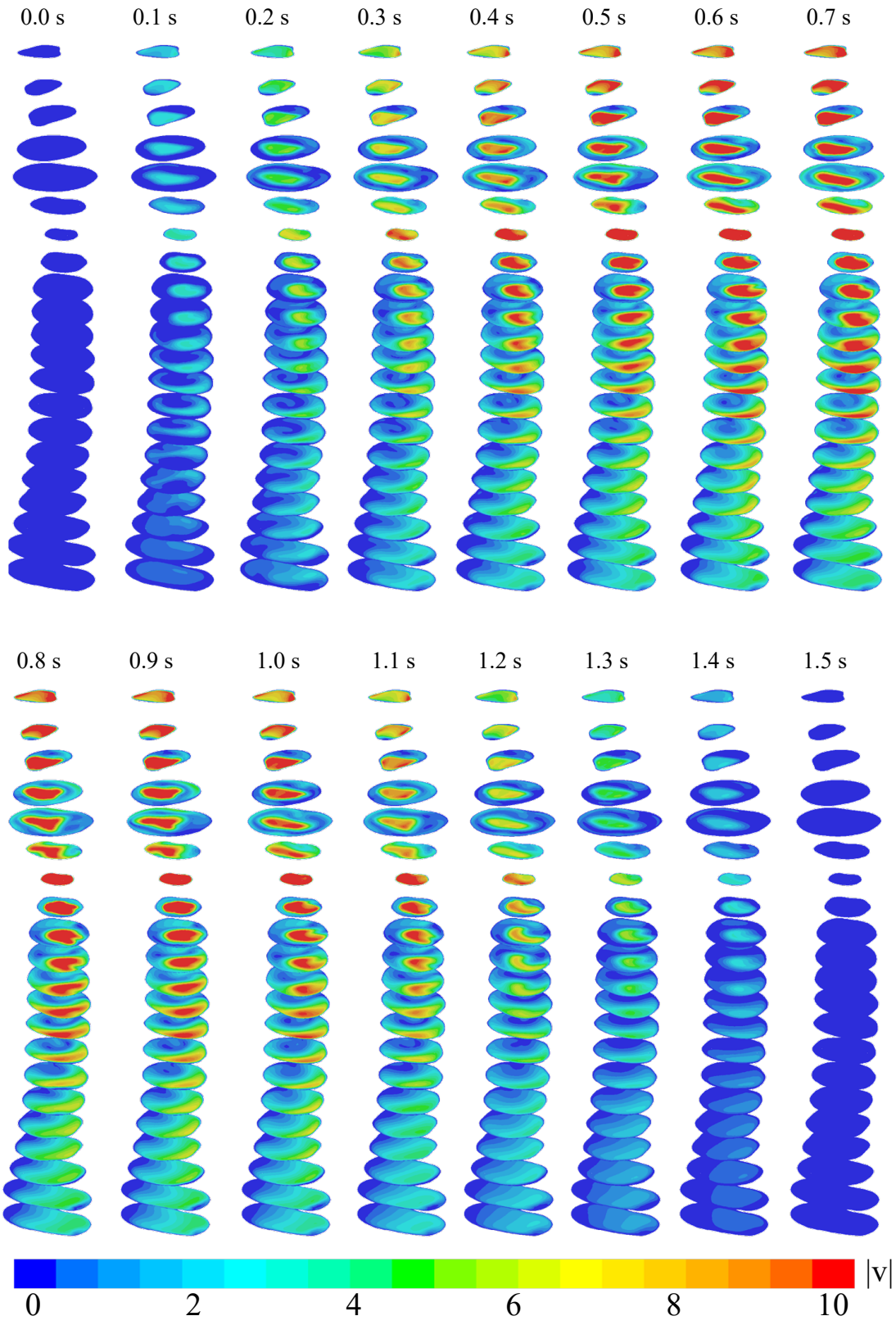

Figure 5.19. Contours of velocity magnitude |v| for stenotic trachea ($\varsigma = 0.76$, $w/D_0 = 1.75$) from simulation of sinusoidal inspiration.

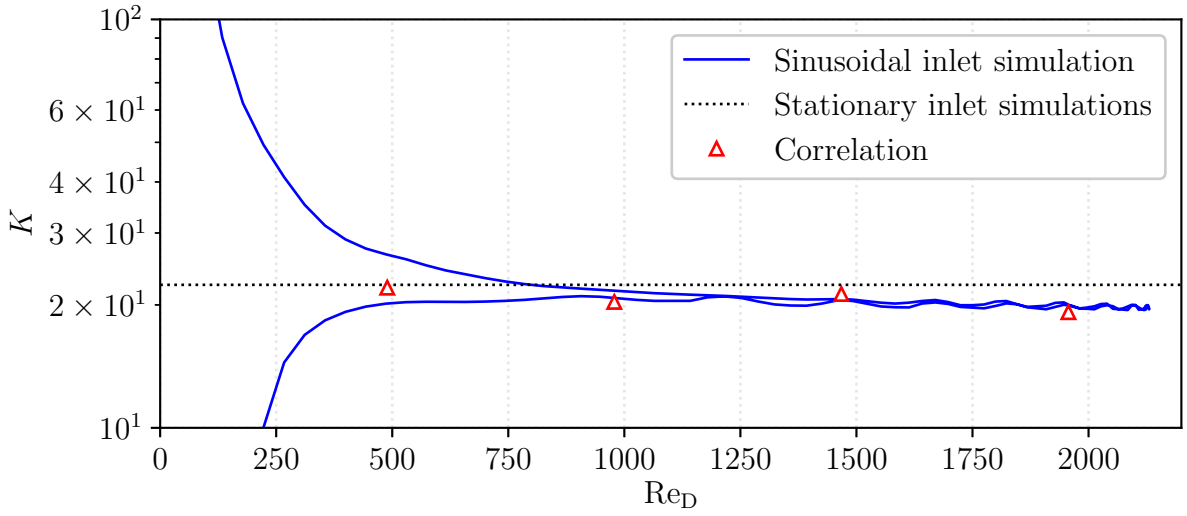

Figure 5.20. Relationship between instantaneous loss coefficient K and instantaneous Reynolds number $\mathrm{Re_D}$ for sinusoidal inflow simulation, compared to the data of the stationary inflow simulation and the stationary inflow correlation of Eq. (5.14).

to the relevant dimensional parameter such as pressure differential, shear stress, or wall normal stress.

It should be noted that for the results discussed in Section 5.5, each simulation on a truncated domain was performed with an inflow condition imposed with velocity normal to the surface, and a power-law velocity profile according to Eq. (5.11). Such domain truncation exposes the results to potential sensitivities in the orientation of the inlet boundary. An additional study of the parametric sensitivity to variations in the inflow direction and potential flow bias is described in Appendix B. The trends are qualitatively identical to those of the current chapter; however, it is also shown that sensitivity to inlet conditions is attenuated for more severe stenosis conditions – that is, higher area reductions ς.

It was demonstrated anecdotally in Section 5.6 that the flow with a variable inlet flow rate is similar to that of a stationary inlet flow. For a stenosis with 76% area reduction and a sinusoidal inspiration profile, a minor hysteresis was found in the relationship between Reynolds number and loss coefficient at low Reynolds numbers. This result corroborates the assumption that the characteristics of inspiratory flow are well-represented by station-

ary flow. It should be noted; however, that the results presented in this chapter do not necessarily hold for expiratory flow. It is hypothesized that the flow structures should be similar; however, the regions of recirculation and flow separation will be completely different. The aerodynamic effects of stenosis on the expiratory cycle may indeed be different from those of the inspiratory cycle.

It should be noted also that the aerodynamic indicators proposed in this chapter are not unique. Rather than taking the maximum perimeter-averaged skin friction coefficient or the minimum perimeter-averaged pressure coefficient, it is possible to consider some integrated or averaged value of these coefficients such as the RMS, or, more generally, a p-norm. The p-norm $||f||_p$ of a function $f(x)$ over the domain $0 \leq x \leq L$ is defined as

$$||f||_p = \left[\frac{1}{L}\int_0^L |f(x)|^p \, dx\right]^{1/p} \tag{5.19}$$

For the p-norm, $p = 2$ recovers the RMS value and $p \to \infty$ recovers the maximum value of $f(x)/L$ on the domain $0 \leq x \leq L$. Completely different aerodynamic functions may also be used. For example, the skin friction coefficient may be decomposed into the shear in the forward direction and shear in the reversed direction, providing an indication of the shear reversal regions. The vortex content of the flow may be measured by one of many aerodynamic quantities such as the vorticity, the helicity, the Q criterion, or the λ_2 criterion [16]; however, a direct connection between vortex content and clinical symptoms is not clear to the author.

Chapter 6
Conclusions & Future Work

In this study, a rigorous methodology has been established for quantifying the aerodynamics of laryngotracheal stenosis. In Chapter 2, a method was described for generating geometric models for analysis from CT scans. In Chapter 3, a wavelet-based method was introduced to provide an objective method of measuring the anatomical length scales associated with the stenosis. In Chapter 4, the stenotic tube model was used as a basis for validating the turbulence model and determining an adequate mesh size. In Chapter 5, simulations were performed on a real airway model with virtually-introduced stenosis in order to quantify the aerodynamic performance with respect to anatomical variations. The correlations developed for aerodynamic performance indicate that the stenosis produces a small aerodynamic effect for area reductions less than 50% relative to the normal airway. This result agrees well with the conclusion of Brouns et al. [7], who concluded that 40% area reductions have a negligible effect on breathing as compared to constrictions greater than 70%. Such a stenosis would conventionally be classified on the Myer-Cotton scale as "Grade I", where it is unlikely that surgery would be ordered. Ranging from area reductions of 50% to 70%, the Myer-Cotton Grade II region contains the beginning of a precipitous decrease in flow, decrease in minimum wall pressure, and increase in maximum shear stress. These appreciable changes in the aerodynamics continue into the Myer-Cotton Grade III region, where there is more than 70% reduction in area. At an area reduction of 90%, the maximum wall shear stresses can measure up to 12 times the maximum wall shear stresses of a normal airway. Likewise, the wall suction pressures can reach values up to 60 times the suction pressures experienced by a normal airway.

Additionally, the flow rate ratio Φ shown in Figure 5.17 and Table 5.1 may be used by surgeons to characterize the sensitivities of the relative flow rate with respect to area reduction. For example, if a surgeon estimates that they can surgically improve a 70% area reduction to a 40% area reduction with a stenosis width of $w/D_0 = 0.65$, this represents

an improvement of $\Phi = 0.69$ to $\Phi = 0.95$, or a 38% increase in flow. This is relative to the maximum possible increase in flow of 45%. Therefore, the surgeon would expect that such an improvement in the anatomy would be physiologically meaningful, even though it does not represent a full anatomical removal of the obstruction.

6.1. Future Computational Studies

In the present study, many assumptions were made in order to simplify the analysis to an appropriate scope. The most obvious extension to the present work is to sequentially remove model assumptions and add complexity:

(i) Eliminate the stationary-flow assumption, simulating flows with transient boundary conditions to mimic the actual transient breathing phenomena.

(ii) Model the interactions between the aerodynamic forces and structural mechanics of the trachea (fluid-structure interaction models).

(iii) Model the effects of mucous lining and mucociliary transport on the trachea walls.

(iv) Implement more high-fidelity turbulence models such as Reynolds Stress Models (RSM) or Large-Eddy Simulations (LES). A Direct Numerical Simulation (DNS) study may also be useful for validating these turbulence models.

It would also be prudent to design a standardized, semi-idealized geometric model of the airway in a CAD software using fully-parameterized surfaces for future simulations, similarly to the work of Brouns [7]. The use of a "clean" geometry created in software would allow a higher-quality mesh to be generated – perhaps even a structured mesh – which is necessary when using more complex turbulence models such as LES. Additionally, a fully-parameterized model would be more easily manipulable to simulate specific anatomical manifestations of diseases such as stenosis.

The present study considered only a single airway model, which was deemed to be reasonably representative of the population (i.e. not obviously abnormal). A natural extension of the present study would be to analyze the trachea models of many samples of the population, and incorporate the statistical differences into the correlations developed

here. This type of statistical extension would be particularly important in establishing the uncertainty associated with the definition of a "normal" airway. Additionally, there may be some natural variations in normal airways which may tend to amplify the aerodynamic effects associated with the stenosis.

Furthermore, the present study considered only a single type of stenosis, generated to be quasi-axisymmetric with respect to the rest of the trachea. In reality, laryngotracheal stenosis may be classified into several different morphologies [24], and it is possible for multiple stenosis regions to exist. Each different morphology of stenosis is expected to have different aerodynamic behavior, and geometric similarity may not be invoked between two stenosis conditions of different morphology. Thus, it would be prudent to perform simulations to characterize the aerodynamic variations of the various stenosis morphologies. A recommended first step would be investigate the differences between a stenosis approximately centered in the airway and a stenosis protruding from one side of the airway, as first investigated in an idealized model by Young & Tsai [47].

Since the present study only analyzed stenosis models which were artificially introduced into normal trachea, it is recommended to analyze the air flows in various trachea models which have been diagnosed as stenotic. Since it is rare for medical imaging to be ordered for stenosis patients, it is difficult to find relevant data; however, the analysis of real stenotic airways would be impactful to validate the methods of artificially simulating stenosis.

6.2. Future Experimental and Clinical Studies

Rather than performing additional computational studies, perhaps the most immediately valuable future work would be to supplement the present computational study with experimental validation. Since the present study represents a minimal physical complexity, it would be prudent to validate the simple physical model before adding more complex models to the simulations. The velocity field could be validated by using particle-image-velocimetry (PIV) methods, as used previously by Taherian [34], or by instrumenting the physical model of the airway with flow meters and pressure transducers as used previously

by Mylavarapu [28].

The present study proposed a connection between specific aerodynamic indicators (loss coefficient, skin friction coefficient, and pressure coefficient) and clinical airway symptoms associated with stenosis (dyspnea, airway infection, and airway collapse) based on physiological insight. In order to fully validate the connection between aerodynamics and clinical symptoms, an in-depth set of clinical trials is necessary. In general, in-situ measurement of airway flows is difficult [41], so a proposed method would be to take CT scans of the airways of symptomatic patients, complete a CFD analysis on the airways, and examine their non-dimensional aerodynamic indicators relative to those of normal airways. By establishing a strong correlation between abnormal aerodynamic indicators and the corresponding symptoms of the patients, the proposed aerodynamic indicators could be considered validated.

6.3. Toward Medical Software and Patient Impact

A natural end goal for this research into the aerodynamics of laryngotracheal stenosis is toward the development of medical software applications. It is envisioned that an otolaryngologist would be able to order a CT scan of a patient's trachea; from the CT scan, the software would be able to instantly predict a set of performance parameters by using correlations between aerodynamics and anatomical measurements. Then, any variation on the original geometry would correspond to a different set of aerodynamic performance parameters. If it were known how each surgical decision would affect the trachea geometry, then an optimal set of surgical decisions could be generated by optimizing the aerodynamic performance subject to the surgical parameters. This optimization algorithm would be available to the surgeon within the context of a simple graphical user application (GUI). With the use of comprehensive aerodynamic correlations, the need for patient-specific CFD is bypassed, allowing surgeons to make decisions within minutes rather than days or weeks. The aerodynamic correlations used in surgery optimization could be provided by a web-service, where they are continuously updated as more data becomes available.

The potential impact of this type of medical software would be immense for patients

with laryngotracheal stenosis. If surgeons can quickly make informed, physics-based decisions, the lives of stenosis patients as well as their families can be drastically improved.

References

[1] Addison, P. *The illustrated wavelet transform handbook: introductory theory and applications in science, engineering, medicine and finance*. CRC Press, Taylor & Francis Group, Boca Raton, FL, 2016.

[2] Ahmed, S. A., and Giddens, D. P. Velocity measurements in steady flow through axisymmetric stenoses at moderate Reynolds numbers. *J. Biomech 16*, 7 (1983), 505–16.

[3] Akay, M. Wavelet applications in medicine. *IEEE Spectrum*, May (1997), 50–56.

[4] ANSYS. ANSYS Fluent Theory Guide, 2016.

[5] ANSYS. ANSYS Fluent User's Guide, 2016.

[6] Benjamin, B., and Holinger, L. D. Laryngeal complications of endotracheal intubation. *Annals of Otology, Rhinology & Laryngology 117*, 9_suppl (2008), 2–20.

[7] Brouns, M., Jayaraju, S. T., Lacor, C., Mey, J. D., Noppen, M., Vincken, W., Verbanck, S., and De Mey, J. Tracheal stenosis: a flow dynamics study. *Journal of Applied Physiology 102*, 3 (2007), 1178–1184.

[8] Burrus, C. S., Gopinath, R. A., and Guo, H. *Introduction to Wavelets and Wavelet Transforms: A Primer*. Pearson, 1997.

[9] Fleming, S., Thompson, M., Stevens, R., Heneghan, C., Plüddemann, A., MacOnochie, I., Tarassenko, L., and Mant, D. Normal ranges of heart rate and respiratory rate in children from birth to 18 years of age: A systematic review of observational studies. *The Lancet 377*, 9770 (2011), 1011–1018.

[10] Griscom, N. T., and Wohl, M. E. B. Dimensions of the growing trachea related to age and gender. *American Journal of Roentgenology 146*, 2 (1986), 233–237.

[11] Hirsch, C. *Numerical Computation of Internal and External Flows: The Fundamentals of Computational Fluid Dynamics*. Butterworth-Heinemann, 2007.

[12] Jahangiri, M., Saghafian, M., and Sadeghi, M. R. Numerical study of turbulent pulsatile blood flow through stenosed artery using fluid-solid interaction. *Computational and Mathematical Methods in Medicine 2015* (2015).

[13] Jayaraju, S. T., Brouns, M., Lacor, C., Belkassem, B., and Verbanck, S. Large eddy and detached eddy simulations of fluid flow and particle deposition in a human mouth-throat. *Journal of Aerosol Science 39*, 10 (2008), 862–875.

[14] Jayaraju, S. T., Brouns, M., Lacor, C., Mey, J. D., and Verbanck, S. Effects of tracheal stenosis on flow dynamics in upper human airways. *European Conference on Computational Fluid Dynamics* (2006), 1–16.

[15] Jeong, S. J., Kim, W. S., and Sung, S. J. Numerical investigation on the flow characteristics and aerodynamic force of the upper airway of patient with obstructive sleep apnea using computational fluid dynamics. *Med Eng Phys 29*, 6 (2007), 637–651.

[16] Jiang, M., Machiraju, R., and Thompson, D. Detection and visualization of vortices. In *Visualization Handbook*. 2005, pp. 295–309.

[17] Koeppen, B. M., and Stanton, B. A. *Berne & Levy Physiology*. Elsevier, 2017.

[18] Kundu, P. *Fluid Mechanics*. Academic Press Elsevier, London, 2016.

[19] Merrill, E. W., and Pelletier, G. a. Viscosity of human blood: transition from Newtonian to non-Newtonian. *Journal of applied physiology (Bethesda, Md. : 1985) 23*, 2 (1967), 178–182.

[20] Mihaescu, M., Murugappan, S., Kalra, M., Khosla, S., and Gutmark, E. Large Eddy simulation and Reynolds-Averaged Navier-Stokes modeling of flow in a realistic pharyngeal airway model: An investigation of obstructive sleep apnea. *Journal of Biomechanics 41*, 10 (2008), 2279–2288.

[21] Mihaescu, M., Mylavarapu, G., Gutmark, E. J., and Powell, N. B. Large Eddy Simulation of the pharyngeal airflow associated with Obstructive Sleep Apnea Syndrome at pre and post-surgical treatment. *Journal of Biomechanics 44*, 12 (2011), 2221–2228.

[22] Molla, M., and Paul, M. LES of physiological pulsatile flow in a model arterial stenosis. In *4th BSME - ASME International Conference on Thermal Engineering, 27-29 December 2008, Dhaka, Bangladesh* (2008), pp. 27–29.

[23] Monnier, P. *Pediatric airway surgery management of laryngotracheal stenosis in infants and children*. Springer, 2011.

[24] Murgu, S., and Miller, R. Evaluation and Classifications of Laryngotracheal Stenosis. *Revista Americana de Medicina Respiratoria RAMR 144*, 4 (2014), 344–357.

[25] Murgu, S. D., and Colt, H. G. Tracheobronchomalacia and excessive dynamic airway collapse. *Respirology 11*, 4 (2006), 388–406.

[26] Myer, C. M., O'connor, D. M., and Cotton, R. T. Proposed grading system for subglottic stenosis based on endotracheal tube sizes. *Annals of Otology, Rhinology & Laryngology 103*, 4 (1994), 319–323.

[27] Mylavarapu, G., Mihaescu, M., Fuchs, L., Papatziamos, G., and Gutmark, E. Planning human upper airway surgery using computational fluid dynamics. *Journal of Biomechanics 46*, 12 (2013), 1979–1986.

[28] Mylavarapu, G., Murugappan, S., Mihaescu, M., Kalra, M., Khosla, S., and Gutmark, E. Validation of computational fluid dynamics methodology used for human upper airway flow simulations. *Journal of Biomechanics 42*, 10 (2009), 1553–1559.

[29] Pope, S. B. *Turbulent Flows*. Cambridge University Press, Cambridge New York, 2000.

[30] Rimensberger, P. *Pediatric and Neonatal Mechanical Ventilation: From Basics to Clinical Practice*. Springer, 2014.

[31] Schlichting, H., and Gersten, K. *Boundary-Layer Theory*. Springer, 2000.

[32] Sherwin, S. J., and Blackburn, H. M. Three-dimensional instabilities of steady and pulsatile axisymmetric stenotic flows. *Journal of Fluid Mechanics 533*, August (2005), 297–327.

[33] Tagliasacchi, A., Delame, T., Spagnuolo, M., Amenta, N., and Telea, A. 3D skeletons: A state-of-the-art report. *Computer Graphics Forum 35*, 2 (2016), 573–597.

[34] Taherian, S., Rahai, H., Bonifacio, J., Lopez, S., and Waddington, T. Computational Fluid Dynamics Validation of the Upper Respiratory System. *Proceedings of the ASME 2017 International Mechanical Engineering Congress and Exposition* (2017), 1–7.

[35] Taherian, S., Rahai, H., Gomez, B., Waddington, T., and Mazdisnian, F. Computational fluid dynamics evaluation of excessive dynamic airway collapse. *Clinical Biomechanics 50*, October (2017), 145–153.

[36] Taherian, S., Rahai, H., Gomez, B. Z., Waddington, T., and Bonifacio, J. R. Tracheal stenosis: A CFD approach for evaluation of drug delivery. In *Volume 3: Biomedical and Biotechnology Engineering* (nov 2015), ASME.

[37] Tilley, A. E., Walters, M. S., Shaykhiev, R., and Crystal, R. G. Cilia Dysfunction in Lung Disease. *Annual Review of Physiology 77*, 1 (feb 2015), 379–406.

[38] van Ertbruggen, C., Hirsch, C., and Paiva, M. Anatomically based three-dimensional model of airways to simulate flow and particle transport using computational fluid dynamics. *J. Appl. Physiol. 98*, 3 (2005), 970–980.

[39] Varghese, S. S., Frankel, S. H., and Fischer, P. F. Direct numerical simulation of stenotic flows, Part 1: Steady flow. *Journal of Fluid Mechanics 582*, 2007 (jul 2007), 253.

[40] Varghese, S. S., Frankel, S. H., and Fischer, P. F. Direct numerical simulation of stenotic flows, Part 2: Pulsatile flow. *Journal of Fluid Mechanics 582*, 2007 (2007), 281.

[41] Wassermann, K., Koch, A., Warschokow, A., and Mathen, F. Measuring in Situ Central Airway Resistance in Patients With Laryngotracheal Stenosis. *The Laryngoscope 109*, September (1999), 1516–1520.

[42] Wikipedia contributors. Respiratory tract — Wikipedia, the free encyclopedia, 2018. [Online; accessed 23-August-2018].

[43] Womersley, J. R. Method for the calculation of velocity, rate of flow and viscous drag in arteries when the pressure gradient is known. *The Journal of Physiology 127*, 3 (1955), 553–563.

[44] World Health Organization. *WHO Child Growth Standards: Length/Height-for-age, Weight-for-age, Weight-for-length, Weight-for-height, and Body Mass Index-for age*. World Health Organization, 2006.

[45] Young, D. F., and Morgan, B. E. An Integral Method for the Analysis of Flow in Analysis Stenoses. *Bulletin of Mathematical Biology 36* (1974).

[46] Young, D. F., and Tsai, F. Y. Flow characteristics in models of arterial stenoses - II. Unsteady flow. *Journal of Biomechanics 6*, 5 (jul 1973), 547–559.

[47] Young, D. F., and Tsai, F. Y. Flow characteristics in models of arterial stenoses I. Steady flow. *Journal of Biomechanics 6*, 4 (jul 1973), 395–410.

[48] Zendehbudi, G. R., and Moayeri, M. S. Comparison of physiological and simple pulsatile flows through stenosed arteries. *Journal of Biomechanics 32*, 9 (1999), 959–965.

Appendix A
Turbulence Model

Using the eddy viscosity hypothesis, the incompressible RANS equations are expressed in tensor notation as

$$\frac{\partial U_i}{\partial t} + U_j \frac{\partial U_i}{\partial x_j} = -\frac{1}{\rho}\frac{\partial P}{\partial x_i} + \frac{\partial}{\partial x_j}\left[(\nu + \nu_t)\left(\frac{\partial U_i}{\partial x_j} + \frac{\partial U_j}{\partial x_i}\right) - \frac{2}{3}k\delta_{ij}\right] \tag{A.1}$$

where U_i (with $i = 1, 2, 3$) is the mean-flow velocity, P is the mean-flow pressure, k is the turbulence kinetic energy, and ν_t is the eddy viscosity, which is an isotropic approximation of the Reynolds stresses.

The turbulence model used extensively in the simulations presented in this document is the k-ω SST model. The k-ω SST model is recommended for complex boundary layer flows under adverse pressure gradient and separation. It was developed out of the observation that the standard k-ω model tends to more accurately predict boundary layers but is highly sensitive to turbulence boundary conditions, while the standard k-ε model tends to be insensitive to boundary conditions and gives less-accurate near-wall solutions. The k-ω SST blends the standard k-ε and standard k-ω models in order to use the best parts of both models, providing accurate boundary layer predictions and low sensitivity to the turbulence boundary conditions.

A.1. Transport Equations

In the k-ω SST model [4], the k and ω model equations are given in tensor notation as

$$\frac{\partial k}{\partial t} + U_i \frac{\partial k}{\partial x_i} = \frac{\partial}{\partial x_j}\left[\left(\nu + \frac{\nu_t}{\sigma_k}\right)\frac{\partial k}{\partial x_j}\right] + G_k - Y_k \tag{A.2}$$

$$\frac{\partial \omega}{\partial t} + U_i \frac{\partial \omega}{\partial x_i} = \frac{\partial}{\partial x_j}\left[\left(\nu + \frac{\nu_t}{\sigma_\omega}\right)\frac{\partial \omega}{\partial x_j}\right] + G_\omega - Y_\omega + D_\omega \tag{A.3}$$

where ν_t is the turbulent eddy viscosity defined in Eq. (A.19), G_k and G_ω represent the production of k and ω, Y_k and Y_ω represent the dissipation of k and ω due to turbulence,

and D_ω represents the cross-diffusion term. Note here that the subscripts k and ω do not refer to tensor indices. The diffusion modifiers σ_k and σ_ω are defined as

$$\frac{1}{\sigma_k} = \frac{F_1}{\sigma_{k,1}} + \frac{1 - F_1}{\sigma_{k,2}}, \qquad \frac{1}{\sigma_\omega} = \frac{F_1}{\sigma_{\omega,1}} + \frac{1 - F_1}{\sigma_{\omega,2}} \tag{A.4}$$

where the blending function F_1 is given by

$$F_1 = \tanh\left(\Phi_1^4\right) \tag{A.5}$$

$$\Phi_1 = \min\left[\max\left(\frac{\sqrt{k}}{0.09\omega y}, \frac{500\nu}{y^2\omega}\right), \frac{4\rho k}{\sigma_{\omega,2} D_\omega^+ y^2}\right], \qquad D_\omega^+ = \max\left[\frac{2\rho}{\sigma_{\omega,2}\omega}\frac{\partial k}{\partial x_j}\frac{\partial \omega}{\partial x_j}, 10^{-10}\right] \tag{A.6}$$

where y is the distance to the next surface; D_ω^+ is the positive portion of the cross-diffusion term D_ω in Eq. (A.3); and $\sigma_{k,1}$, $\sigma_{k,2}$, $\sigma_{\omega,1}$, and $\sigma_{\omega,2}$ are model constants given in Table A.1.

A.2. Production Terms

The term G_k in Eq. (A.2) represents the production of turbulence kinetic energy k. From an exact derivation of the transport equation of k, this is defined as

$$G_k = -\overline{u_i' u_i'}\frac{\partial u_j}{\partial x_i} \tag{A.7}$$

The Boussinesq hypothesis yields an expression for G_k in terms of the rate of strain tensor:

$$G_k = \nu_t S^2 \tag{A.8}$$

where S is the modulus of the rate-of-strain tensor S_{ij}:

$$S \equiv \sqrt{2 S_{ij} S_{ij}}, \qquad S_{ij} \equiv \frac{1}{2}\left(\frac{\partial U_i}{\partial x_j} + \frac{\partial U_j}{\partial x_i}\right) \tag{A.9}$$

The term G_ω in Eq. (A.3) represents the production of ω and is given by

$$G_\omega = \frac{\alpha\alpha^*}{\nu_t} G_k \tag{A.10}$$

where α and α^* are "switched" between experimentally fit values by the relations:

$$\alpha = \frac{\alpha_\infty}{\alpha^*} \left(\frac{\alpha_0 + \mathrm{Re}_t/R_\omega}{1 + \mathrm{Re}_t/R_\omega} \right) \tag{A.11}$$

$$\alpha^* = \alpha^*_\infty \left(\frac{\beta_i/3 + \mathrm{Re}_t/R_k}{1 + \mathrm{Re}_t/R_k} \right) \tag{A.12}$$

$$\alpha_\infty = F_1 \left(\frac{\beta_{i,1}}{\beta^*_\infty} - \frac{\kappa^2}{\sigma_{\omega,1}\sqrt{\beta^*_\infty}} \right) + (1 - F_1) \left(\frac{\beta_{i,2}}{\beta^*_\infty} - \frac{\kappa^2}{\sigma_{\omega,2}\sqrt{\beta^*_\infty}} \right) \tag{A.13}$$

$$\beta_i = F_1 \beta_{i,1} + (1 - F_1)\, \beta_{i,2} \tag{A.14}$$

where F_1 is a blending function defined in Eq. (A.5); and R_k, R_ω, α_0, α^*_∞, $\beta_{i,1}$, $\beta_{i,2}$, β^*_∞, κ, $\sigma_{\omega,1}$, and $\sigma_{\omega,2}$ are model constants given in Table A.1. The turbulent Reynolds number Re_t is defined as

$$\mathrm{Re}_t = \frac{k}{\nu\omega} \tag{A.15}$$

A.3. Dissipation Terms

The term Y_k and Y_ω in Eq. (A.2) and (A.3) represent the dissipation rates of k and ω, and are expressed for an incompressible flow as

$$Y_k = \beta^* k\omega, \qquad\qquad Y_\omega = \beta_i \omega^2 \tag{A.16}$$

where for an incompressible flow,

$$\beta^* = \beta^*_\infty \left(\frac{4/15 + (\mathrm{Re}_t/R_\beta)^4}{1 + (\mathrm{Re}_t/R_\beta)^4} \right) \tag{A.17}$$

where β_i is defined in Eq. (A.14), Re_t is defined in Eq. (A.15), and R_β and β^*_∞ are model constants given in Table A.1.

A.4. Cross-Diffusion Term

The k-ω SST is based on both the standard k-ω and the standard k-ε models, using k-ω near walls and k-ε far from walls. In order to blend them together, the k-ε model has been transformed into equations based on k and ω, which differ from the standard k-ω equations by a single term – the cross-diffusion term D_ω in Eq. (A.3), defined as

$$D_\omega = (1 - F_1) \frac{2}{\sigma_{\omega,2}\omega} \frac{\partial k}{\partial x_j} \frac{\partial \omega}{\partial x_j} \tag{A.18}$$

where F_1 is defined in Eq. (A.5) in order to "switch" to k-ω near walls and to k-ε far from walls. The eddy viscosity ν_t is calculated as

$$\nu_t = \frac{1}{\max\left[\frac{1}{\alpha^*}, \frac{F_2 S}{a_1 \omega}\right]} \frac{k}{\omega} \tag{A.19}$$

where S is the strain rate magnitude defined in Eq. (A.9), a^* is given in Eq. (A.12), and a_1 is a model constant given in Table A.1. The blending function F_2 is given by

$$F_2 = \tanh\left(\Phi_2^2\right), \qquad \Phi_2 = \max\left[\frac{2\sqrt{k}}{0.09\omega y}, \frac{500\nu}{y^2\omega}\right] \tag{A.20}$$

where y is the nearest distance to a surface.

A.5. Model Constants

All of the model constants used by Fluent [4] in the k-ω SST turbulence model are given in Table A.1.

Table A.1. k-ω SST turbulence model constants [4].

Constant	Value	Constant	Value
$\sigma_{k,1}$	1.176	α^*_∞	1
$\sigma_{k,2}$	1.0	$\beta_{i,1}$	0.075
$\sigma_{\omega,1}$	2.0	$\beta_{i,2}$	0.0828
$\sigma_{\omega,2}$	1.168	β^*_∞	0.09
R_k	6	κ	0.41
R_ω	2.95	R_β	8
α_0	1/9	a_1	0.31
α^*_0	0.024		

Appendix B
Parametric Sensitivity to Inflow Boundary

In Section 5.4, a power-law velocity profile was applied to the inlet boundary of the truncated domain in order to obtain flow correlations. It is important also to understand the possible variation in aerodynamics which may be lost in the domain truncation. Thus, we consider several variations of (a) biasing of the inlet flow and (b) the direction of the inlet flow and are considered. By parameterizing the inflow bias and directivity, it is possible to capture effects which are not present in the full model – for example, the effects of tilting the head while breathing. In order to capture this head-tilting effect with a full domain, it would be necessary to generate multiple models, each representing a different patient posture. It is much simpler to prescribe a boundary condition on a truncated domain than to generate multiple models. Additionally, it should be noted that the precise orientation of the inlet plane to the truncated domain is non-unique. The sensitivity of the results to the inlet boundary orientation should be captured by varying the direction of the flow relative to the inlet boundary.

From the results presented in Section 5.3, it was found that the turbulence intensity and eddy viscosity ratio at the glottis are insensitive to the upstream conditions. Since it is unlikely that posture will appreciably influence the turbulence conditions in a normal situation, the turbulence quantities are prescribed according to Equations (5.9) and (5.10).

B.1. Biased Inlet Flow Distribution

In order to specify a velocity profile, a set of axes is defined at the area-center of the inlet boundary, aligned with arbitrarily-defined directions, as illustrated in the left panel of Figure B.1. Firstly, a base velocity profile is assigned to the cross-sectional area based on the distance to the nearest wall y as

$$\frac{v}{v_{\max}} = 1 - \left(1 - \frac{y}{y_{\max}}\right)^n \tag{B.1}$$

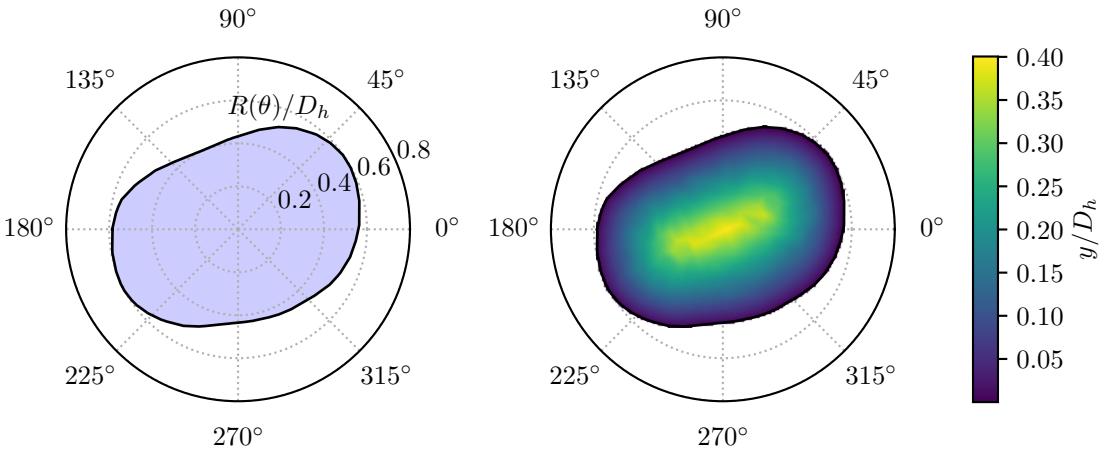

Figure B.1. Inlet boundary plane (left) with the outer radius function $R(\theta)$, scaled by the hydraulic diameter, and (right) dimensionless wall distance y/D_h plotted on the inlet boundary.

where $v_{\max}$ is the maximum velocity, $y_{\max}$ is the maximum distance from the wall (shown in the right panel of Figure B.1), and n is a profile parameter. Taking $n = 2$ is equivalent to a laminar flow for a circular cross-section, while higher values of n give more blunt velocity profiles characteristic of turbulent flows and flows with strongly favorable pressure gradients (e.g. converging sections). It was found by comparing the simulation results of the full airway to this model that $n = 8$ provides the most representative velocity gradients.

In order to create a bias on the base velocity profile, it is prudent to map the inlet boundary to a circular area. Knowing the outer radius R as a function of the angle about the center, $R = R(\theta)$, it is then possible to map each point on the surface to an equivalent circular cross-section by scaling each radial coordinate r by $R(\theta)$. Then, the coordinates of the mapped inlet boundary may be expressed in Cartesian form (x^*, y^*) in terms of the original polar coordinates (r, θ) as

$$x^* = \frac{r}{R(\theta)}\cos(\theta), \qquad y^* = \frac{r}{R(\theta)}\sin(\theta) \tag{B.2}$$

Then, the Gaussian bias G is centered at a location (x_c^*, y_c^*) and parameterized by a radius

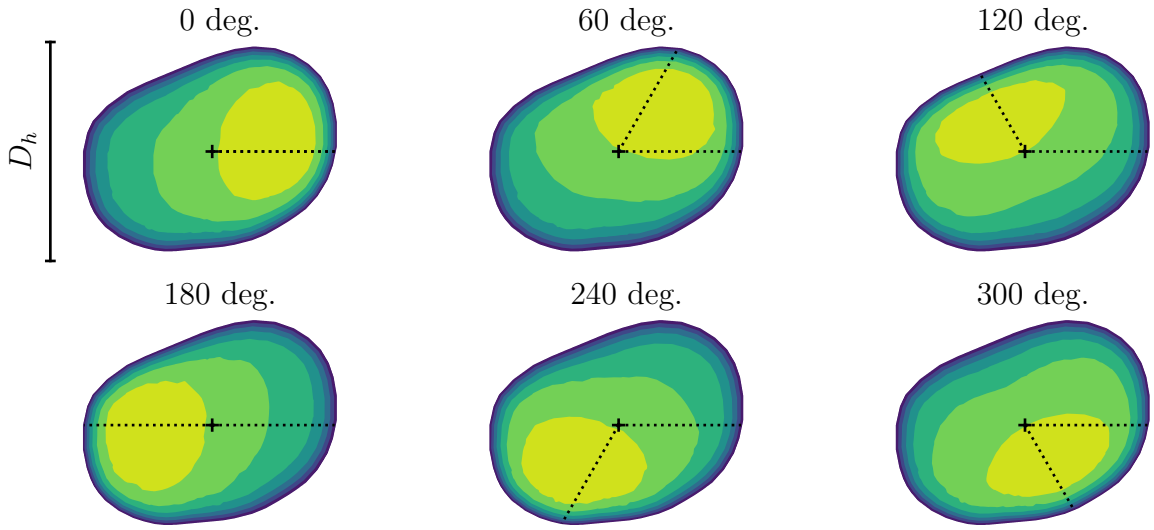

Figure B.2. Examples of Gaussian-biased inlet velocity profiles with power-law base profile ($n = 8$), with 6 variations of bias angle. Dotted lines indicating the bias angle are shown for reference.

factor R_b, angle θ_b, bias factor B, and falloff rate σ:

$$G = B \exp\left[-\frac{(x^* - x_c^*)^2 + (y^* - y_c^*)^2}{2\sigma^2}\right], \qquad x_c^* = R_b \cos(\theta_b), \qquad y_c^* = R_b \sin(\theta_b) \tag{B.3}$$

Here, a radius factor of $R_b \in [0, 1]$ moves the center of the bias region between the center and the outer edge of the boundary, the bias factor B adjusts the amount of flow biased through the Gaussian, and the falloff rate σ adjusts the size of the area through which the flow is biased. Combining the Gaussian bias with the base velocity profile of Eq. (B.1),

$$\frac{v}{v_{\text{ref}}} = (1 + G)\left[1 - \left(1 - \frac{y}{y_{\max}}\right)^n\right] \tag{B.4}$$

The reference velocity v_{ref} is determined by integrating the full profile and specifying a volumetric flow rate. By a combination of physical intuition and comparison to the results of Section 5.3, it was found that the most representative velocity profiles are specified by $B = 3$, $R_b = 0.75$, and $\sigma = 1$. Examples of the Gaussian-biased profiles remapped onto the original cross-sectional areas are shown in Figure B.2.

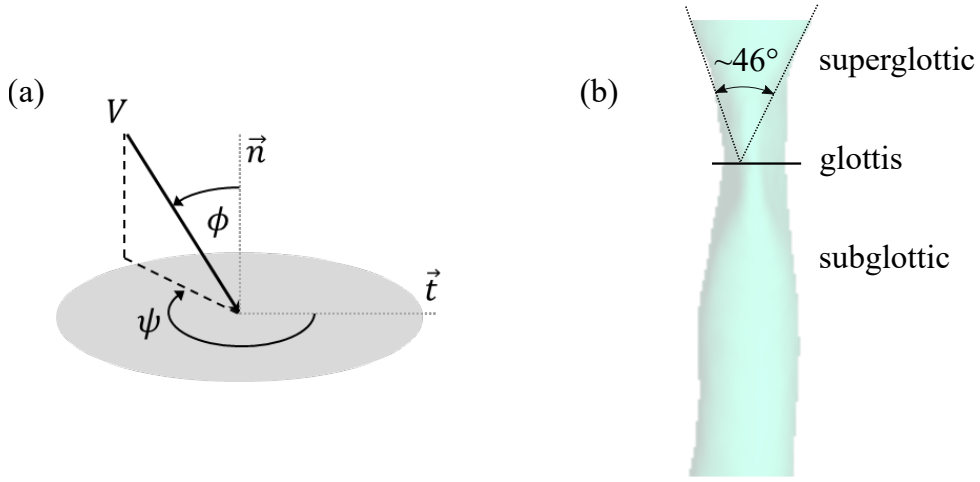

Figure B.3. (a) Illustration of inflow directivity parameters on a generic inlet boundary plane with tangent vector $\vec{t}$, normal vector $\vec{n}$, angle of incidence ϕ, and azimuthal angle ψ. (b) Maximum possible angle of incidence $2\phi \approx 46°$ measured from superglottic region of airway model.

B.2. Directivity of Inlet Flow

Since the 3D orientation of the inlet plane to the truncated model is somewhat ambiguous, it is prudent to also parameterize the direction of the inflow velocity. As shown in Figure B.3a, the velocity direction is parameterized by both an angle of incidence ϕ and azimuthal angle ψ, relative to the normal vector $\vec{n}$ and tangent vector $\vec{t}$ of the inlet boundary. While the azimuthal angle ψ may vary from 0° to 360°, the angle of incidence ϕ has well-defined geometric limits. The flow is restricted to enter from within the upstream volume; thus, its limits may be measured from the geometry, as shown in Figure B.3b. From this measurement, it is estimated that the angle of incidence may be no larger than $\phi \approx 23°$.

B.3. Numerical Simulations

For each flow rate, four variations of inlet flow bias and four variations of inlet flow directivity were used. The inlet flow directions used were as follows: 1 normal to the inlet boundary and 3 at 20° angle of incidence, with azimuthal angles evenly-spaced around 360°. The flow bias variations were as follows: 1 non-biased (with the base power-law profile) and 3 Gaussian biases evenly spaced about 360° about the inlet boundary. These

Table B.1. Summary of simulation parameters for parametric sensitivity study.

Parameter	Variants	Description
3D Model	17	One baseline, 16 stenosis variations (see Figure 5.6)
Reynolds number, $\mathrm{Re_D}$	5	Approximately 500, 1000, 1500, 2000, and 2500
Inlet Turb. Intensity	1	Determined from $\mathrm{Re_D}$ by Eq. (5.9)
Inlet Eddy Visc. Ratio	1	Determined from $\mathrm{Re_D}$ by Eq. (5.10)
Inlet Flow Direction	4	1 normal to inlet, 3 at 20° incidence (see Section B.2)
Inlet Flow Bias	4	1 non-biased, 3 biased (see Section B.1)
Total	1360	

simulation parameters are collected in Table B.1. Altogether, 1360 simulations were carried out on truncated domains. Note that many of variations represent many combinations of the "worst-case" scenario. It is therefore not expected that the results should provide a Gaussian distribution, but rather an upper bound for the uncertainty of the flow quantities. Firstly, the minimum pressure coefficient and maximum skin friction coefficient are shown in Figure B.4 with error bars indicating a 95% confidence interval (i.e. removing 5% of outlying data). Note that this result is nearly identical to the results of Figure 5.13, albeit with larger error bars. It should be noted that the relative spread of minimum pressure coefficient decreases with higher area reduction ς. This is because the higher area reductions tend to "homogenize" the flow and reduce the influence of upstream perturbations. As such, the largest uncertainties exist in the lowest area reduction ς, where the inflow perturbations largely affect the results. This trend is perhaps better examined in the loss coefficient K and the corresponding relative flow rate Φ, as shown in Figure B.5. Here, the results K are most affected by the perturbations of inflow condition at low area reductions ς. The relative flow rate Φ sees large uncertainties at low area reductions, as $0.85 < \Phi < 1.17$ for the normal case; but, much smaller uncertainties are seen at high area reductions, as $0.26 < \Phi < 0.34$ for $\varsigma = 0.90$.

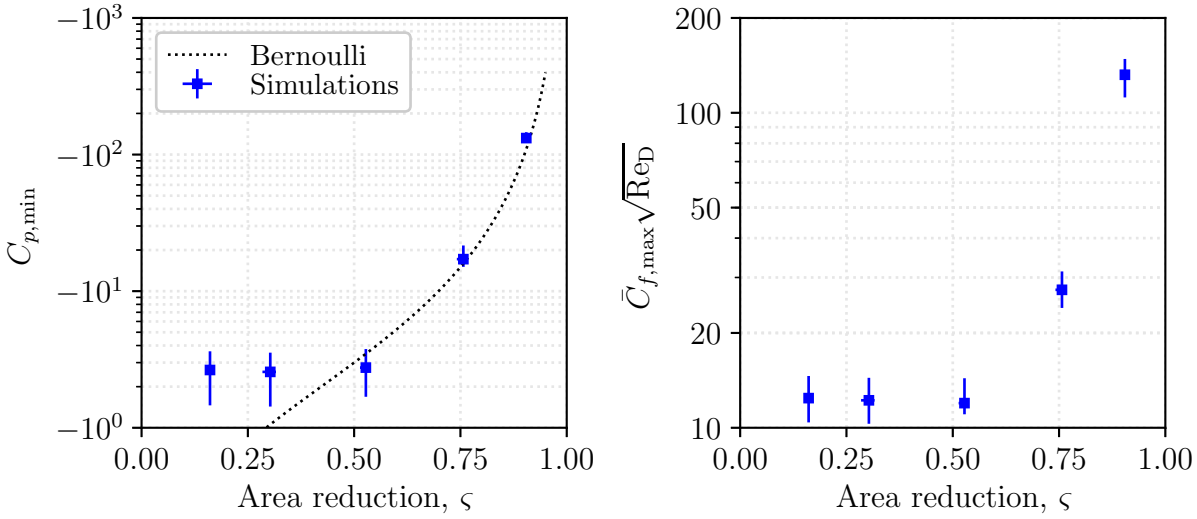

Figure B.4. Minimum pressure coefficient $\bar{C}_{p,\min}$ and maximum skin friction coefficient $\bar{C}_{f,\max}$ for all simulations versus area reduction ς, with all variations of inflow condition. A 95% confidence interval is indicated with error bars.

B.4. Discussion

The parametric sensitivity of the results of truncated domain simulations to these variations will guide simulations in future studies and provide an starting point for evaluating the uncertainties of the results. From these simulations, it is concluded that the qualitative trends are not affected by these uncertainties. Since the variations explored in these simulations represent the extreme cases of flow bias and inflow directivity, they should not be assumed to be representative of normal ranges for a given patient, but rather as lower and upper bounds. These uncertainties may be better understood and validated through experimental studies. In particular, a probability distribution for each parameter of the inflow boundary condition may be estimated experimentally through the use of a flexible airway model which can be manipulated to represent different postures, and measuring the velocity profiles with particle-image velocimetry (PIV). Once a probability distribution is acquired for each parameter, a Monte-Carlo method may be used in simulations to generate a realistic probability distribution for the aerodynamic indicators, which may be validated with the results of the very same experiments.

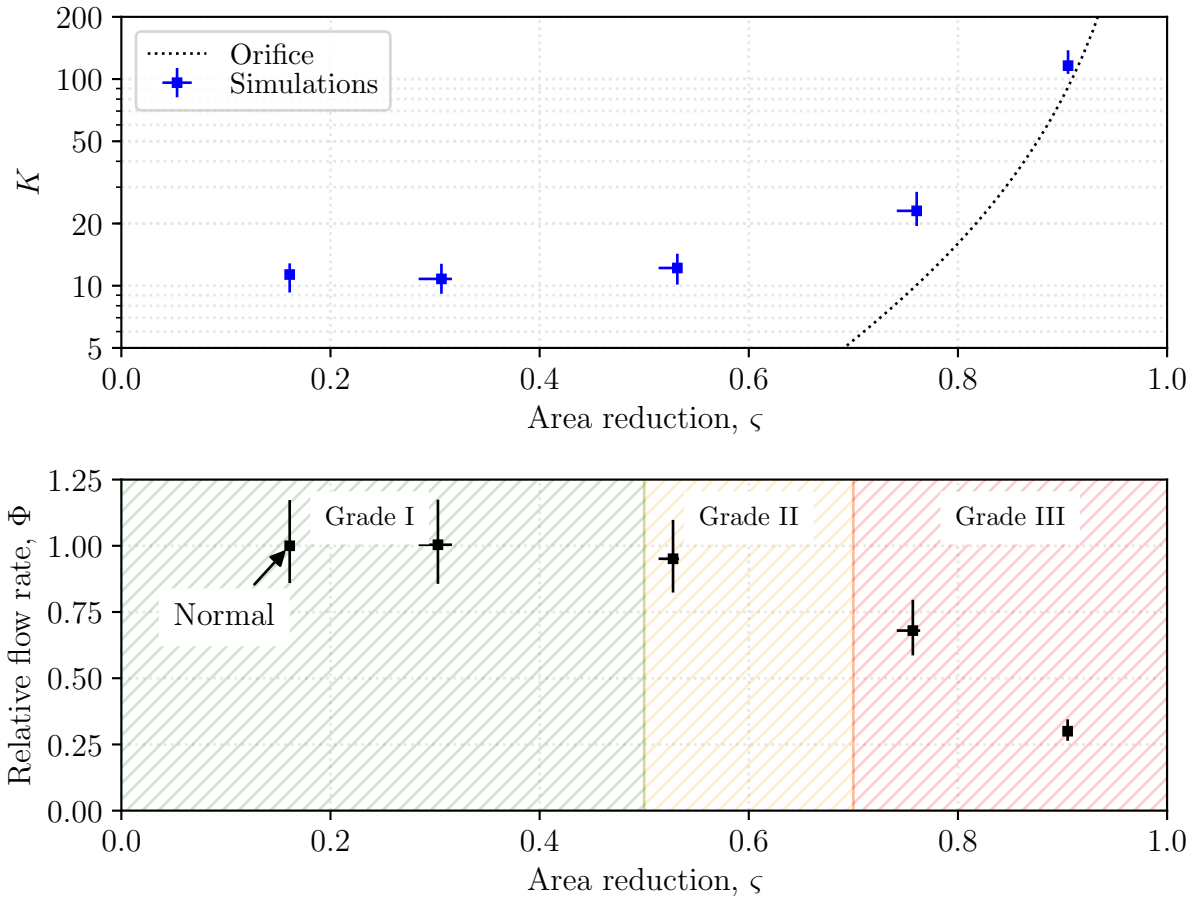

Figure B.5. Loss coefficient K and relative flow rate Φ as a function of area reduction ς, with all variations of inflow condition. A 95% confidence interval is indicated with error bars. Myer-Cotton Grades I-III are indicated as three regions of area reduction.

Vita

Joseph Poynot is a native of New Orleans, Louisiana. After graduating from Jesuit High School of New Orleans in 2009, he enrolled in Louisiana State University in Baton Rouge, where he earned a Bachelor of Science degree in Mechanical Engineering in 2013 with a minor in Mathematics. Upon graduation, he began working as a Design Engineer at International Mezzo Technologies in Baton Rouge, where he designed novel heat exchangers and heat transfer systems for motorsport, aerospace, and defense applications. It was in this position where he developed an interest and proficiency in computational mechanics and modeling. In January 2017, he returned to Louisiana State University to pursue a Master of Science degree in Mechanical Engineering. He plans to pursue an engineering research and development career in industry upon completion of his degree.